Charge Sensing and Spin Dynamics in GaAs Quantum Dots

A thesis presented
by

Alexander Comstock Johnson

to
The Department of Physics
in partial fulfillment of the requirements
for the degree of
Doctor of Philosophy
in the subject of

Physics

Harvard University
Cambridge, Massachusetts

September 2005

Thesis Advisor: Author:

Charles M. Marcus Alex C. Johnson

Charge Sensing and Spin Dynamics in GaAs Quantum Dots

Abstract

This thesis describes a series of experiments which explore and the technique of charge sensing in GaAs/AlGaAs quantum dot devices, then use charge sensing as a tool to investigate spin and charge dynamics. The first experiment generates Fano resonances and shows that charge sensing modifies the resonances in nontrivial ways. Charge sensing is also responsible on its own for features similar to Fano resonances. A phenomenological model is proposed and is is good quantitative agreement with the measured lineshapes.

The remaining experiments use sensing to measure charge in a double quantum dot. Equilibrium measurements (no source-drain bias or voltage pulses) are presented, which allow sensitive determination of interdot tunnel coupling and electron temperature. Adding a source-drain bias dramatically illuminates the spin properties of few-electron double dots via the phenomenon of singlet-triplet spin blockade, visible in both transport and sensing measurements.

By adding gate-voltage pulses to these systems, we can measure energy spectra and dynamics in isolated or nearly-isolated double dots. In the isolated case we demonstrate excited state spectroscopy and single-shot charge position measurements. In few-electron double dots we present spin relaxation and dephasing measurements showing that the effective magnetic field from hyperfine interaction with the host Ga and As nuclei causes random spin precession on a timescale of ∼10 ns (measured both by direct time-domain measurements and by a linewidth in field), and that this is the only significant source of spin dephasing up to ∼1 ms.

Contents

List of Figures

Acknowledgements

Experimental physics is an inherently collaborative effort on just about all levels, all the way from talks with experts from around the world, where one parenthetical remark can spark a new line of experiments, to times when I might have forgotten to eat or sleep without a little help from my friends. There are far too many people who contributed to my Ph.D. for me to have any hope of thanking them all, but here we go.

My first thanks go to Charlie, without whose wealth of experience, unending stream of ideas, and remarkable intuition, none of this would have been possible. I am particularly grateful to Charlie for his sincere passion for the truth and his devotion to doing things right, in lab, in publications, and in the world beyond physics.

The other grad students in the group are the ones who make the day-to-day experience what it is. My time here began with many late nights with Ron, Josh, and Andrew, and eventful days with Sara, Jeff, Dominik, and Heather. Despite the failing experiment, Josh teaching me and Ron to run a fridge was a great introduction to low-T physics. Ron was always happy to talk about physics, especially when he had a paper to write, and Josh was always happy to plan the next experiment (or hike, bike ride, or ski trip). With Andrew around there was never a dull moment, and always a new game to play (crossword, foam-based, or otherwise). Sara's no-nonsense attitude injected a healthy dose of realism and perspective into Marcus lab life, and the lab has never really recovered from the departure of its social coordinator. Heather taught us all what a lab notebook could look like, and Dominik showed that if you take twelve papers worth of data at once you'll have more time for parties and dancing. Jeff, besides brightening the lab with his incredible creativity (and his award-winning plants), could make a photo album of everything that happened during my tenure in lab, which he is the only one to share in its entirety. Jeff's easy-going but organized manner meant that when he was around you knew everything would work out, because there was always a backup plan.

The next year Leo and Mike joined the lab, increasing the lab's diversity of expertise (Leo the electronics and RF jock, and Mike the nanotube jock) and personalities (Leo the crazy latin drummer turned marathon runner and Mike the metro DJ politics junkie). I owe many thanks to deli meat for resuscitating me after brutal penny wars with Mike. Working with Jason over the last year and a half has been a real pleasure. His manner of powering through any problem is inspiring, be it in fabrication, measurement, or an effeminate piece of hardware. I'd also like to thank Jake and Lily, who managed to straddle the worlds of theory and experiment admirably, Edward who is just as quick a learner in lab as on the slopes, and Yiming who almost seemed cheerful about taking the evaporator job from me. I could go on, thanking all of the other students, postdocs, visitors, and the excellent staff at Harvard (the group would grind to a halt without the able help of James I, II, and III, Tomas and Matt, Jim MacArthur, Louis and his machinists, Ralph and Joan, and many others) but I have the feeling this acknowledgements section would never end.

So finally I'd like to thank Stela for bringing more joy than she knows to my life, and my parents for making this all possible, encouraging and supporting me without fail through more than twenty years of formal education.

Chapter 1

Introduction

The theory of quantum mechanics is one of the great success stories of 20th century science, and it goes hand in hand with the explosion of electronics technology. As dramatic as this technological advance has been, however, so far most electronic devices have been engineered semiclassically: quantum mechanics tells us what kind of potential electrons feel in different materials but beyond that the electrons are treated as classical particles. There is still a long way to go before the size and energy scales of individual atoms limit the miniaturization and speed of electronics.

While the electronics industry tends to take a top-down approach, starting with large, well-understood systems and watching what happens upon shrinking them, basic physics, especially theoretical physics, tends to prefer a bottom-up approach, building complex systems from their well-understood component particles. In one trivial sense the quantum mechanics of everyday particles is complete: the equations of motion for electrons and atomic nuclei interacting with each other are known, so in principle we can predict what will happen to any given collection of such particles in any given initial state. But while simulations based on the exact equations are often useful in classical physics—for designing cars and bridges, for sending rockets to other planets—the complexity of the exact equations grows so much more quickly in quantum than in classical mechanics that simplifying assumptions must be made for even a small number of particles. Grappling with this complexity is the central pursuit of condensed matter physics.

In the last several decades, thanks mainly to advances in nanoscale fabrication techniques, a new research field dubbed *mesoscopic physics* has emerged, at the boundary of these top-down and bottom-up understandings of many-particle systems. Mesoscopic (meaning medium-sized) refers to the length scale of particle confinement being smaller than its coherence length, such that the localized effects of quantum mechanics become important, but not as small as the atomic scale at which it would interact with only a few other particles.[1]

This thesis concerns electrons confined to a 2-dimensional electron gas at the boundary of two semiconductors, GaAs and $\mathrm{Al}_x\mathrm{Ga}_{1-x}\mathrm{As}$. This system has been remarkably prolific because of the ease of engineering a wide variety of quantum states. The experiments presented here are linked by a technique known as *charge sensing*, which has been known for over a decade but only in the past few years has its power and versatility become apparent. This thesis helps develop charge sensing from a technique under investigation in its own right to a robust method of measuring isolated systems, which yields otherwise inaccessible information about the energy spectra, the spin states, and the dynamics of electrons in a semiconductor lattice.

---

[1] Some definitions limit mesoscopics to systems of particles confined on scales larger than their wavelengths [1], such that they interact with many of each other. As we will see, however, interesting many-particle interaction effects are seen with even a single electron if its wavefunction is spread over many lattice sites.

1.1 Organization of this thesis

Chapters 2 and 3 review the background necessary to understand the experiments in this thesis. Chapter 2 introduces GaAs nanostructures and the techniques for creating and measuring them, and Ch. 3 discusses the main concepts involved in understanding the particular nanostructures used in the experiments to follow, namely quantum point contacts and single and double quantum dots.

Chapter 4 discusses an experiment designed to measure Fano resonances. The analysis of these data constituted a watershed moment in my thinking about quantum dot measurements; though other members of the group were already working on charge sensing, the Fano resonance experiment showed the ubiquity and strength of charge sensing, to the extent that while Fano resonance could be found in certain small portions of parameter space, charge sensing was, to our dismay at the time, reliably found everywhere. Connect that reliability with the other advantages we were beginning to realize charge sensing possessed, and sensing became the new tool of choice. Chapter 5 describes the use of charge sensing in a double quantum dot to determine not just the presence but the positions of electrons. This allowed us to study isolated double quantum dot devices, which never exchange charge with any reservoirs but merely shuttle electrons from one side to the other. Chapter 6 describes pulsed-gate measurements of such an isolated device, yielding the excited state spectrum and allowing a single-shot measurement of charge location.

Next we move to a smaller double dot design, which can be tuned to zero, one, or two electrons in either dot with arbitrary interdot and dot-lead tunnel couplings. In this few-electron regime, orbital energy level separations become very large while the available spin states become simple and well-understood. Chapter 7 describes DC transport and charge sensing measurements of this device in both the one-electron and two electron cases. A strong bias asymmetry is observed in the two-electron case, which fits neatly into a model in which the ground state for two electrons in one dot is a spin singlet whereas two separated electrons may take either a singlet or a triplet spin state. This effect, known as singlet-triplet spin blockade, formed the basis of our subsequent pulsed-gate measurements investigating two-electron spin dynamics in real time. Chapter 8 describes our first successful pulsed-gate scheme in this device. In this scheme, a separated two-electron state is prepared with a uniform mixture of spin states, then tilted so that the ground state has both electrons in the same dot. As this experiment was performed with weak interdot tunneling, it tells us about the long-time behavior of spins in this system, and the magnetic field dependence of the results pointed to hyperfine interaction with nuclei as the main source of spin evolution. Chapter 9 describes the second successful pulsed-gate scheme, in which a separated singlet state is prepared by splitting the overlapping singlet, then after some time we attempt to push the electrons back into the same dot. The time dependence of these results give us the first direct measure of the inhomogeneous spin dephasing time T_2^* in a single-electron quantum dot, while the magnetic field dependence provides insight into the energy levels of this system with unprecedented precision.

The appendices provide some experimental and theoretical details which I hope will be useful to others in the field. Appendix A provides more detailed theory of quasistatic nuclear fields, backing up Ch. 8, much of which is relevant also to Ch. 9. Appendix B describes some of the circuitry and wiring I built for use inside and outside the cryostat, and Ap. C describes our cold finger design. Appendix D describes some Igor programs I developed for data acquisition and management. Finally, Ap. E has some miscellaneous techniques for measuring devices efficiently.

Chapter 2

GaAs nanostructures

Quantum state engineering involves the creation of well-defined potential profiles on the scale of the partcles' wavelengths. The known ways of doing this are myriad. Photons and atoms can interact in free space [2, 3] or solid state [4, 5] cavities. Electrons (or composite particles such as excitons or cooper pairs) can be bound to nanostructured materials such as carbon nanotubes [6, 7], semiconductor nanowires [8], metal grains [9, 10], self-assembled quantum dots [11, 12], or lithographically patterned superconductors [13, 14] or semiconductors.

Of all these techniques, perhaps none has shown the versatility and tunability of the lithographically patterned GaAs/AlGaAs semiconductor heterostructure. Two-dimensional systems can be made with unrivaled homogeneity and arbitrary density [15, 16, 17]. From this starting point, one-dimensional [18, 19, 20, 21] and fully quantized zero-dimensional systems [22, 23, 24, 25] can be made in almost any imaginable combination, and the individual elements of the Hamiltonian—energy levels, tunnel couplings, interference phases, and more—can be tuned by external parameters within a single device. This chapter describes some of the techniques for creating and

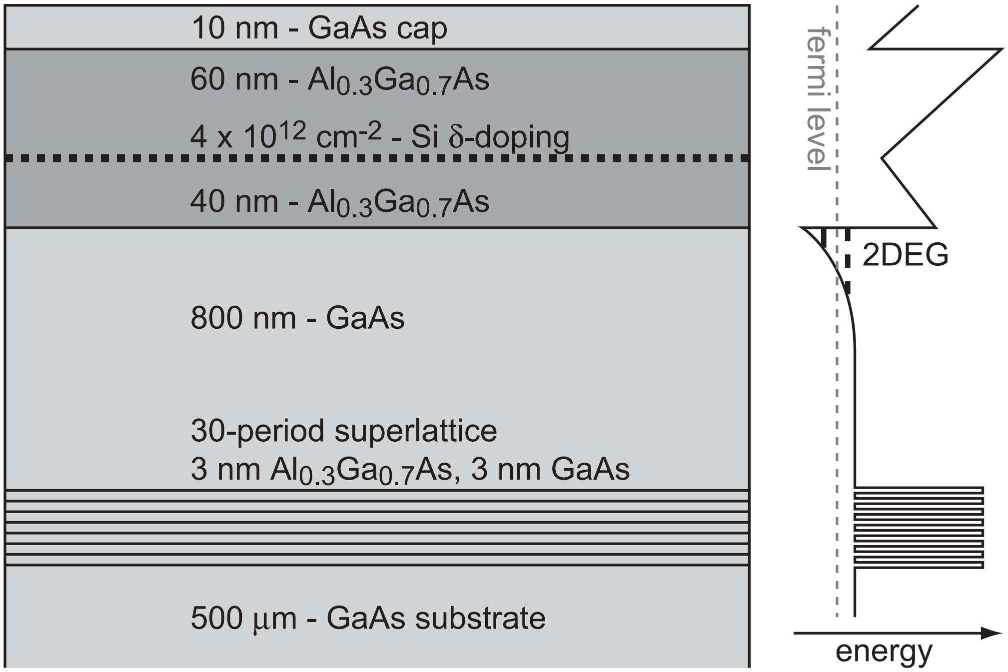

Figure 2.1: Wafer structure of a 2DEG. At right the energy of the conduction band edge is shown schematically vs. depth. A trianglular potential well is formed at the buried GaAs/AlGaAs interface with one subband (thick solid line) below the Fermi level. Other subbands (thick dashed line) are inaccessible. The specific parameters shown here describe the nominally identical wafers 010219B and 031104B, grown by Micah Hanson at UCSB, which were used to make all of the devices used in the experiments in this thesis.

measuring this endless variety of devices.

2.1 GaAs/AlGaAs heterostructures

The first step in creating a GaAs nanostructure is to make a two-dimensional electron gas (2DEG) [26] at the interface between GaAs and $\mathrm{Al}_x\mathrm{Ga}_{1-x}\mathrm{As}$ (typically $x \sim 0.3$) as shown in Fig. 2.1. Positively charged donors (usually group IV silicon atoms substituting for group III gallium or aluminum) are placed tens of nanometers away from the interface in the AlGaAs region. Because AlGaAs has a larger band gap than GaAs, the global potential minimum is not at the donors but at the interface with the GaAs. This separation of dopants and charge carriers is called *modulation doping*, and is responsible for the extraordinarily smooth potential in the 2DEG plane in two ways. First, because GaAs and AlGaAs have nearly identical lattice constants and can be grown with atomic precision using molecular beam epitaxy (MBE), there are few defects at the interface. Second, potential fluctuations due to the random locations of the donors are smoothed by their distance from the interface (40 nm for these wafers), which is larger than the average distance between donors (5 nm). Modulation-doped heterostructures can achieve mean free paths as high as 100 μm even for densities as low as one electron per (100 nm)^2. The other layers in a heterostructure wafer play subtler roles in maintaining 2DEG quality: far below the 2DEG there is a GaAs/AlGaAs superlattice which smoothes any impurity potential in the underlying bulk GaAs wafer, and above the AlGaAs layer is a thin cap of GaAs, to prevent oxidation of the surface, which could also occur randomly and affect the potential at the 2DEG.

2.2 Contacting the 2DEG

All of the measurement techniques I will describe involve measuring the current/voltage characteristics of various regions of 2DEG, and to do this we need to make electrical contact between the 2DEG and a metal, that we can attach a wire to. These are referred to as *ohmic contacts* because good ones behave just like small resistors. Two barriers must be overcome to make contact to a 2DEG: the structural barrier (the 100 nm insulating AlGaAs layer above the 2DEG) and the Schottky barrier inherent in a metal-semiconductor interface. The most common contact method, and the only one used in the devices in this thesis, is to deposit gold-germanium on the surface and anneal it into the wafer. The standard picture invoked to describe the annealing process is that spikes of gold extend through the AlGaAs to penetrate the physical barrier, bringing germanium to diffuse into the GaAs, where it is an n-type dopant and thus lowers the Schottky barrier. Within this model it is easy to explain the need to precisely tune the annealing time and temperature: too little annealing and there will be too few metal spikes reaching the 2DEG layer; too much annealing and the spikes will all merge, such that electrons may only enter the 2DEG at the very edge of the contact. For this reason, every time a new wafer is used, a new annealing recipe must be determined by trial and error for best contact.

The following is a typical ohmic contact recipe: Deposit 5 nm Pt, 100 nm AuGe, 25 nm Pt, and 100 nm Au on the clean surface of the wafer, then heat to 480 °C for 60 seconds. The first platinum layer is very thin, and is present solely to help the gold-germanium stick to the surface. In the past the group has used nickel for this purpose, but we have avoided this more recently because nickel is ferromagnetic and causes heating when the magnetic field is swept through zero.[1] The gold-germanium layer that follows is intended to be a eutectic (lowest melting point) mixture of 88% gold, 12% germanium. The eutectic temperature is 356 °C (compared with $\sim$1000 °C for either pure gold or pure germanium). This is well below the annealing temperature, so this layer liquefies during the anneal, which presumably greatly enhances its diffusion into the wafer. Above the AuGe is a platinum barrier layer and then a layer of pure gold to aid wirebonding. In practice, however, another layer of gold is often deposited

---

[1] It isn't clear which bit of nickel was responsible for this heating. We eliminated nickel here and in the sticking layer for gold-plated connectors in several locations near the device, and this field-sweep heating has disappeared.

after annealing because this first bonding layer can harden during the anneal.

A good contact has two closely related properties: it follows Ohm's law $V = IR$ over the useful current range $|I| < 100\text{nA}$,[2] and the resistance R of the contact is small compared to the device to be measured. For most measurements of GaAs nanostructures, $R < 1\text{k}\Omega$ is considered good, although we have on occasion seen contact resistances of 50 Ω or less for normal $\sim$ 100-150 μm square pads. Contacts with resistance $R > 10\text{k}\Omega$ can still be used if necessary, but they are likely to show pronounced non-Ohmic and frequency-dependent response, which complicates the interpretation of data, even if used in a four-wire configuration which normally removes the contact resistance from the measurement.

2.3 Depletion gates

Nanostructures can be created in an existing 2DEG by a variety of methods, including etching [27], local oxidation [28, 29], local charging [30], and electrostatic gating [18, 31, 22, 23]. The common feature of all of these approaches is that they raise the Fermi level in a particular region of 2DEG above the first z-subband minimum, excluding all electrons from that region. The most versatile approach is electrostatic gating, where electron beam lithography is used to define metal gates with feature sizes of 100 nm or less.[3] An arbitrary negative voltage can be applied to each gate,

---

[2] 100 nA is the current generated by 1 mV across an open single-mode quantum channel, $R = h/2e^2$, as described in Sec. 3.1.

[3] An argument could be made that local charging by a scanned probe is more versatile, because after cooling you can draw any arbitrarily complex device without extra gates, however the hysteretic nature of such charging and the inability to change more than one parameter without moving the probe limit the use of this technique in practice.

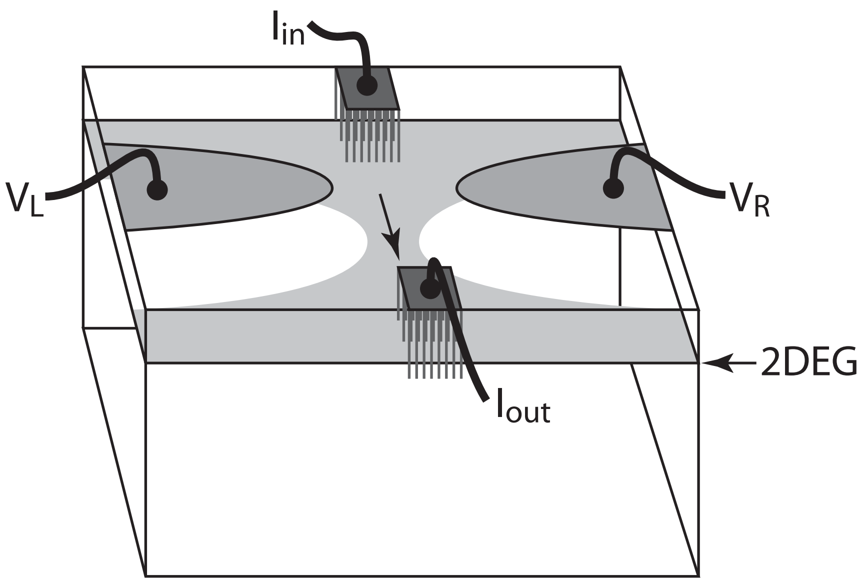

Figure 2.2: Metal gates are deposited on the surface of the wafer, defined by electron beam lithography. Wires are bonded to these gates and attached to external negative voltages, labeled V_L and V_R on this simple drawing. Regions where electrons remain in the underlying 2DEG are shown in light grey. Ohmic contact is made to the 2DEG regions on either side of the device to allow current to flow in and out of the 2DEG through the device.

raising the potential and removing the electrons from a variably sized region under and around the gates, as illustrated in Fig. 2.2. Determining exactly what potential is created in the 2DEG for a specific configuration of gates and gate voltages can be extremely difficult for a number of reasons.[4] Fortunately the exact details of the potential are seldom important, and most systems can be expressed by effective Hamiltonians in which the important parameters can be measured experimentally and tuned by the gate voltages.

---

[4] For example, the electrons in the 2DEG screen the gate potential to some degree, but due to their long wavelengths such screening is imperfect, and stops altogether where the 2DEG is depleted. Other factors complicating this analysis include the "impurity" potential due to the random locations of ionized donors or crystal impurities, and selective ionization of donors due to our trick of cooling with a positive gate bias. Among others, Mike Stopa [32, 33, 34] has made a career of calculating 2DEG potentials, and the Heller and Westervelt groups [35, 36] have extensively studied transport through impurity potentials.

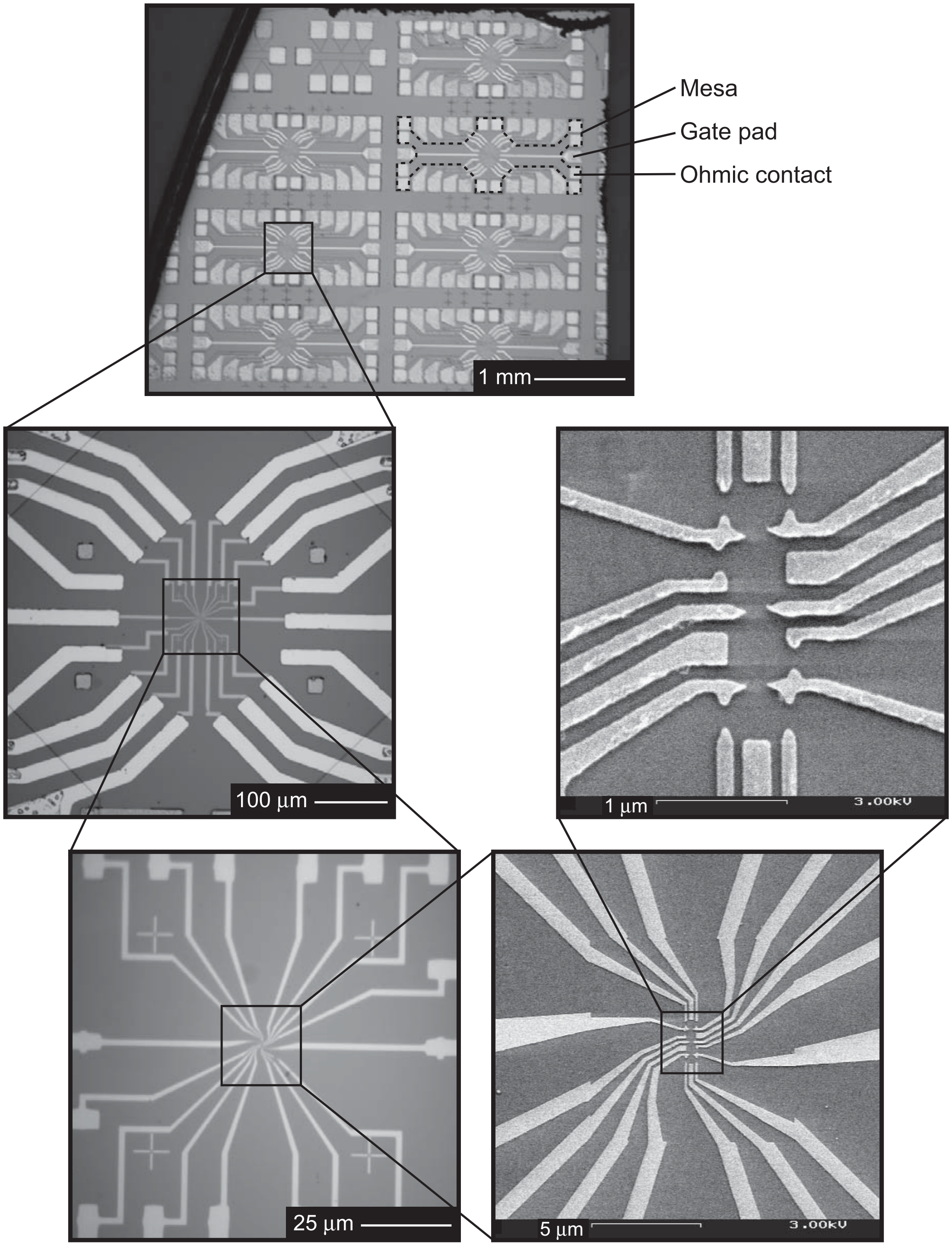

Figure 2.3: Multi-scale view of *Gorgonzola* (aka HJL18), the chip used in Chs. 5 and 6. The upper image shows the entire chip. Dashed line highlights the outline of one mesa. Bond pads on the mesa are ohmic contacts, bond pads off mesa are gates. Continuing counter-clockwise, we zoom in on the center of one device by about a factor of 5 each time. The three largest-scale images are from an optical microscope, the two smallest from a scanning electron microscope.

The upper image of Fig. 2.3 shows a complete chip. Because a lot of work goes into making a good 2DEG wafer and learning how to make good ohmic contacts and gates on it, and because there can be a significant failure rate for devices due to fabrication errors or for unknown reasons, it is advantageous to maximize the number of devices made out of one wafer. For this reason, we pack many devices onto a single chip. Putting multiple devices on one chip requires an additional fabrication step to electrically isolate the devices from each other. We do this by etching away the 2DEG between the devices, leaving behind a "mesa" of 2DEG for each device, one of which is outlined on the upper image of Fig. 2.3. Surrounding each device is a set of metal pads (100–150 μm squares) for wire bonding. The pads on-mesa are ohmic contacts, and the pads off-mesa are gates. The remaining images in Fig. 2.3 magnify the center of the device, following the gates and 2DEG reservoirs from their macroscopic bond pads down to their fine tips defining the submicron-scale device. In the most zoomed-in image (center right), imagining a depletion halo around each gate shows where four confined regions of electrons (quantum dots) will be located, connected to each other by three tunnel barriers and connected to 2DEG reservoirs by another six barriers.

Chapter 3

Quantum transport

This chapter lays the theoretical groundwork for the experiments described later on. I have not tried to give an exhaustive treatment of quantum transport, rather to introduce the physics of key device elements and give references to neighboring applications in the literature. Most of the concepts in this chapter can also be found in review articles or books, my favorites being Datta [37] and Imry [38] for 2D and 1D systems and scattering and the Kouwenhoven review [39] for dots in the Coulomb blockade. Van der Wiel's review [40] is an excellent detailed reference on Coulomb-blockaded double dots.

3.1 Quantum point contacts

The simplest nanostructure to make in a 2DEG is a constriction, such as is shown in Fig. 2.2, by depleting two gates with a gap between them. A short constriction is known as a quantum point contact (QPC). A remarkable property of a QPC, and one that was by no means obvious before it was observed, is that even if there are only a few electron wavelengths from the entrance to the exit of the constriction it behaves almost identically to the theory for an infinitely long clean wire of uniform width.[1] Analyzing the infinite wire is straightforward: regardless of the shape of the transverse potential, motion in this direction can be quantized into discrete transverse subbands, just as was already done in the z direction due to the heterostructure. Electrons then propagate freely along the wire with a dispersion relation $E = \hbar^2 k^2/2m^*$ determined solely by the effective mass m^*, which in GaAs is $0.067m_e$, where m_e is the electron mass, 9.11×10^{-31}kg. As it turns out, however, we don't even need to know the dispersion relation to determine the conductance of this system.

Consider for simplicity the case of zero temperature and one transverse subband occupied at the Fermi energy at each end of the wire, but with higher Fermi energy on one side (the source) than on the other side (the drain). At any energy where states on both sides are occupied, the current passing one way through the constriction must exactly cancel the current passing the opposite direction in order to satisfy detailed balance. The net current is therefore given by the rate of electrons passing through the constriction above the drain Fermi level but below the source, $I = e \int_{E_d}^{E_s} dE \frac{\partial^2 N}{\partial E \partial t}$. Taking the derivative with respect to voltage by using $E = eV$, the differential conductance is

$$G = \frac{dI}{dV} = e^2 \frac{\partial^2 N}{\partial E \partial x} \frac{\partial x}{\partial t}. \tag{3.1}$$

We can evaluate the first term (the linear density of states) by applying infinite boundary conditions to our wire and counting nodes, which gives $\frac{\partial N}{\partial x} = \lim_{x \to \infty} \frac{N}{x} = g_s \frac{x/(\lambda/2)}{x} = 4\pi g_s k$ where the spin degeneracy $g_s = 2$ for our spin-1/2 electrons at low magnetic field. For the purposes of calculating current we consider only half of these

---

[1] Note that because the 2DEG depth ($\sim$ 100nm) is typically several wavelengths ($\sim$ 50nm), nearly every constriction meets this requirement, since the potential from surface gates is softened on roughly the scale of the depth.

states (those moving from source to drain), so $\frac{\partial^2 N}{\partial E \partial x} = 2\pi g_s \frac{\partial k}{\partial E}$. The second term in Eq. 3.1, $\frac{\partial x}{\partial t}$, is the group velocity, also written as $\frac{\partial \omega}{\partial k} = \frac{1}{\hbar}\frac{\partial E}{\partial k}$. Putting these together, the two derivatives exactly cancel, leaving

$$G = g_s \frac{e^2}{h}. \tag{3.2}$$

Because of the remarkable simplicity of this equation and the fact that so few assumptions went into it, e^2/h is known as the *universal quantum of conductance.* Temperature and higher subbands can easily be added to this picture. Each time a new subband edge crosses the Fermi level the conductance increases by $g_s e^2/h$, resulting in a series of conductance steps as a function of gate voltage. Temperature has the effect of averaging over a distribution of energies, and as such it has no effect on the levels of the conductance plateaus. The primary effect of temperature is to broaden the transitions from sharp jumps as each subband minimum changes from empty to filled, to smooth increases as the probability of occupying the bottom of a new subband gradually increases from 0 to 1. In high-quality QPCs this broadening can be used to measure electron temperature.

QPCs vary greatly in the degree to which they match this model. There is, of course, the "0.7 structure," studied extensively by the Marcus group and others [41, 27, 20, 42], which affects details of the transition from zero to one mode. Here we are concerned with more drastic effects which introduce backscattering, where electrons which would otherwise have passed through the constriction are scattered back to the source reservoir, altering the basic picture of smooth transitions between conductance plateaus. This can be caused by impurities in or near the channel, by too-sharp edges of the QPCs making the transition from 2D reservoirs to the 1D channel non-adiabatic,[2] by other depletion gates if the QPC is part of a more complex device, or by a combination of small-angle impurity scattering and scattering off other depletion gates. For this reason, a more complete description including a finite, energy-dependent transmission coefficient $T_n(E)$ for each mode n is often useful. We can then write the conductance as

$$G = \frac{e^2}{h} \sum_n T_n(E_f) \tag{3.3}$$

or, at finite temperature,

$$G = \frac{e^2}{h} \int dE \, \frac{\partial f(E - E_f, T)}{\partial E} \sum_n T_n(E), \tag{3.4}$$

where $f(\epsilon, T)$ is the Fermi distribution for temperature T. This is known as the two-terminal Landauer formula. Each transmission coefficient may have complicated non-monotonic behavior as a function of energy, although in general they all tend from zero at low energy to unity (full transmission) at high energy.

Another way to interpret a transmission coefficient less than 1 is as the onset of tunneling. The term tunneling is usually reserved for a process which is classically disallowed, meaning that the potential profile rises above the total energy of the particle at some point in the barrier. A particle has negative kinetic energy while tunneling, whereas scattering can occur even due to a drop in potential and an increase in kinetic energy. Truly infinite 1D channels would not allow tunneling, because a barrier of any height has zero transmission at infinite length. But real QPCs, with lengths of only a few electron wavelengths, make very good tunnel barriers. In the end, there's no difference between low transmission caused by tunneling, by scattering, or even by interference [43].

---

[2] This effect is analogous to the well-known effect from introductory quantum mechanics, in which a particle moving in 1D can be backscattered by a sharp drop in potential, which does not occur in classical mechanics.

Figure 3.1 shows some of the behaviors possible in a QPC. The QPCs in (a)–(c) were made as independent devices, with no other nearby gates and with shapes optimized for clean transmission. All of these devices show multiple clear plateaus at the expected conductance values (note that the vertical scale in (a)–(c) is in units of $2e^2/h$), although in some cases there are bumps or dips in the plateaus. Contrast this with QPCs integrated into more complex devices, with constrained geometries. Conductance traces for four such QPCs are shown in Fig. 3.1 (d)–(g). In these QPCs, instead of a smooth rise to a plateau at $2e^2/h$, we see gradual bumpy increases, often with sharp peaks indicative of resonance, sometimes with what looks like a plateau but at an arbitrary conductance. Behavior of these QPCs at and above $2e^2/h$ is not shown, but they only sometimes have a plateau at all, and generally the conductance just continues its bumpy rise higher and higher. All of these effects indicate complex behavior of the transmission coefficients, rather than a simple turn-on as the subband minimum crosses the Fermi energy.

3.2 Quantum dots

Whereas a quantum point contact is the restriction of a 2D electron gas in one more dimension, forming a 1D channel, a quantum dot is the restriction of electrons in all three dimensions, and as such is sometimes referred to as a zero-dimensional (0D) system. Typically, in order to study quantum dots, two QPCs are incorporated into the perimeter of the dot, and properties of the dot are inferred from the conductance of electrons going in one lead and coming out the other. Although many other geometries and measurement techniques are possible (some of which are explored in the coming

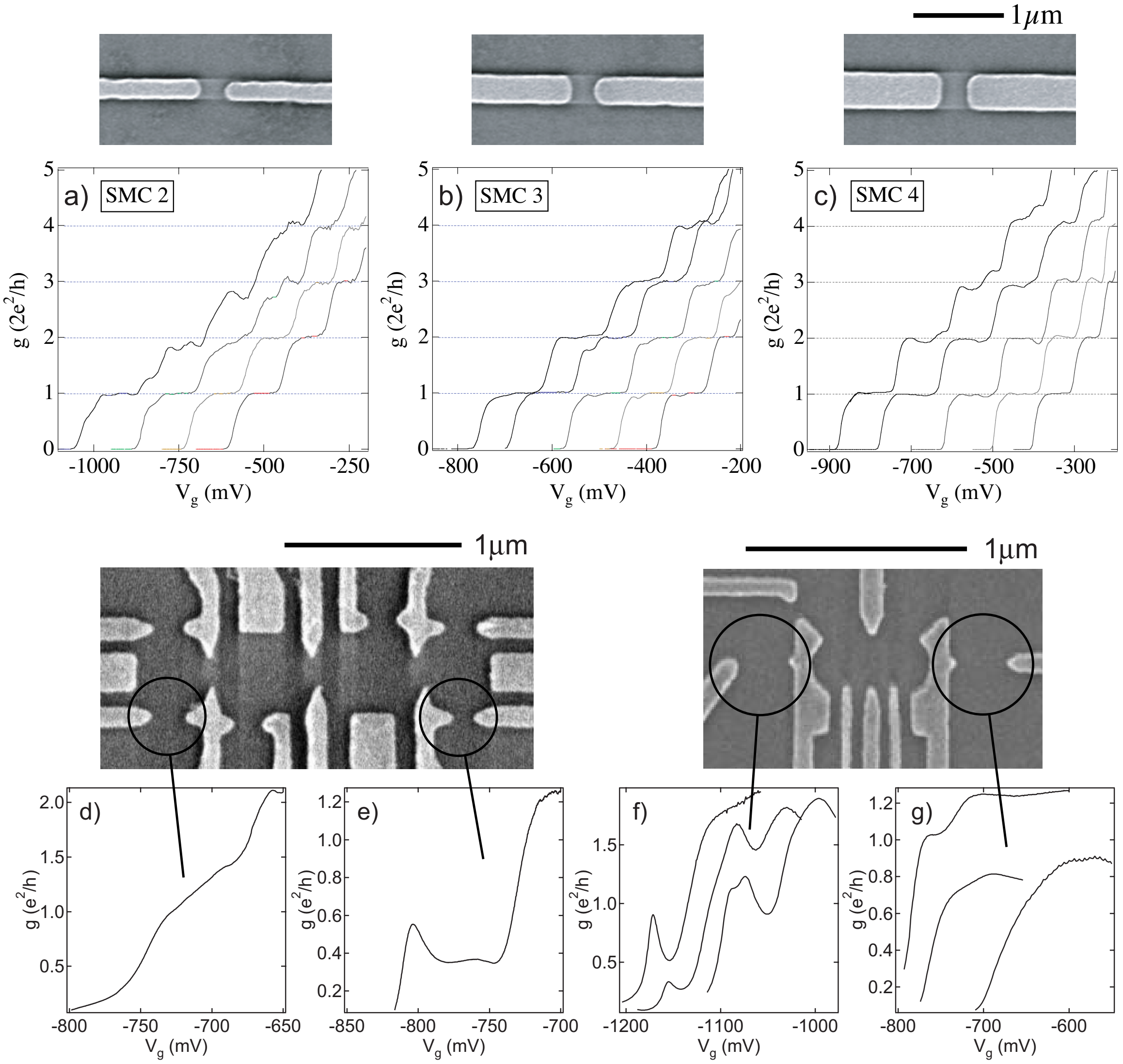

Figure 3.1: Sample QPC conductance traces. a)–c) Conductance vs. gate voltage V_g for three QPCs made for independent study (data courtesy of S. M. Cronenwett [1]). d)–g) Analogous traces (showing only the region below $2e^2/h$) for four QPCs in two devices used as charge sensors in Chs. 5 and 6 (d,e) and in Chs. 7–9 (f,g).

chapters), we begin by reviewing standard transport through a dot. Understanding the successes and limitations of transport measurements motivates the use of charge sensing for certain purposes, which I describe below in Sec. 3.4.

Quantum dots can be divided into two categories with strikingly different properties: open dots, where the QPC leads are set to fully transmit at least one mode, and closed dots, where all of the leads are set as tunnel barriers. Open dots are important laboratories for interference effects, quantum chaos, and the various statistical ensembles available due to, for example, shape distortions, magnetic fields, and spin-orbit coupling [44, 45, 46, 47, 48]. All of the experiments in this thesis concern closed quantum dots, and the remainder of this section will introduce the physics of these systems.

A closed quantum dot can be represented schematically as an island of charge connected capacitively and via tunnel barriers to conducting reservoirs, and purely capacitively to any number of gates. For simplicity here I will assume source and drain reservoirs (with capacitances C_s and C_d and voltages V_s and V_d and a single gate (C_g and V_g) as shown in Fig. 3.2(a). The Hamiltonian of the dot can then be written as

$$H_{QD} = E_c \frac{N(N-1)}{2} - \frac{Ne}{C_\Sigma}(C_g V_g + C_s V_s + C_d V_d) + \sum_{i,\sigma} N_{i\sigma}\epsilon_{i\sigma} \tag{3.5}$$

where C_Σ is the sum of all gate and lead capacitances and is related to the charging energy E_c by $E_c = e^2/C_\Sigma$. The first term is the Coulomb energy associated with putting N electrons onto the island together, making the *constant interaction* approximation that every electron feels a Coulomb repulsion energy E_c with every other electron, regardless of what quantum state either electron occupies. The second term in Eq. 3.5 is the Coulomb interaction between electrons in the dot and the other nearby conductors, where C_Σ is the sum of all the individual capacitances. Again we've assumed constant interactions with these conductors independent of the quantum state of each electron. There are several trivial corrections to the constant interaction approximation, such as a general decrease in E_c as N increases. Simple electrostatics imply that E_c should vary somewhere between inversely with area (if the dot/gate geometry looks like a parallel plate capacitor) and inversely with perimeter (if the dot is large and coplanar with the gates). Typical values of E_c in GaAs quantum dots range from several meV in few-electron dots to a few hundred μeV in large (~1000 electrons) dots. There are also deviations from the constant interaction model with more interesting effects, such as Hund's rule [49], which we will touch on in Ch. 7.

These first two terms are essentially classical, requiring only that charge be quantized. The final term in Eq. 3.5 is due to quantum confinement in the electrostatic potential of the gates. Here we make the approximation that each electron enters a single-particle energy level, where the i-th level with spin σ has energy $\epsilon_{i\sigma}$ and is occupied by $N_{i\sigma} = 0$ or 1 electrons. The many-particle state is then simply the product of the occupied single-particle states. The validity of this approximation is the subject of countless works, both theoretical and experimental, in a wide variety of quantum systems; Ref. [50] provides an introduction to this question as it concerns 2DEGs, and shows that the single-particle picture is remarkably successful in dots containing several hundred electrons. More recent studies of few-electron quantum dots have shown the single-particle picture to work well enough that a shell structure similar to atomic energy levels can be observed [25], leading these systems to be called "artificial atoms." Later chapters will have more to say about the spectra of energy levels $\epsilon_{i\sigma}$ in a quantum dot, but for now it is only important that they are arrayed with some mean energy spacing Δ between successive levels of the same spin.[3] Since the density of states in 2D is a constant, in large dots where the effect of the gates on the potential is screened except near the perimeter, Δ goes as inverse dot area, or simply $\Delta = g_s E_f / N$ where E_f is the Fermi energy measured relative to the band minimum.

---

[3] For the most part this is the relevant spacing, because even when spin degeneracy is broken, states of opposite spin will hybridize with each other only very weakly.

E_f is around 7 meV in the 2DEGs used here, so a 0.5 μm^2, 1000-electron dot would have $\Delta \approx 14\mu$eV. The gate potential is not screened in the middle of small dots so the band minimum rises, decreasing the level spacing. The first excited state of one of our one-electron dots is typically 1–3 meV above the ground state. In GaAs dots, almost always $\Delta < E_c$, although in some other systems (nanotubes, for example) this is not necessarily the case.

In addition to the Hamiltonian of the dot itself, the source and drain reservoirs ($\alpha \in \{S, D\}$) have energies

$$H_\alpha = \sum_{k,\sigma} \epsilon_k N_{\alpha k\sigma} \tag{3.6}$$

where k are states in the leads (plane waves if we assume the leads are clean 1D channels) with spins σ and occupations $N_{\alpha k\sigma}$ which usually[4] follow a Fermi distribution $N(\epsilon) = 1/(1 + e^{\frac{\mu_\alpha - \epsilon}{kT_\alpha}})$ based on the chemical potential $\mu_\alpha = -eV_\alpha$ and temperature T_α of the reservoir. The reservoirs couple to the dot via terms

$$H_{QD-\alpha} = \sum_{i,k,\sigma} t_{i\alpha k\sigma}(c^\dagger_{i\sigma} c_{\alpha k\sigma} + h.c.) \tag{3.7}$$

which link creation and annihilation operators $c^\dagger$ and c in the dot with those in the leads via tunneling elements $t_{i\alpha k\sigma}$ that depend on the particular form of the i-th wavefunction in the dot (whether, for instance, it has a node in the vicinity of the tunnel barrier[5]) and can in principle be functions of energy or spin of electrons in the leads as well.[6] *h.c.* denotes the Hermitian conjugate. Fermi's golden rule yields a transition rate into and out of each level in the the dot based on these tunneling

---

[4] See Ref. [51] for an application in which a non-Fermi distribution is created and studied.

[5] See Ref. [52] for a description of this variation using random matrix theory, applicable to large dots.

[6] Refs. [53, 54] use spin-split Landau levels to load particular spins into a dot, and Ref. [55] discusses a similar scheme in parallel (Zeeman) field.

amplitudes,

$$\Gamma_{\alpha i\sigma} = 4\pi\rho(\epsilon_{i\sigma})|t_\alpha|^2 \tag{3.8}$$

where $\rho(\epsilon_{i\sigma})$ is the density of states in lead α at the energy of the dot level.[7] Γ has units of energy, from which the tunneling time is given by $t_{\alpha i\sigma} = \hbar/\Gamma_{\alpha i\sigma}$. Γ has additional significance as the lifetime broadening of the states in the dot.

Once the dot is closed and charge is quantized, we encounter the phenomenon of *Coulomb blockade*. At most values of gate voltage only one charge state is allowed, so no charge may be added to or removed from the dot, and conductance is suppressed. Consider first the condition $V_{sd} = 0$ (for simplicity, choose $V_s = V_d = 0$). Ignoring for the moment the quantum confinement term and adding an irrelevant term depending only on gate voltage, we can rewrite Eq. 3.5 as

$$H_{dot} = (E_c/2)(N - N_g)^2 \tag{3.9}$$

where $N_g = C_g V_g/e + 1/2$. The gate charge N_g increases linearly with gate voltage, but in the ground state, the real charge N on the dot rounds this to the nearest integer, as depicted in Fig. 3.2(b). The only values of gate voltage at which conductance is allowed are where N_g is close to a half-integer $n + \frac{1}{2}$, at which point electrons may pass through the dot one at a time, alternating between charge states n and $n + 1$. This leads to conductance spikes as a function of gate voltage, with a period $\Delta V_g = e/C_g$ (Fig. 3.2(b), bottom panel).

In total there are five energy scales relevant to transport through a quantum dot,

---

[7] ρ here is the absolute density of states, with units of inverse energy, not the usual density per unit length. As the length of the lead is increased, ρ increases linearly, while the tunneling elements t vary as the inverse square root of lead length since they are proportional to individual wavefunction amplitudes. Thus, Γ tends to a constant as lead size diverges.

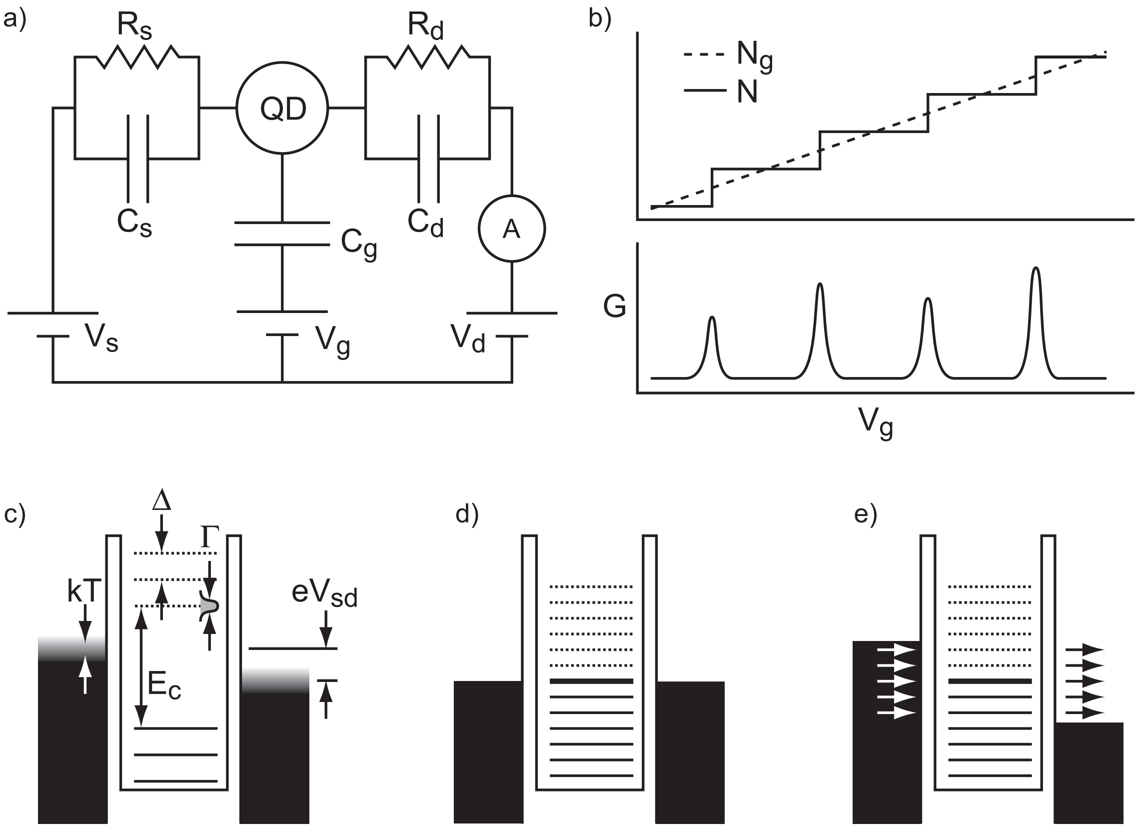

Figure 3.2: Schematic description of a quantum dot. a) Circuit equivalent of a quantum dot, showing voltages and capacitances of the source, drain, and gate, tunneling "resistances" to the source and drain, and the current measurement for calculating conductance. b) The smooth gate charge N_g, resulting dot charge N, and conductance spikes characteristic of Coulomb Blockade. c) Five energy scales determine behavior of a closed quantum dot. A gap E_c opens up between the occupied n-electron states (solid lines) and unoccupied $n+1$-electron states (dotted lines), which are spaced by Δ and tunnel-broadened by Γ, while the leads are characterized by temperature kT and bias eV_{sd}. A transport resonance condition in the quantum regime d) at zero bias, where current flows through only the ground state, and e) at $V_{sd} > \Delta$, through ground and excited states. The thick solid line represents the newly occupied state in the $n+1$-electron ground state. The thin solid and dotted lines represent states filled or empty, respectively, in the ground states of both occupancies.

shown on a generic level diagram in Fig. 3.2(c). Two involve the structure of the dot (E_c and Δ), two concern the leads (kT and eV_{sd}), and one describes the coupling between them (Γ).[8] The first question is what determines whether the dot is open or

---

[8] To determine the conductance through the dot it is necessary to know the tunnel rate to each lead, but for delineating regimes of different behavior only their sum is relevant.

closed. The Hamiltonian Eq. 3.5 is only valid if charge in the dot is quantized, but when the dot is open, charge in the leads flows continuously into the dot to screen charge excitations. There are three ways I know of to get at this crossover, which all seem independent until they arrive remarkably at the same answer. First, we may simply stipulate that the entrance and exit must be tunnel barriers, since this constrains motion through the barrier that would allow screening. In other words, $G_\alpha < e^2/h$. A second, more satisfying route involves the energy-time uncertainty relation, noting that charge may only be quantized if energy can be resolved to better than E_c. The time that determines energy resolution is the charge relaxation time $R_\alpha C_\Sigma = C_\Sigma/G_\alpha$, and using $\Delta E \Delta t > h$ again leads directly to $G_\alpha < e^2/h$.

Finally, for a golden-rule approach to be valid and not give way to higher-order processes (which in turn screen the charge), the energy spectrum in the dot must be well-resolved, meaning that $\Gamma < \Delta$. Although it doesn't explicitly make sense to talk about a resistance unless the barrier connects two continuums, we can regard the resistance as a property of the barrier independent of what states it connects, and calculate it by approaching the continuum limit in the dot. One way to do this without changing the properties of the dot (i.e. letting $\Delta \to 0$) is to assume a large bias across the barrier so that tunneling is allowed into $n = eV/\Delta$ states. The current across the barrier is $I = e\frac{dN}{dt} = en\Gamma/\hbar = V\frac{e^2}{\hbar}\frac{\Gamma}{\Delta}$ and dividing by voltage gives

$$G = \frac{e^2}{\hbar}\frac{\Gamma}{\Delta}. \tag{3.10}$$

Within a factor of 2π, the condition $\Gamma < \Delta$ is then equivalent to $G < e^2/h$.

The heirarchy $\Gamma < \Delta < E_c$ for Coulomb-blockaded dots yields four temperature ranges, each with its own distinct behavior. The effect of temperature is to broaden the step from filled to empty states in the reservoirs by the Fermi function, with an energy width proportional to kT. At the highest temperatures, $kT > E_c$, conductance is never fully suppressed, because thermal excitations can always access multiple charge states, and conductance may show weak oscillations with period e/C_g if kT is only somewhat larger than E_c. This limits large closed dots ($E_c \sim 100\mu$eV) to use well below 1 K ($= 86\mu$eV) and for practical purposes they are best studied in dilution refrfigerators at below 100 mK. Small dots, where the energy scales are larger, may be studied in warmer cryostats (^{3}He at 300 mK or ^{4}He at 1 K), however even the small-dot experiments presented here were performed in a dilution refrigerator for maximum energy resolution.

The range $\Delta < kT < E_c$ is known as classical Coulomb blockade, because while transport is fully suppressed away from resonance and on resonance only two charge states contribute, multiple energy levels are available within each charge state. Levels in the dot are filled according to a Fermi distribution, just like states in the lead, and the convolution of these three Fermi functions gives a peak with $\cosh^{-2}$ voltage profile (i.e. exponential tails) and a full width at half maximum (FWHM) of $4.3kT$ when scaled by the lever arm C_g/C_Σ relating voltage changes on the gate to energy changes in the dot.

Cooling further (or using smaller dots) we reach the quantum Coulomb blockade regime, $kT < \Delta$, where only one energy level is involved in transport. This regime is divided further into the thermally broadened regime $\Gamma < kT$ (warmer or more closed barriers) and the lifetime-broadened regime $\Gamma > kT$ (cooler or more open barriers). Thermally broadened peaks still have a $\cosh^{-2}$ voltage profile but now only two Fermi functions (one for each lead) are convolved and the scaled FWHM drops to $3.5kT$. In addition, the peak height decreases as temperature increases, whereas in classical blockade the peak height is roughly constant with temperature. In the lifetime-broadened regime, all Fermi functions are out of the picture, and instead the voltage profile of the peak is Lorentzian (i.e. polynomial tails) characteristic of a resonance damped by decay to the leads. The quantum Coulomb blockade regime is accessible in a dilution refrigerator for dots containing several hundred electrons or less ($\Delta > 50\mu$eV), which describes all of the dots used in this thesis. What makes this regime interesting is that charge motion is dependent on the properties of the individual quantum state being accessed, and many of these properties can be deduced from measurable quantities like peak position and height, and how these change in magnetic fields. In addition, as we will see in Ch. 9, this regime allows preparation of a known quantum state which can then be manipulated to perform more complicated dynamics studies.

Figure 3.2(d) shows the spectrum of single-particle levels available at the n to $n+1$ electron resonance with zero source-drain bias. In the quantum Coulomb blockade regime at this condition, current flows through only the thick-lined state, which is empty in the n-electron ground state and filled in the $n+1$-electron ground state. The charging energy gap is now effectively absent from the system: higher energy levels (dashed lines) are available to accept electrons when the thick state is vacant, and lower energy levels are available to eject electrons when the thick state is filled without paying the charging energy cost. At zero bias such processes are forbidden because the occupation of states in the leads exactly matches the occupation within the dot, and no filled and empty levels exist at the same energy. But at sufficient source-drain biases, so long as the thick state remains between the two Fermi levels, these processes are allowed. Current through the dot changes whenever one of these states passes either the source or drain Fermi level, enabling excited-state spectroscopy of the dot by measuring current vs. V_g and V_{sd} [50].

3.3 Double dots

A QPC by itself couples two continuums to each other, and a single quantum dot couples a continuum to a discrete set of states. We can investigate the coupling between two discrete spectra by creating two quantum dots tunnel-coupled to each other. The circuit equivalent of a double dot is shown in Fig. 3.3(a). The key new features are the mutual capacitance and interdot tunneling, denoted by C_m and R_m, which parametrize the interaction between the two dots. Likewise, following Ref. [40], we can build up the double-dot Hamiltonian from single-dot components plus a term for each form of interaction,

$$\begin{aligned} H_{DQD} &= \frac{E_{c1}}{2}N(N-1) - \frac{NE_{c1}+ME_m}{e}(C_{g1}V_{g1}+C_sV_s) + \sum_{i,\sigma} N_{i\sigma}\epsilon_{i\sigma} \\ &+ \frac{E_{c2}}{2}M(M-1) - \frac{ME_{c2}+NE_m}{e}(C_{g2}V_{g2}+C_dV_d) + \sum_{j,\sigma} M_{j\sigma}\epsilon_{j\sigma} \\ &+ E_m NM + \sum_{i,j,\sigma} t_{ij\sigma}(c^{\dagger}_{i\sigma}c_{j\sigma} + h.c.). \end{aligned} \tag{3.11}$$

Here N and M are the occupations of the left and right dots, and defining $C_{1(2)}$ as the total capacitance of the left (right) dot, the single dot charging energies are given by

$$E_{c1(2)} = \frac{e^2}{C_{1(2)}}\left(1 - \frac{C_m^2}{C_1C_2}\right)^{-1} \tag{3.12}$$

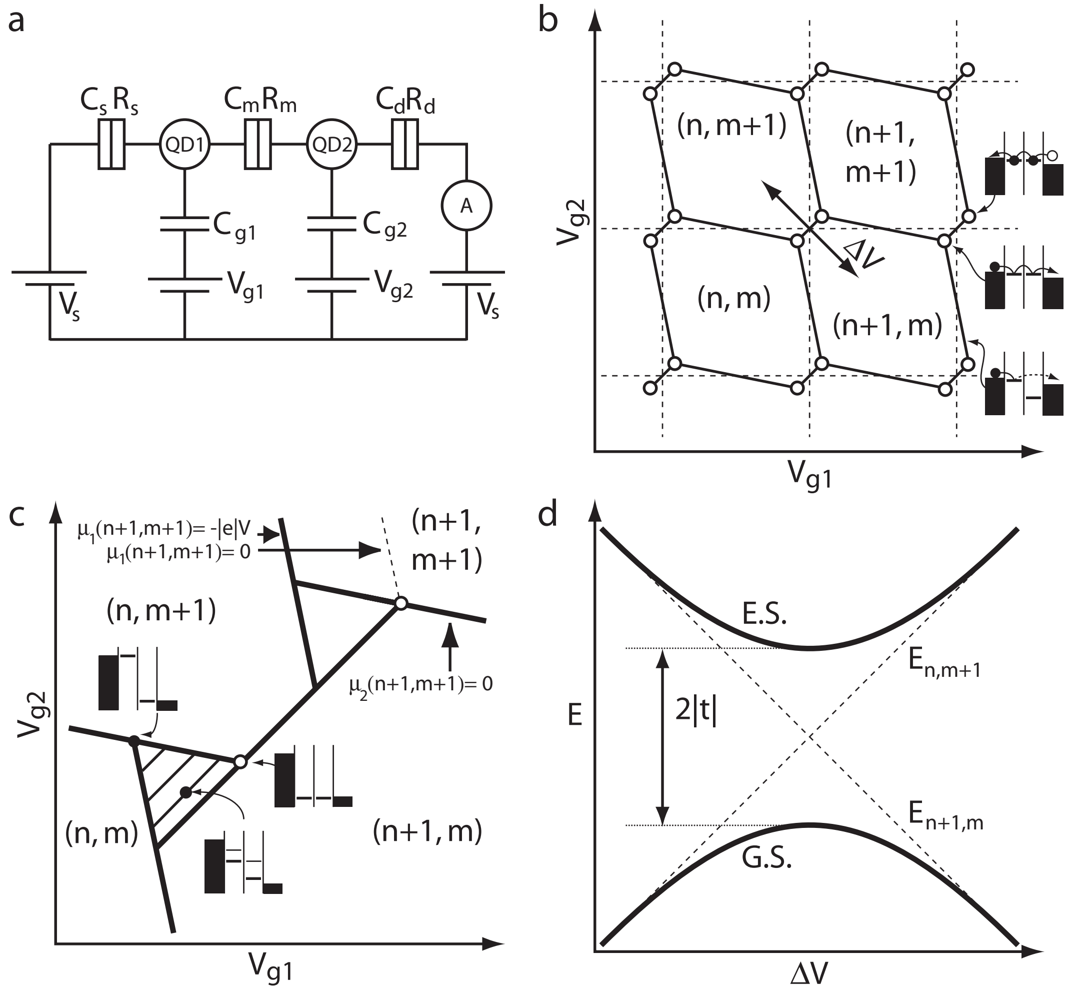

Figure 3.3: Double quantum dots. a) Circuit equivalent of a double dot. The double boxes represent a capacitor and resistor in parallel. b) At zero source-drain bias, the ground state charge is constant within hexagonal regions in the V_{g1}–V_{g2} plane. Ordered pairs (n, m) denote charge on the left and right dots respectively. Current can only flow at the vertices, called *triple points*, where three charge states are in equillibrium. The upper one (top diagram) is called the hole triple point and the lower one (middle diagram) the electron triple point. When the dots are fairly open, conduction is sometimes seen along the hexagon edges as well, due to cotunneling processes as in the bottom diagram. When considering two states of the same total charge, e.g. $(n, m+1)$ and $(n+1, m)$, the relevant parameter is *detuning*, or motion away from equal energy such as the line labeled ΔV. c) At finite source-drain bias, the triple points expand into triangles. Ground-state-to-ground-state transport occurs along the base of each triangle ($\Delta V = 0$), and excited states are manifest as lines of current parallel to the ground state line. d) Due to a finite tunnel coupling t between the dots, two states of the same total charge will hybridize, displaying an avoided crossing as a function of detuning. Figure adapted from [40] and [56].

and the mutual charging energy (the extra energy needed to add an electron to one dot due to a single electron on the other) is

$$E_m = \frac{e^2}{C_m}\left(\frac{C_1 C_2}{C_m^2} - 1\right)^{-1} \tag{3.13}$$

Tunnel elements $t_{ij\sigma}$ connect states i in the left dot with states j in the right dot, conserving the spin σ. The full Hamiltonian contains additional terms corresponding the lead and to dot-lead couplings, which are identical to their single-dot counterparts.

The only additional approximations incorporated in Eq. 3.11 beyond those made for single dots are that cross-capacitances are zero (e.g. from gate 1 to dot 2—this is a fairly trivial assumption to remove, by using linear combinations of V_{g1} and V_{g2}.) and that the tunneling elements are small enough that the two dots are really distinct, and as far as charging effects are concerned electrons are localized on one dot at a time. As with single dots, we can make the equivalent assertions that electron localization begins when the RC time is long enough to resolve the charging energies or when the barrier has a tunneling conductance ($G_m < e^2/h$). We can also guess that strong mixing of states in the two dots would occur when the tunneling elements $t_{ij\sigma}$ become equal to the level spacing Δ of each dot (which we assume are equal for simplicity). Barrier conductance is perhaps even less meaningful in a double dot than in a single dot, but we can relate it to the tunneling elements through Eqs. 3.8 (taking $\rho = 1/\Delta$) and 3.10, yielding $G_m = 4\pi\frac{e^2}{h}(\frac{t}{\Delta})^2$. Again, to within a constant, all three approaches give the same condition, $t < \Delta$, for the dots to be well-separated.

As with single dots, we begin by considering only the classical terms in Eq. 3.11, omitting the last term on each line which is a purely quantum effect, and for the moment set the source and drain voltages to zero to examine the ground state of the system. With the substitutions $N_g = C_{g1}V_{g1}/e + K_1$ and $M_g = C_{g2}V_{g2}/e + K_2$ where $K_{1(2)} = \frac{1}{2}\frac{1-E_m/E_{C1(2)}}{1-E_m^2/E_{C1}E_{C2}}$ is just a constant offset,[9] we can rewrite the classical energy as

$$U(N, M) = \frac{1}{2}E_{c1}(N - N_g)^2 + \frac{1}{2}E_{c1}(N - N_g)^2 + E_m(N - N_g)(M - M_g). \quad (3.14)$$

Because $E_m^2 < E_{c1}E_{c2}$,[10] $(N, M) = (N_g, M_g)$ is the ground state charge configuration for every set of gate voltages such that N_g and M_g are integers. In V_{g1}–V_{g2} space, therefore, the ground states map out a grid. In the limit of $E_m = 0$, the charge transitions in each dot exactly follow the gridlines of that dot's own gate irrespective of the other gate voltage, shown by the dotted lines in Fig. 3.3(b). Current would pass through the system only at the intersections, where four charge states would be degenerate. Finite mutual charging is equivalent to an energy term depending on the total double-dot occupation $N + M$, and because the lower left and upper right states at this intersection differ in total occupation by two (one in each dot), the mutual charging term breaks their degeneracy and splits the intersection point into two, called *triple points* because three charge states are degenerate. With this splitting, each charge configuration is the ground state over a hexagonal region in gate space, tiling into a honeycomb pattern as indicated by the solid lines in Fig. 3.3(b).

Current flows at both triple points by the same tunneling processes and through the same states in each dot, however the order of tunneling events is different depending on whether the doubly-empty or doubly-occupied charge state completes the conduction

---

[9] This offset, like the 1/2 offset in the single-dot case, arises from the $N(N-1)$ factor (rather than N^2) due to the quantized charge on the dot. In practice it is irrelevant because we don't know beforehand what voltage should correspond to a zero-electron dot, which is likely why many authors simply use N^2 and ignore the offset.

[10] This can be shown to always be true, using Eqs. 3.12 and 3.13 and the fact that C_1 and C_2 are sums which both include C_m.

cycle. Consider a small increase in the Fermi energy of the left lead (i.e. a negative voltage) such that electrons flow from left to right. At the upper, or "hole" triple point (top diagram in Fig. 3.3(b)), we can think of the doubly-occupied state as the initial state, and a single hole enters from the right lead, hops from the right dot to the left, then escapes to the left lead. At the lower, or "electron" triple point (middle diagram), the doubly-empty state can be thought of as the initial state, and an electron enters from the left, hops from the left dot to the right, and escapes to the right lead. The result is the same, and barring any voltage or mutual charging dependence of the tunnel rates the current will be the same.

Experimentally, current is often seen along the honeycomb edges as well as at the triple points. This requires a cotunneling event as shown in the bottom diagram in Fig. 3.3(b). The left dot is at a charge resonance, so an electron can tunnel from the left lead to the left dot, then to get to the right lead it may virtually transit through an energetically forbidden state in the right dot. A similar process can occur on the short honeycomb edge connecting the two triple points. On this edge an electron may occupy either dot, but it is energetically forbidden for it to exit or for another electron to enter. With the existing electron in the right dot, a virtual process can simultaneously eject that electron to the right lead and bring a new electron from the left lead into the left dot.

When a large source-drain bias is applied across the double dot, each triple point expands into a triangle satisfying $-|e|V \geq \mu_1 \geq \mu_2 \geq 0$, as shown in Fig. 3.3(c). This describes the case of $V_d = 0$ and $V_s = V$, where V is negative (higher energy). If V is positive, the inequalities are reversed. The chemical potentials μ_1 and μ_2 are simply the energies to add the last electron to the left or right dot with the other dot occupied as required at that triple point. In the electron triangle, for example, the relevant chemical potentials are $\mu_1(n+1,m) = U(n+1,m) - U(n,m)$ and $\mu_2(n,m+1) = U(n,m+1) - U(n,m)$. Within the bias triangles we begin to see the effects of quantized energy levels in the dots. Fully elastic transport from one ground state to the other is allowed only along the lower right edge of the triangle, where $\mu_1 = \mu_2$, and consequently this edge is usually a current maximum. If $|eV| > \Delta$, additional lines of high current appear parallel to the ground state line due to transport through excited states, as shown by the lower diagram in Fig. 3.3(c). The remaining area of the triangle is typically filled in with weaker current due to inelastic transitions from the left dot to the right dot involving emission of either a phonon or a photon.

The one term in the Hamiltonian Eq. 3.11 we have yet to consider is the tunnel coupling between the two dots (although in the previous section we implicitly assumed that some tunneling could occur). This term affects energy levels in the dots only in the vicinity of the triple points and the short honeycomb segment connecting them. In this neighborhood we can think of the double dot as a two-level system (the ground states of $(n,m+1)$ and $(n+1,m)$) with the bare detuning between them parametrized by a gate voltage ΔV along a diagonal line as shown in Fig. 3.3(b). The tunnel coupling then produces an avoided crossing between these levels (Fig. 3.3(d)) during which the two states hybridize and the ground state passes one electron smoothly from one dot to the other. The hyperbolic shape of the avoided crossing is reflected in the triple points, which at large tunnel coupling begin to push apart and stretch into crescents, smoothly connecting the two longer honeycomb edges coming into each triple point.

3.4 Charge sensing

While anyone studying the 0.7 structure would call QPC traces such as Figs. 3.1(d)–(g) unacceptibly dirty, for their purpose in this thesis—charge sensing—they are all just fine. Charge sensing is the use of a conduction path to infer the number and/or location of nearby charges. The only requirement to be able to do this is that the conduction path be acutely sensitive to the local electrostatic environment, so that when an electron moves nearby—into or out of a quantum dot, or from one dot to another—the conductance of the path changes.

Conceptually, the technique of charge sensing is identical to a field effect transistor—one might even call charge sensors "single-electron FETs." There are fundamental quantum mechanics questions involved in charge sensing, because it is a form of measurement and therefore exerts a complementary backaction on the system being measured. For the experiments in the following chapters this backaction will be negligible in most cases, because the sensors are weakly driven or weakly coupled to the system being sensed, such that the measurement timescale is much longer than other electron dynamics.

There is no fundamental limit to the sensitivity of a charge sensor. The location of a single electron could in principle determine whether a nearby conduction path is fully opaque or fully transparent, and it has been shown (albeit for fairly low on-state conductances) that one may alter conductance by more than two orders of magnitude (see Ref. [57] and Ch. 4). However, most of the charge sensors used in this thesis have much lower sensitivities, primarily because the sensed electron is screened by a gate between it and the sensor channel. The key feature of charge sensing relative to transport measurements is that they do not require fast processes within the dots being measured in order to generate a measureable current. Electrons may move faster than the measurement time, in which case the sensor will measure an average property as is done in transport measurements, or they may move more slowly than the measurement,[11] in which case every event may be recorded individually, known as a *single-shot* measurement. In some cases (see Ch. 6) the electrons may never visit any reservoir, so they will generate no current whatsoever, but as long as their positions change they may be studied via charge sensing. The experiments in the following chapters explore some of the behavior of charge sensors and their interaction with single and double quantum dots, then use them as tools to investigate some otherwise inaccessible energetics and dynamics in double dots.

---

[11] Measurements as fast as several μs have been performed in GaAs systems [58, 55].

Chapter 4

Coulomb-modified Fano resonance in a one-lead quantum dot

A. C. Johnson, C. M. Marcus
Department of Physics, Harvard University, Cambridge, Massachusetts 02138
M. P. Hanson, A. C. Gossard
Department of Materials, University of California, Santa Barbara, California 93106

We investigate a tunable Fano interferometer consisting of a quantum dot coupled via tunneling to a one-dimensional channel. In addition to Fano resonance, the channel shows strong Coulomb response to the dot, with a single electron modulating channel conductance by factors of up to 100. Where these effects coexist, lineshapes with up to four extrema are found. A model of Coulomb-modified Fano resonance is developed and gives excellent agreement with experiment.[1]

---

[1] This chapter is adapted from Ref. [59]

4.1 Introduction

The interplay between interference and interaction, in its many forms, is the central problem in mesoscopic physics. In bulk systems, screening reduces the strong repulsion between electrons to a weak interaction between quasiparticles, but in confined geometries electron-electron interaction can dominate transport. The Fano effect—an interference between resonant and non-resonant processes—was first proposed in the context of atomic physics [60]. More recently, Fano resonances have been investigated in condensed matter systems, including surface impurities [61], quantum dots [62, 63, 64, 65, 66], and carbon nanotubes [67], and have generated interest as probes of phase coherence [68, 69] and as possible spin filters [70]. These studies have treated Fano resonance as purely an interference effect. When the resonant channel is a tunneling quantum dot, however, Fano resonance coexists with Coulomb interaction that appears in single-dot transmission as the Coulomb blockade. In the Fano regime, the coexistence of Coulomb and interference effects leads to new transport regimes that to date have not been investigated theoretically or experimentally.

In this chapter, we present measurements of a Fano interferometer consisting of a quantum dot coupled to a one-dimensional channel. We have independent control of all couplings defining the resonant and non-resonant processes, allowing us to identify and investigate several regimes of behavior. With the channel partially transmitting but not allowing tunneling into the dot, a charge sensing effect is observed whereby channel conductance responds to the number of charges on the dot [71, 72, 73]. Alternatively, if the dot-channel barrier is lowered, and the conducting path pushed towards the dot, a regime emerges in which all transmitted electrons pass through

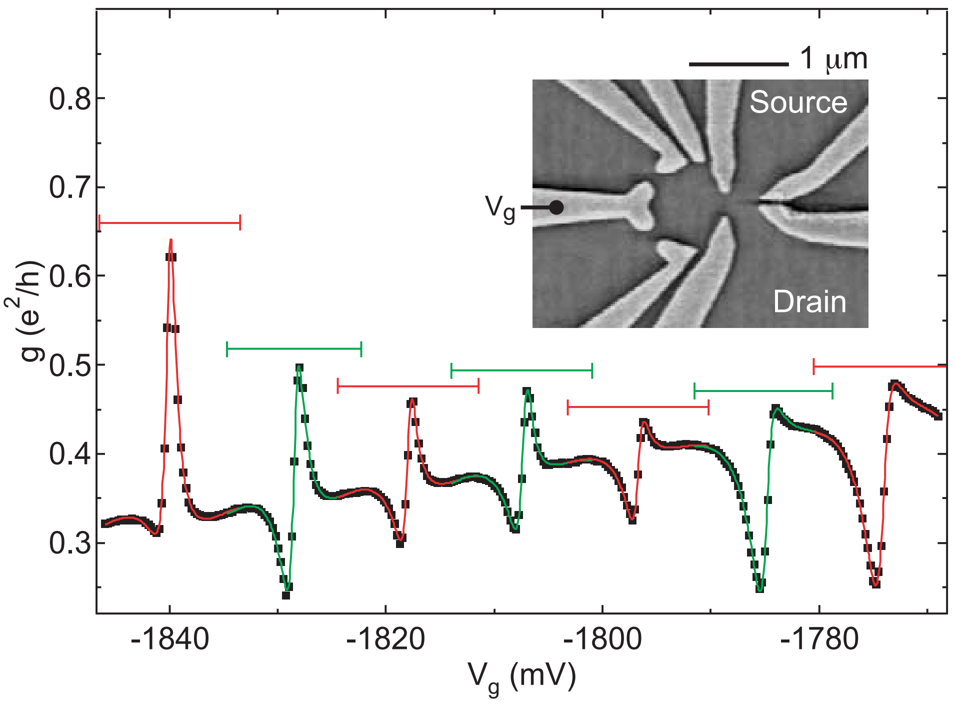

Figure 4.1: Channel conductance data (squares) and fits (curves) vs. gate voltage V_g in the Fano regime. Bars show fitting ranges. Inset: SEM image of a similar sample, a quantum dot coupled by one lead to a conducting channel.

the dot, and standard Coulomb blockade resonances result. Between these extremes lies the Coulomb-modified Fano regime, in which resonant tunneling via the dot and direct channel transmission coincide. Fano resonances appear throughout this regime, generally in conjunction with charge sensing. We develop a model that combines these two effects and successfully describes the data. With this model, resonance parameters are extracted and used to evaluate interaction effects.

The device (inset to Fig. 4.1) consists of a 0.5 μm^2 quantum dot and a constriction, all defined by Cr-Au depletion gates on a GaAs/AlGaAs heterostructure grown by MBE. The two-dimensional electron gas lies 100 nm below the surface, with density 2×10^{11} cm^{-2} and mobility $2{\times}10^5$ cm^2/Vs. The dot contains $\sim$ 600 electrons and has level spacing $\Delta \sim 20$ μeV. The experiment was performed in a dilution refrigerator with an electron temperature of 50 mK, in a magnetic field of 0 to 200 mT perpendicular to the device plane. Conductance was measured using a lock-in amplifier with 10 μV excitation at 15.7 Hz.

Figure 4.1 shows conductance in the Fano regime as a function of gate voltage V_g over a range containing seven resonances. A progression of lineshapes is seen, each comprising a dip and a peak similar to Fano resonance. The non-interacting Fano lineshape, given by Eq. 4.1 below, is insufficient to explain these data. However, a model incorporating Coulomb interaction (described below) provides improved fits, as seen in Fig. 4.1.

4.2 Device behavior

We first discuss qualitatively the limiting regimes with the dot either capacitively or tunnel coupled to the channel, as well as the intermediate case, the Coulomb-modified Fano regime. When the channel is tuned to partially transmit one mode, but there is no conductance between channel and dot, sawtooth patterns such as Fig. 4.2(a) appear. These can be explained by considering a single effective gate, combining the effects of the metal gate and the dot charge, that smoothly modulates g, the channel conductance. Every electron residing on the dot has a gating effect on the channel, modifying the effective gate voltage by an amount V_s, which we denote the *sensing voltage*. Each time a charge is added to the dot (as V_g is made more positive), the effective gate voltage jumps by V_s, causing g to jump to the value it had at a gate voltage more negative by V_s. If g is a decreasing (increasing) function of V_g, this results in an upward (downward) jump. For this device V_s is typically ~80% of the

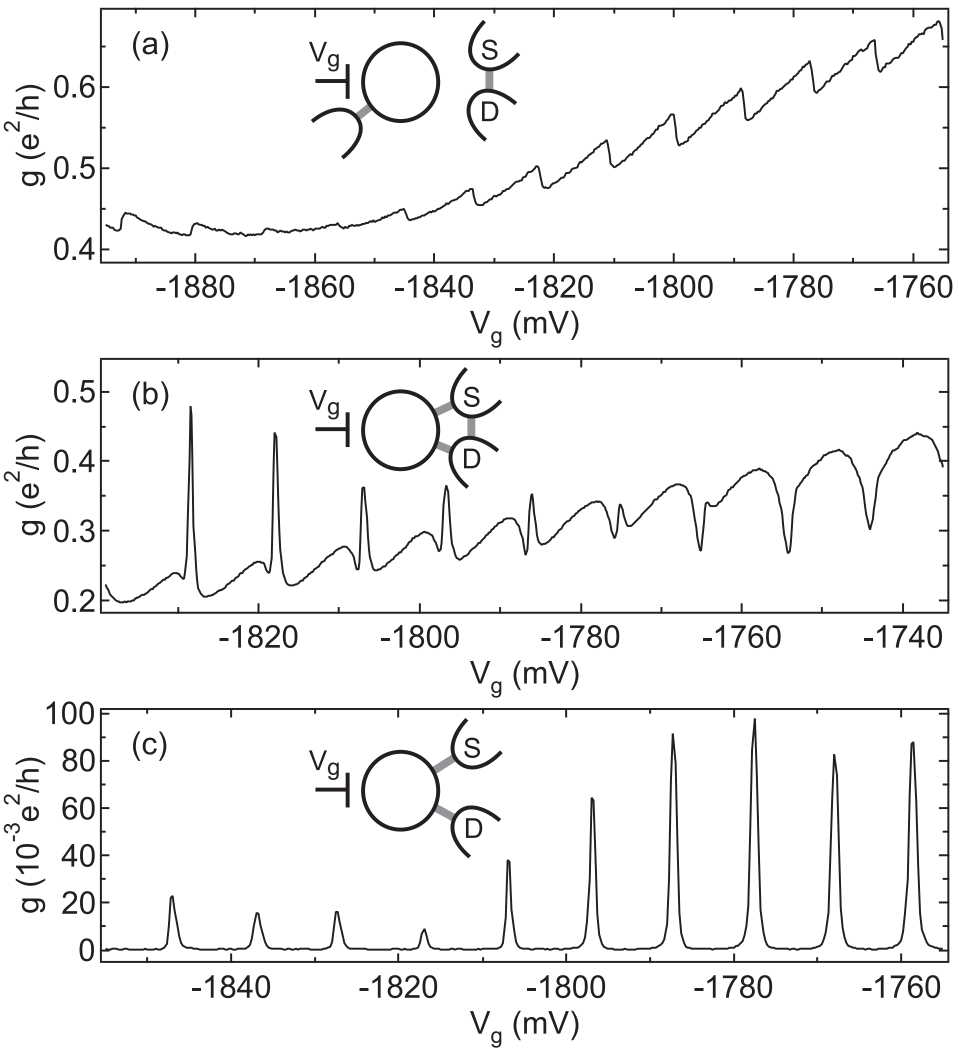

Figure 4.2: Three configurations with a tunnel coupled dot. Drawings indicate tunneling paths. (a) Pure charge sensing: the dot couples capacitively to the channel and tunnels weakly to a third reservoir. (b) Fano resonance with charge sensing: tunneling between the channel and the dot interferes with direct transmission. (c) Breit-Wigner resonances: the only conducting path is through the dot.

spacing between jumps, indicating that the channel is more sensitive to excess dot charge than to the gate directly.

The Coulomb-modified Fano regime emerges as tunneling is introduced between the dot and the channel. When the charge sensing effect is relatively weak, such as in Fig. 4.1, features clearly resembling non-interacting Fano resonance are observed. In other cases, for example Fig. 4.2(b), the charge-sensing jump is comparable to or larger than the peak of the Fano resonance. In this regime, combining the charge-sensing jump with the dip-peak pair of Fano resonance, one resonance can have up to four extrema.

When direct conductance is made much smaller than conductance through the dot, the direct path (through the channel) no longer interferes significantly with the resonant path (though the dot). In this limit, the Fano regime crosses over to the familiar Coulomb blockade regime, yielding simple single resonances as seen in Fig. 4.2(c).

Before analyzing the Fano regime in detail, we turn our attention to features that can appear as Fano resonance but are actually a result of charge sensing. Figure 4.3 shows the effect of quantized charge in the dot on a resonance in the channel, in the absence of any tunneling between the two. Channel conductance was measured while tuning the coupling between the dot and a third reservoir. When the tunnel rate to the third reservoir is low (Fig. 4.3(a)), one finds smooth segments punctuated by jumps. The dotted curves are identical forms offset by $V_s = 4.0$ mV, indicating how channel resonances would appear for an isolated dot occupied by $n = N$ or $n = N + 1$ electrons. If this family of curves is extended to all n, it overlays every segment of the data, though the jumps from one curve to the next are irregularly spaced and change position if the sweep is repeated. We identify these jumps as single tunneling events, and estimate a tunneling time $\hbar/\Gamma$ here of order seconds, based on motion of the jump point upon repeating sweeps.

As tunneling to the third reservoir is increased (Fig. 4.3(b)), jumps become periodic and repeatable, but there remains a family of evenly spaced curves onto which all of

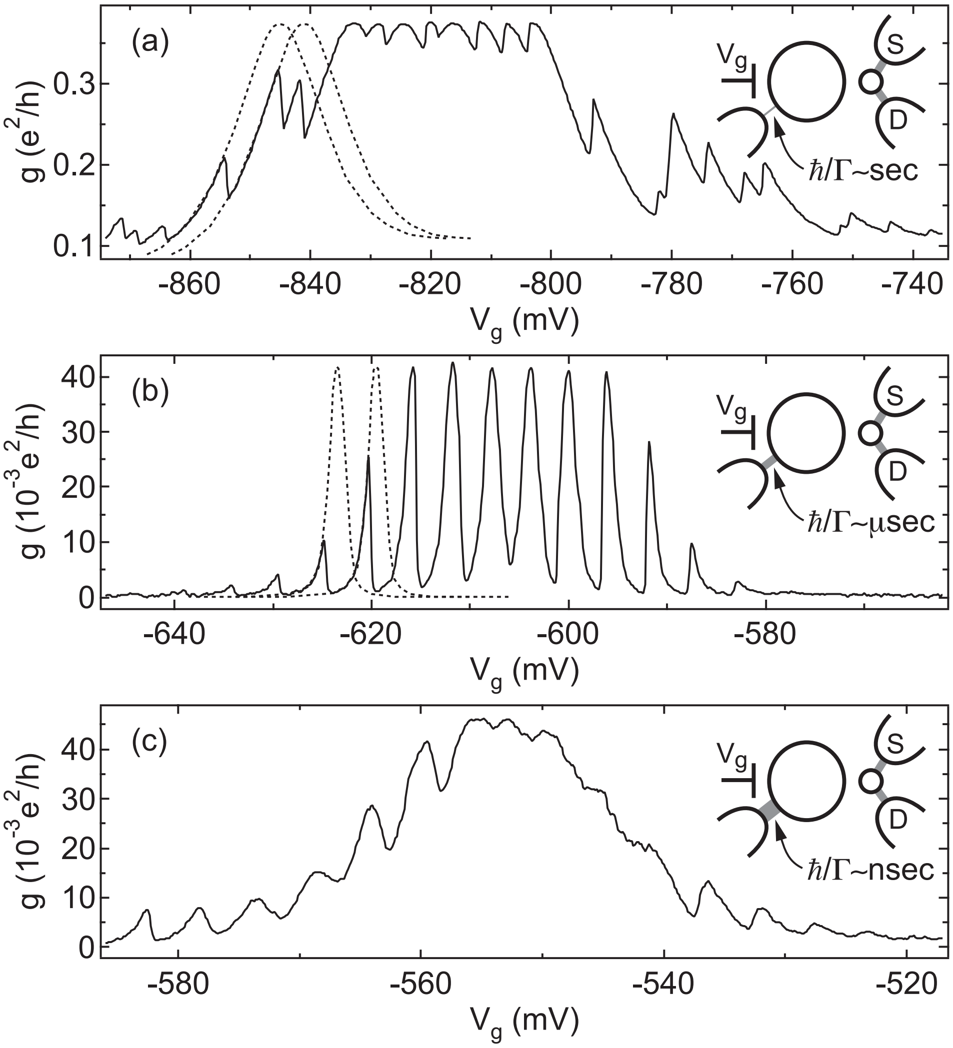

Figure 4.3: Charge sensing by a channel resonance. Drawings indicate the tunneling rate to the extra lead. Dotted curves show how the full resonance would look with dot charge fixed at two consecutive values. (a) With the dot nearly isolated, jumps between these curves are sharp, erratic and unrepeatable. (b) Increase tunneling and the jumps become periodic and repeatable. (c) With the dot nearly open, the jumps broaden and resemble an oscillation superimposed on a single, broad resonance.

the data falls. In this case the channel resonance is much narrower, and adding a single charge to the dot shifts the channel from directly on to far off resonance. This single-electron switch has an on/off conductance ratio of 20. Traces with still narrower resonances show on/off ratios >100, as in other recent reports [74, 57]. Notice, however, the similarity between these asymmetric line shapes and Fano resonances, even though this is pure charge sensing.

Still greater coupling of the dot to the third reservoir yields lifetime-broadened transitions. This is the case in Fig. 4.3(c), where the dominant feature is a single broad resonance, modulated by weak charge quantization in the dot. This motivates an important feature of the model, that the Fano resonance and the charge-sensing jump, since both result from the same process, have a single width parameter Γ.

4.3 Model for Coulomb-modified Fano resonance

In the single-level transport regime, $kT < \Gamma < \Delta$, transmission through one discrete level produces a Breit-Wigner resonance, represented by a complex transmission amplitude $t = t_0/(\epsilon + i)$ with dimensionless detuning $\epsilon = (E - E_0)/(\Gamma/2)$. Here an electron of energy E encounters a resonance at E_0 with width Γ, and peak transmission t_0, accounting for lead asymmetry. Conductance is proportional to the transmission probability $|t|^2$, giving a Lorentzian lineshape [75]. A continuum channel can be added to the amplitude (coherently) or probability (incoherently), giving the non-interacting Fano lineshape,

$$g(E) = g_{inc} + g_{coh}\frac{|\epsilon + q|^2}{\epsilon^2 + 1}, \tag{4.1}$$

where g_{coh} (g_{inc}) is the coherent (incoherent) contribution to the continuum conductance. The Fano parameter q selects from a symmetric peak ($q = \infty$), symmetric dip ($q = 0$), or a dip to the left ($q > 0$) or right ($q < 0$) of a peak. The resonances in Fig. 4.1 evolve from $q = 2.5$ on the left to $q = 0.6$ on the right. In cases allowing arbitrary phase between the resonant and non-resonant paths, such as the Aharonov-

Bohm interferometer, q becomes complex. This is equivalent to increasing g_{inc}. In the present context, the interfering paths enclose no area, forcing a real q. This eliminates the ambiguity between g_{inc} and Imq, and constrains the Fano lineshape to maximum visibility [68].

The Coulomb-modified Fano effect can be modeled by extending Eq. 4.1 to include nearby resonances and charge sensing effects. We first write g as a sum over initial occupation numbers of the dot,

$$g(V_g) = \sum_n g_n(V_g) p_n(V_g). \tag{4.2}$$

If the dot contains n electrons, the only resonant processes allowed are the $n \rightarrow n+1$ and $n-1 \rightarrow n$ transitions, corresponding to the addition or removal of one electron. The contribution of the n-electron dot is thus

$$g_n(V_g) = g_{inc}(\widetilde{V}_n) + g_{coh}(\widetilde{V}_n) \left| 1 + \frac{q(\widetilde{V}_n) - i}{\epsilon_{n-} + i} + \frac{q(\widetilde{V}_n) - i}{\epsilon_{n+} + i} \right|^2 . \tag{4.3}$$

The allowed resonances have detunings $\epsilon_{n\pm} = (eV_g C_g / C_{tot} + E_{n \rightarrow n\pm 1})/(\Gamma/2)$, including a contribution from V_g (in energy units), with a lever arm given by the ratio of gate capacitance to total dot capacitance. The allowed resonances add coherently[2] to a direct conductance g_{coh}. g_{inc} is then added to account for multiple modes in the channel and explicit decoherence processes. Finally, each term is weighted by $p_n(V_g) = [\tan^{-1}(\epsilon_{n-} - \tan^{-1}(\epsilon_{n+})]/\pi$, the zero-temperature probability of occupation n. This can be derived from the Friedel sum rule, which relates changes δ in transmission phase to fractional changes in dot occupancy, $\delta(\arg(t)) = \pi\delta(\langle N \rangle) \bmod \pi$, where t is the Breit-Wigner transmission or reflection amplitude [77, 78].

---

[2] Adding amplitudes is an approximation which inflates the extracted coherence for poorly-separated resonances. Going beyond this requires choosing a microscopic model. See Ref. [76].

Charge sensing enters Eq. 4.3 via the effective gate voltage $\widetilde{V}_n = V_g - nV_s$. We expand dependences on $\widetilde{V}_n$ to first order, $q(\widetilde{V}_n) = q_0 + \frac{dq}{dV_g}$, and similarly for g_{coh} and $g_{tot} = g_{inc} + g_{coh}$. The slope $\frac{dg_{tot}}{dV_g}$ gives the charge-sensing sawtooth pattern, where charges in the dot affect the potential seen by charges in the channel. Nonzero $\frac{dq}{dV_g}$ and $\frac{dg_{coh}}{dV_g}$ produce subtle changes to the lineshape near resonance, and reveal how the potential seen by a charge in resonance depends self-consistently on its probability of being in the dot. As nearby resonances are generally similar in lineshape, the model assumes they obey the same linear expressions when calculating their influence on the tails of the resonance being fitted. This permits fitting with overlapping ranges as shown in Fig. 4.1, for more accurate determination of the charge-sensing parameters.

One limitation of this model deserves particular attention. A resonance in the channel makes conductance away from a dot resonance nonlinear on the scale of V_s, while the model assumes linearity. Thus, while the model trivially fits Fig. 4.2(a) by setting $g_{coh} = 0$, it cannot account for Fig. 4.3 in this manner. However, the asymmetric lineshapes in Fig. 4.3 give a somewhat plausible fit to the model. In order to unambiguously identify a Fano resonance, it is necessary that the off-resonant conductance varies linearly, which in turn requires that resonances be well separated so that background behavior can be isolated.

4.4 Analysis and discussion

Figure 4.4 shows fits to the model and the information this yields. Every resonance in Fig. 4.4(a) was fit four times, using all permutations of varying or fixing at zero the parameters $\frac{dq}{dV_g}$ and $\frac{dg_{coh}}{dV_g}$, to investigate whether this unusual sensing is necessary to explain the data. The results for one resonance are shown in Fig. 4.4(b). The first fit holds both parameters at zero while $\frac{dg_{tot}}{dV_g}$, V_s and the five parameters of a basic Fano resonance are varied. This reproduces all features qualitatively, but quantitative agreement is much poorer than with the latter three fits, which are nearly identical and agree with experiment to almost within the noise.[3] We therefore conclude that at least one of q and g_{coh} is subject to charge sensing, implying that the potential felt by the charge in resonance is modified by its own probability to be in the dot.

Finally, we consider parameter correlations among subsequent resonances. Figures 4.4(c)–(e) show g_{tot} and g_{coh}, Γ, and q extracted from each fit to each resonance in Fig. 4.4(a). Most trends are consistent with general arguments about tunneling wave functions: as g_{tot} increases, indicating a lower channel potential, Γ increases due to a lower tunnel barrier, and q decreases to keep peak conductance, given by $g_{inc} + g_{coh}(q^2 + 1)$, relatively constant. On top of this there appear to be fluctuations in g_{coh}, Γ, and q which are expected due to subsequent dot wave functions having different amplitudes near the barrier.

Two additional features stand out in the data. First, in many instances the fractional coherence g_{coh}/g_{tot} is roughly constant for several peaks then jumps abruptly to a different level for subsequent peaks, as occurs in Fig. 4.4 at $V_g = 1700$mV, while g_{tot} and other parameters evolve smoothly. Observed fractional coherence spans a range from $< 10\%$ to $> 50\%$,[4] likely due to multiple weakly transmitting modes in the

---

[3] In some cases all four fits are noticeably different, but a near-degeneracy is typical. Therefore, the fit is unreliable when both parameters are varied, hence the erratic behavior and large error bars on the parameters in red.

[4] This is a conservative bound from the ratio of minimum conductance to g_{tot}. Extracted g_{coh}/g_{tot} reaches 90%, because charge sensing raises the minimum even if $g_{inc} = 0$.

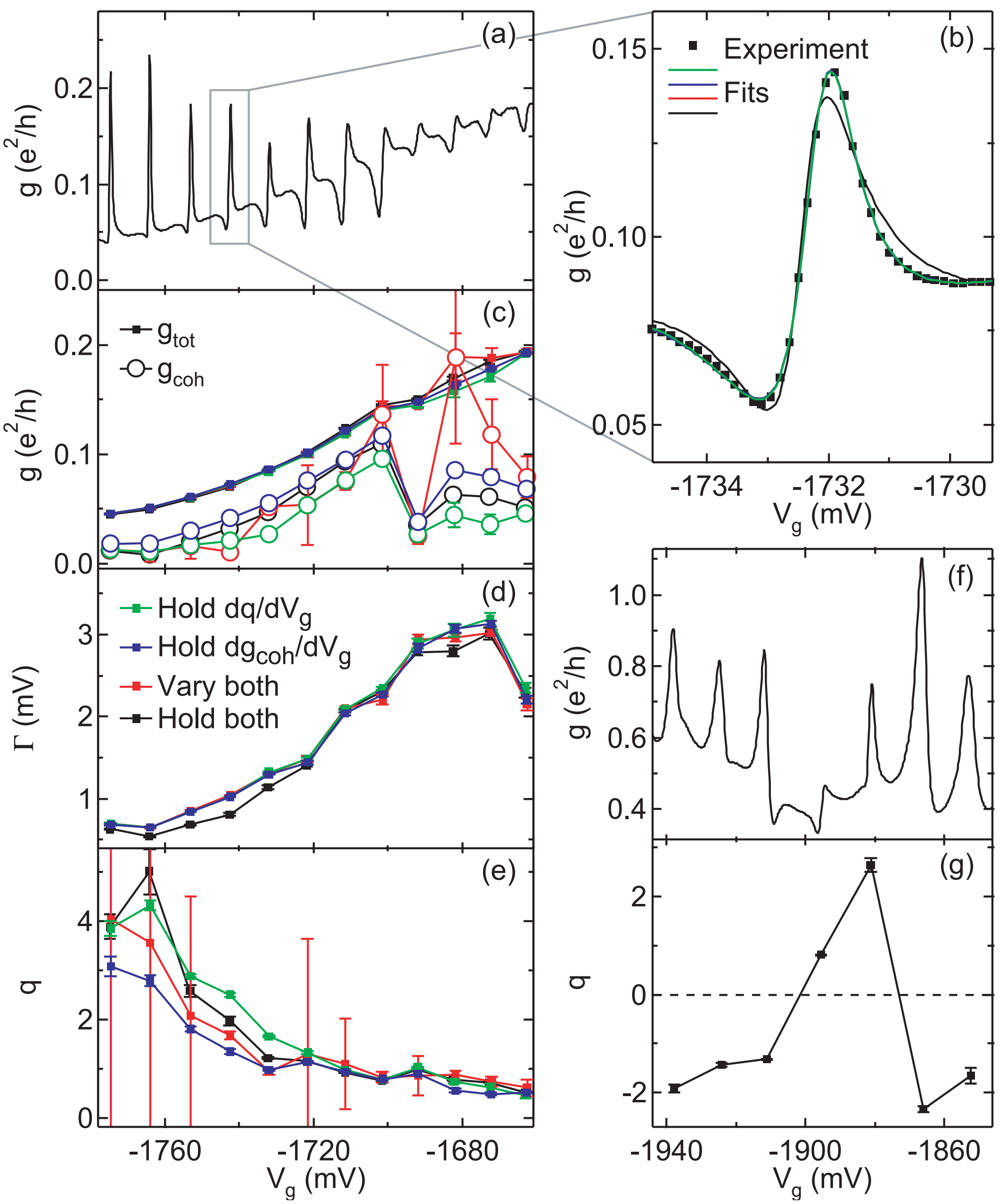

Figure 4.4: (a) Experimental data with twelve Fano resonances. In (b) we show one resonance and its four fits. Of the parameters dq/dV_g and dg_{coh}/dV_g, the fits fix at zero both (black), one (green and blue), or neither (red). All four fits are shown, but the latter three are indistinguishable. In (c)-(e) we plot, using the same colors to denote fitting method, the parameters g_{tot} and g_{coh}, Γ, and q, from the fits to (a). Panel (f) shows data exhibiting reversals of the sign of q, with extracted q values shown in (g).

channel which couple differently to the dot. A jump in g_{coh}/g_{tot} may reflect abrupt rearrangement of dot wave functions, changing its coupling to each channel mode while total coupling, measured by Γ, is nearly unchanged.

Second, changes to the sign of q are present but infrequent. An example is the data in Fig. 4.4(f) and (g), where q flips twice in the observed range. Previous observations of mesoscopic Fano resonance in transmission [62, 63, 64, 65], including measurements of a dot in an Aharonov-Bohm ring [79, 80] showed a constant sign of q, sparking intense debate on why no reversals were seen when simple theory predicts that consecutive peaks always change sign [78, 81, 82]. In the present geometry, however, as with recent work on Fano resonance in reflection [66], a constant sign is expected because the dot meets the channel in only one lead, so there is no freedom of relative sign between two matrix elements to reverse the phase. Why then are different signs of q observed here at all? One possibility is that the scattering phase in the channel changes by π, as if it too passed through a resonance [83]. This requires q to pass smoothly through zero at a maximum of g_{tot}, which is consistent with the observation that q is mostly positive in some regions and negative in others, but cannot explain the flips in Fig. 4.4(f). A more likely explanation for this data is that the source and drain leads couple to different areas in the dot, due to the spatial extent of the tunnel barrier. With appropriate nodes in several wave functions, the source and drain couplings have opposite signs and q reverses sign for several resonances, exactly as observed in Fig. 4.4(f). In short, both coherence jumps and Fano parameter flips can be explained by imperfect one-dimensionality of the channel and the tunnel barrier. In principle, these effects could be used to study wave function properties not accessible via transmission.

We thank A. A. Clerk, W. Hofstetter and B. I. Halperin for useful discussion and N. J. Craig for experimental contributions. This work was supported in part by the ARO under DAAD19-99-1-0215 and the Harvard NSF-NSEC (PHY-0117795). ACJ acknowledges support from the NSF Graduate Research Fellowship Program.

Chapter 5

Differential charge sensing and charge delocalization in a tunable double quantum dot

L. DiCarlo, H. J. Lynch, A. C. Johnson, L. I. Childress, K. Crockett, C. M. Marcus
Department of Physics, Harvard University, Cambridge, Massachusetts
M. P. Hanson, A. C. Gossard
Department of Materials, University of California, Santa Barbara, California

We report measurements of a tunable double quantum dot, operating in the quantum regime, with integrated local charge sensors. The spatial resolution of the sensors is sufficient to allow the charge distribution within the double dot system to be resolved at fixed total charge. We use this readout scheme to investigate charge delocalization as a function of temperature and strength of tunnel coupling, showing that local charge sensing allows an accurate determination of interdot tunnel coupling in the absence of transport.[1]

---

[1] This chapter is adapted from Ref. [84]

5.1 Introduction

Coupled semiconductor quantum dots have proved a fertile ground for exploring quantum states of electronic charge and spin. These “artifical molecules” are a scalable technology with possible applications in information processing. New kinds of classical computation may arise from quantum dots configured as single electron switches [74] or as building blocks for cellular automata [85]. Ultimately, coupled quantum dots may provide a quantum computing platform where the charge states and/or spins of electrons play a vital role [86]. Charge-state superpositions may be probed using tunnel-coupled quantum dots, which provide a tunable two-level system whose two key parameters, the bare detuning ϵ and tunnel coupling t between two electronic charge states [40], can be controlled electrically.

In this chapter, we investigate experimentally a quantum two-level system, realized as left/right charge states in a gate-defined GaAs double quantum dot, using local electrostatic sensing (see Fig. 5.1). In the absence of tunneling, the states of the two-level system are denoted $(M+1, N)$ and $(M, N+1)$, where the pair of integers refers to the number of electrons on the left and right dots. For these two states, the total electron number is fixed, with a single excess charge moving from one dot to the other as a function of gate voltages. When the dots are tunnel coupled, the excess charge becomes delocalized and the right/left states hybridize into symmetric and antisymmetric states.

Local charge sensing is accomplished using integrated quantum point contacts (QPCs) positioned at opposite sides of the double dot. We present a model for charge sensing in a tunnel-coupled two-level system, and find excellent agreement with experi-

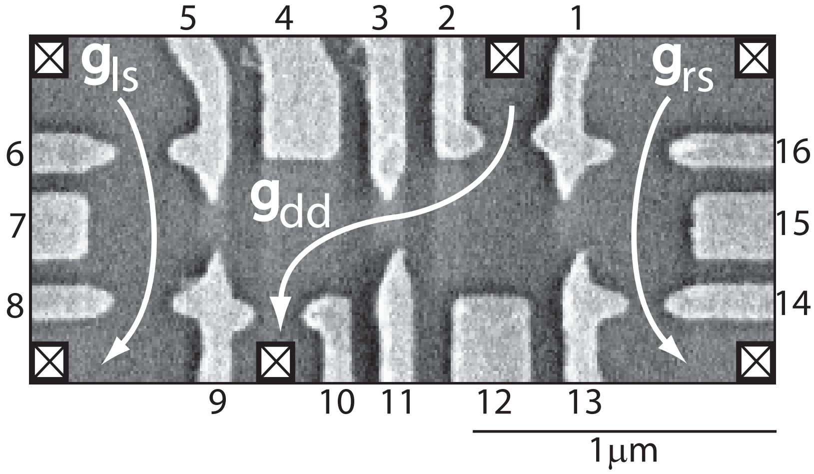

Figure 5.1: SEM micrograph of a device similar to the measured device, consisting of a double quantum dot with quantum point contact charge sensors formed by gates 8/9 (13/14) adjacent to the left (right) dot. Series conductance g_{dd} through the double dot was measured simultaneously with conductances g_{ls} and g_{rs} through the left and right sensors.

ment. The model allows the sensing signals to be calibrated using temperature dependence and measurements of various capacitances. For significant tunnel coupling, $0.5k_BT_e \lesssim t \ll \Delta$ (T_e is electron temperature, Δ is the single-particle level spacing of the individual dots), the tunnel coupling t can be extracted quantitatively from the charge sensing signal, providing an improved method for measuring tunneling in quantum dot two-level systems compared to transport methods [40].

Charge sensing using a QPC was first demonstrated in Ref. [71], and has been used previously to investigate charge delocalization in a single dot strongly coupled to a lead in the classical regime [73], and as a means of placing bounds on decoherence in an isolated double quantum dot [85]. The back-action of a QPC sensor, leading to phase decoherence, has been investigated experimentally [87] and theoretically [88]. Charge sensing with sufficient spatial resolution to detect charge distributions within a double dot has been demonstrated in a metallic system [72, 89]. However, in metallic systems the interdot tunnel coupling cannot be tuned, making the crossover to charge delocalization difficult to investigate. Recently, high-bandwidth charge sensing using a metallic single-electron transistor [90], allowing individual charging events to be counted, has been demonstrated [58]. Recent measurements of gate-defined few-electron GaAs double dots [91] have demonstrated dual-QPC charge sensing down to $N, M = 0, 1, 2...$, but did not focus on sensing at fixed electron number, or on charge delocalization. The present experiment uses larger dots, containing ~ 200 electrons each (though still with temperature less than level spacing, see below).

The device we investigate, a double quantum dot with adjacent charge sensors, is formed by sixteen electrostatic gates on the surface of a GaAs/$\mathrm{Al_{0.3}Ga_{0.7}As}$ heterostructure grown by molecular beam epitaxy (see Fig. 5.1). The two-dimensional electron gas layer, 100 nm below the surface, has an electron density of $2 \times 10^{11}\,\mathrm{cm}^{-2}$ and mobility $2 \times 10^{5}\,\mathrm{cm}^2/\mathrm{Vs}$. Gates 3/11 control the interdot tunnel coupling while gates 1/2 and 9/10 control coupling to electron reservoirs. In this measurement, the left and right sensors were QPCs defined by gates 8/9 and 13/14, respectively; gates 6, 7, 15, and 16 were not energized. Gaps between gates 5/9 and 1/13 were fully depleted, allowing only capacitive coupling between the double dot and the sensors.

Series conductance, g_{dd}, through the double dot was measured using standard lock-in techniques with a voltage bias of $5\,\mu\mathrm{V}$ at 87 Hz. Simultaneously, conductances through the left and right QPC sensors, g_{ls} and g_{rs}, were measured in a current bias configuration using separate lock-in amplifiers with $0.5\,\mathrm{nA}$ excitation at 137 and 187 Hz. Throughout the experiment, QPC sensor conductances were set to values in the 0.1 to 0.4 e^2/h range by adjusting the voltage on gates 8 and 14.

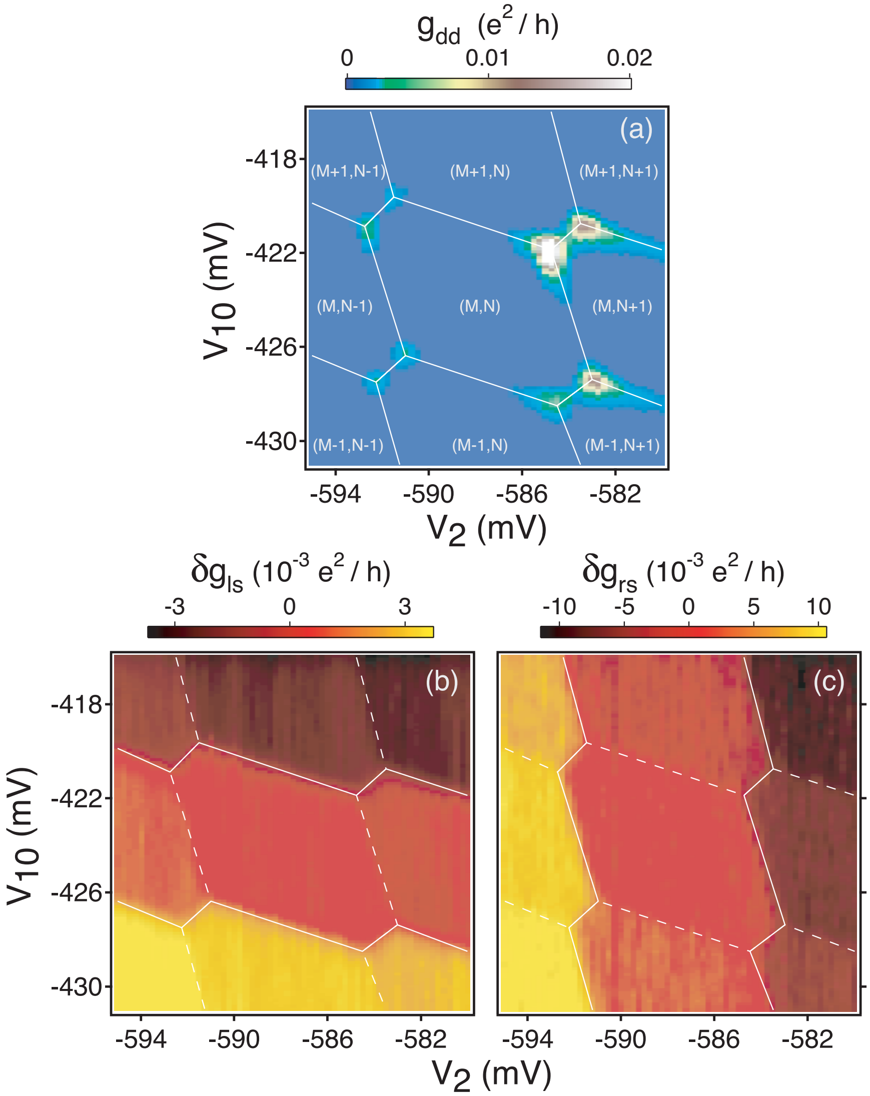

Figure 5.2: a) Double dot conductance, $g_{\rm dd}$, as a function of gate voltages V_2 and V_{10}. White lines indicate the honeycomb pattern. Within each honeycomb cell, electron number on each dot is well defined, with M(N) referring to electron number in the left (right) dot. b, c) Simultaneously measured sensing signals from left (b) and right (c) QPCs. $\delta g_{\rm ls}$ ($\delta g_{\rm rs}$) are QPC conductances after subtracting a best-fit plane. See text for details. The horizontal pattern in (b) and vertical pattern in (c) demonstrate that each sensor is predominantly sensitive to the charge on the dot it borders.

The device was cooled in a dilution refrigerator with base temperature $T \sim 30\,$mK. Electron temperature T_e at base was $\sim 100\,$mK, measured using Coulomb blockade peak widths with a single dot formed. Single-particle level spacing $\Delta \sim 80\,\mu$eV for the individual dots was also measured in a single-dot configuration using differential conductance measurements at finite drain-source bias. Single-dot charging energies, $E_C = e^2/C_o \sim 500\,\mu\text{eV}$ for both dots (giving dot capacitances $C_o \sim 320\,\text{aF}$), were extracted from the height in bias of Coulomb blockade diamonds [92].

5.2 Charge sensing honeycombs

Figure 5.2(a) shows g_{dd} as a function of gate voltages V_2 and V_{10}, exhibiting the familiar 'honeycomb' pattern of series conductance through tunnel-coupled quantum dots [93, 94, 95]. Conductance peaks at the honeycomb vertices, the so-called triple points, result from simultaneous alignment of energy levels in the two dots with the chemical potential of the leads. Although conductance can be finite along the honeycomb edges as a result of cotunneling, here it is suppressed by keeping the dots weakly coupled to the leads. Inside a honeycomb, electron number in each dot is well defined as a result of Coulomb blockade. Increasing V_{10} (V_2) at fixed V_2 (V_{10}) raises the electron number in the left (right) dot one by one.

Figures 5.2(b) and (c) show left and right QPC sensor signals measured simultaneously with g_{dd}. The sensor data plotted are $\delta g_{\text{ls(rs)}}$, the left (right) QPC conductances after subtracting a best-fit plane (fit to the central hexagon) to remove the background slope due to cross-coupling of the plunger gates (gates 2 and 10) to the QPCs. The left sensor shows conductance steps of size $\sim 3 \times 10^{-3}\, e^2/h$ along the (more horizontal) honeycomb edges where the electron number on the left dot changes by one (solid lines in Fig. 5.2(b)); the right sensor shows conductance steps of size $\sim 1 \times 10^{-2}\, e^2/h$ along the (more vertical) honeycomb edges where the electron number of the right dot changes by one (solid lines in Fig. 5.2(c)). Both detectors show a conductance step, one upward and the other downward, along the $\sim$ 45-degree diagonal segments connecting nearest triple points. It is along this shorter segment that the total electron number is fixed; crossing the line marks the transition from $(M+1, N)$ to $(M, N+1)$. Overall, we see that the transfer of one electron between one dot and the leads is detected principally by the sensor nearest to that dot, while the transfer of one electron between the dots is detected by both sensors, as an upward step in one and a downward step in the other, as expected.

5.3 Temperature and tunnel coupling

Focusing on interdot transitions at fixed total charge, i.e., transitions from $(M+1, N)$ to $(M, N+1)$, we present charge-sensing data taken along the "detuning" diagonal by controlling gates V_2 and V_{10}, shown as a red diagonal line between the triple points in Fig. 5.3(a). Raw data (no background subtracted) for the two sensors are shown in Fig. 5.3(b). The transfer of the excess charge from left dot to right dot causes a conductance step on both QPCs, clearly discernable from the background slope caused by coupling of gates 2 and 10 to the QPCs.

Also shown in Fig. 5.3(b) are fits to the raw sensor data based on a model of local sensing of an isolated two-level system in thermal equilibrium, which we now describe. Varying V_2 and V_{10} along the red diagonal changes the electrostatic energy difference, or bare detuning ϵ, between $(M+1, N)$ and $(M, N+1)$. The lever arm relating gate voltage to detuning is set by the slope of the swept diagonal and by several dot capacitances, and can be calibrated experimentally as described below. When the tunnel coupling t mixing these two states is small compared to the single-particle

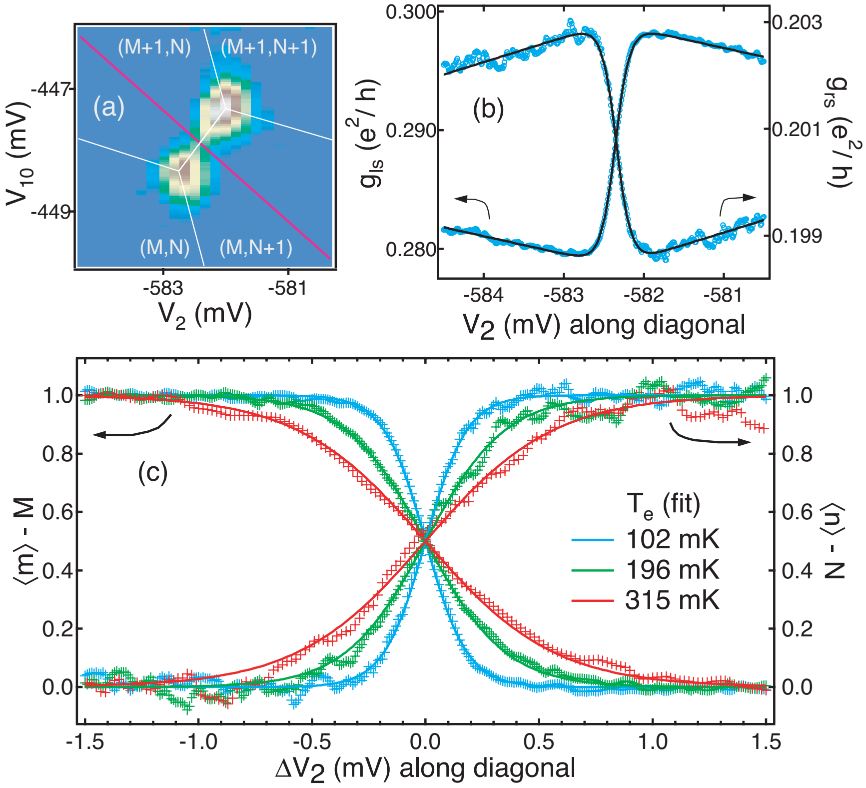

Figure 5.3: a) Double dot conductance $g_{\rm dd}$ as a function of gate voltages V_2 and V_{10} in the vicinity of a triple point. Same color scale as in Fig. 5.1(a). The detuning diagonal (red line) indicates the fixed-charge transition between $(M+1,N)$ and $(M,N+1)$. b) Left and right QPC conductance with no background subtraction (blue points), along the detuning diagonal, with fits to the two-level model, Eq. (2) (black curves). See text for fit details. c) Excess charge (in units of e) in the left and right dot, at $T = 30\,\mathrm{mK}$ (blue), $200\,\mathrm{mK}$ (green) and $315\,\mathrm{mK}$ (red). Corresponding values of T_e extracted from the fits (solid curves) are 102, 196 and 315 mK.

level spacings for the individual dots, we can consider a two-level system whose ground and excited states, separated by an energy $\Omega = \sqrt{\epsilon^2 + 4t^2}$, consist of superpositions of $(M+1,N)$ and $(M,N+1)$ [96]. The probability of finding the excess charge on the left dot while in the ground (excited) state is $\frac{1}{2}(1 \mp \epsilon/\Omega)$. The excited state is populated at finite temperature, with an average occupation $1/(1+\exp(-\Omega/k_B T_e))$. The average excess charge (in units of e) on the left and right dots is thus:

$$\left\{ \begin{array}{c} \langle m\rangle - M \\ \langle n\rangle - N \end{array} \right\} = \frac{1}{2}\left(1 \mp \frac{\epsilon}{\Omega}\tanh\left(\frac{\Omega}{2k_B T_e}\right)\right). \qquad (5.1)$$

Our model assumes that each sensor responds linearly to the average excess charge on each dot, but more sensitively to that on the nearest dot as demonstrated experimentally in Fig. 5.2. The resulting model for sensor conductance is:

$$g_{\mathrm{ls(rs)}} = g_{o\mathrm{l}(o\mathrm{r})} \pm \delta g_{\mathrm{l(r)}} \frac{\epsilon}{\Omega} \tanh\left(\frac{\Omega}{2k_B T_e}\right) + \frac{\partial g_{\mathrm{l(r)}}}{\partial \epsilon}\epsilon. \tag{5.2}$$

The first term on the right is the background conductance of the QPC, the second term represents the linear response to average excess charge, and the third represents direct coupling of the swept gates to the QPC. As shown in Fig. 5.3(b), our model gives very good fits to the data. For each trace (left and right sensors), fit parameters are $g_{o\mathrm{l}(o\mathrm{r})}$, $\delta g_{\mathrm{l(r)}}$, $\frac{\partial g_{\mathrm{l(r)}}}{\partial \epsilon}$, and T_e. In these data, the tunnel coupling is weak, and we may set $t = 0$.

Figure 5.3(c) shows the effect of increasing electron temperature on the transition width. Here, vertical axes show excess charge extracted from fits to QPC sensor conductance data. Sweeps along the red diagonal were taken at refrigerator temperatures of 30 mK (blue), 200 mK (green) and 315 mK (red). We use the 315 mK (red) data to extract the lever arm relating voltage along the red diagonal (see Fig. 5.3(a)) to detuning ϵ. At this temperature, electrons are well thermalized to the refrigerator, and thus $T_e \approx T$. The width of the sensing transition at this highest temperature lets us extract the lever arm, which we then use to estimate the electron temperature for the blue (green) data, getting $T_e = 102(196)$ mK.

We next investigate the dependence of the sensing transition on interdot tunneling in the regime of strong tunneling, $t \gtrsim k_B T_e$. Figure 5.4 shows the left QPC sensing signal, again in units of excess charge, along the detuning diagonal crossing a different pair of triple points, at base temperature and for various voltages on the coupling gate 11. For the weakest interdot tunneling shown ($V_{11} = -1096$ mV), the transition was thermally broadened, i.e., consistent with $t = 0$ in Eqs. 5.1 and 5.2, and did not become narrower when V_{11} was made more negative. On the other hand, when V_{11} was made less negative, the transition widened as the tunneling between dots increased. Taking $T_e = 102\,\mathrm{mK}$ for all data and calibrating voltage along the detuning diagonal by setting $t = 0$ for the $V_{11} = -1096$ mV trace allows tunnel couplings t to be extracted from fits to our model of the other tunnel-broadened traces. We find $t = 10\,\mu\mathrm{eV}$ (2.4 GHz) (green trace), $t = 16\,\mu\mathrm{eV}$ (3.9 GHz) (turquoise trace), and $t = 22\,\mu\mathrm{eV}$ (5.3 GHz) (purple trace). Again, fits to the two-level model are quite good, as seen in Fig. 5.4.

Finally, we compare tunnel coupling values extracted from charge sensing to values found using a transport-based method that takes advantage of the t dependence of the splitting of triple points (honeycomb vertices) [97, 40]. In the weak tunneling regime, $t \ll \Delta$, the splitting of triple points along the line separating isocharge regions $(M+1, N)$ and $(M, N+1)$ has two components in the plane of gate voltages, denoted here δV_{10} and δV_2. The lower and upper triple points are found where the lowest energy $M + N + 1$ state (the delocalized antisymmetric state) becomes degenerate with the charge states (M, N) and $(M+1, N+1)$, respectively. Using the electrostatic model in Ref. [40], we can show that $\delta V_{10(2)}$ are related to various dot capacitances and t by

$$\delta V_{10(2)} = \frac{|e|}{C_{g10(g2)}} \left(\frac{C_m}{C_o + C_m} + 2t \frac{C_o - C_m}{e^2} \right). \tag{5.3}$$

Here, $C_{g10(g2)}$ is the capacitance from gate 10 (2) to the left (right) dot, C_o is the self-capacitance of each dot, and C_m is the interdot mutual capacitance. All these capacitances must be known to allow extraction of t from $\delta V_{10(2)}$. Gate capacitances

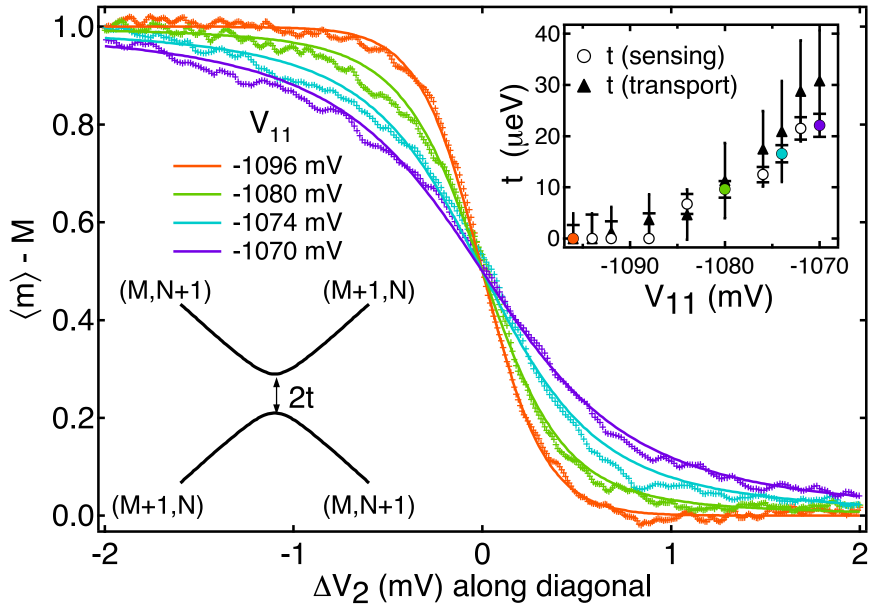

Figure 5.4: Excess charge on the left dot, extracted from left QPC conductance data, along a detuning diagonal (crossing different triple points from those in Fig. 5.3) at base temperature and several settings of the coupling gate 11. The temperature-broadened curve (red) widens as V_{11} is made less negative, increasing the tunnel coupling, t. See text for details of fits (solid curves). Top right inset: comparison of t values extracted from sensing (circles) and transport (triangles) measurements, as a function of V_{11}. Colored circles correspond to the transitions shown in the main graph. Lower left inset: Schematic energy diagram of the two-level system model, showing ground and excited states as a function of detuning ϵ, with splitting (anticrossing) of $2t$ at $\epsilon = 0$.

$C_{g10(g2)}$ are estimated from honeycomb periods along respective gate voltage axes, $\Delta V_{10(2)} \sim |e|/C_{g10(g2)} \sim 6.8\,\mathrm{mV}$. Self-capacitances C_o can be obtained from double dot transport measurements at finite bias [40]. However, lacking that data, we estimate C_o from single-dot measurements of Coulomb diamonds [92]. Mutual capacitance C_m is extracted from the dimensionless splitting $\delta V_{10(2)}/\Delta V_{10(2)} \sim \frac{C_m}{C_o+C_m} \sim 0.2$, measured at the lowest tunnel coupling setting.

Tunnel coupling values as a function of voltage on gate 11, extracted both from charge sensing and triple-point separation, are compared in the inset of Fig. 5.4. The two approaches are in good agreement, with the charge-sensing approach giving significantly smaller uncertainty for $t \gtrsim 0.5k_BT_e$. The two main sources of error in the sensing approach are uncertainty in the fits (dominant at low t) and uncertainty in the lever arm due to a conservative 10 percent uncertainty in T_e at base. Error bars in the transport method are set by the smearing and deformation of triple points as a result of finite interdot coupling and cotunneling. We note that besides being more sensitive, the charge-sensing method for measuring t works when the double dot is fully decoupled from its leads. Like the transport method, however, the sensing approach is valid for $t \ll \Delta$ (this condition may not be amply satisfied for the highest values of V_{11}).

In conclusion, we have demonstrated differential charge sensing in a double quantum dot using paired quantum point contact charge sensors. States $(M+1, N)$ and $(M, N+1)$, with fixed total charge, are readily resolved by the sensors, and serve as a two-level system with a splitting of left/right states controlled by gate-defined tunneling. A model of local charge sensing of a thermally occupied two-level system agrees well with the data. Finally, the width of the $(M+1,N) \rightarrow (M,N+1)$ transition measured with this sensing technique can be used to extract the tunnel coupling with high accuracy in the range $0.5k_BT_e \lesssim t \ll \Delta$.

We thank M. D. Lukin, B. I. Halperin and W. van der Wiel for discussions, and N. J. Craig for experimental assistance. We acknowledge support by the ARO under DAAD19-02-1-0070, DARPA under the QuIST program, the NSF under DMR-0072777 and the Harvard NSEC, Lucent Technologies (HJL), and the Hertz Foundation (LIC).

Chapter 6

Charge sensing of excited states in an isolated double quantum dot

A. C. Johnson, C. M. Marcus
Department of Physics, Harvard University, Cambridge, Massachusetts 02138
M. P. Hanson, A. C. Gossard
Department of Materials, University of California, Santa Barbara, California 93106

Pulsed electrostatic gating combined with capacitive charge sensing is used to perform excited state spectroscopy of an electrically isolated double-quantum-dot system. The tunneling rate of a single charge moving between the two dots is affected by the alignment of quantized energy levels; measured tunneling probabilities thereby reveal spectral features. Two pulse sequences are investigated, one of which, termed latched detection, allows measurement of a single tunneling event without repetition. Both provide excited-state spectroscopy without electrical contact to the double-dot system.[1]

---

[1] This chapter is adapted from Ref. [98]

6.1 Introduction

Electrically controllable discrete quantum states found in quantum dot systems are efficient laboratories for the study of quantum coherence [99, 100], as well as a potential basis for quantum computation [101, 102]. Measuring the spectrum and dynamics of quantum dots requires coupling to a macroscopic measurement apparatus, which in turn may act to reduce coherence [103, 87, 104, 105, 106]. Excited state spectroscopy of single [107, 108] and double [109, 110, 40] quantum dots has typically been performed using nonlinear transport, requiring tunnel coupling of the device to electron reservoirs [40]. This coupling perturbs the quantum states and may increase decoherence and heat the device, particularly at the large biases needed for spectroscopy far from the Fermi surface.

An alternative approach that we investigate in this chapter is to use capacitive charge sensing [71, 72, 73, 91, 84] combined with pulsed gate voltages that provide an excitation window [111]. Charge sensing has recently been used to probe excited-state spectra in a few-electron quantum dot coupled to one reservoir [112]. We investigate pulse/sense spectroscopy in an electrically isolated double quantum dot, where a single charge, moving between the two dots, is used to probe excited states. Local charge sensing by a quantum point contact (QPC) near one of the dots provides readout.

The pulse/sense method operates as follows: A reset pulse on two gates simultaneously opens the coupling between the dots and tilts the potential, putting the excess charge on a selected dot. When the pulse is removed, each dot separately is in its ground state, but the double dot system is out of equilibrium. The excess charge is given a finite time to tunnel to the other dot (the probe time). The probability of tunneling depends sensitively on the alignment of ground and excited state levels in the two dots. Whether or not the charge tunnels during the probe time is detected by a QPC sensor.

Two gate sequences are investigated. In the first, a short reset pulse is followed by a relatively long probe interval during which a low tunneling rate gives a moderate total probability for tunneling. By cycling the reset/probe steps, the QPC measures the average charge configuration, dominated by the probe step. This allows fine energy resolution, as the probe process is insensitive to both thermal effects and experimental difficulties associated with short pulses. The second sequence uses two pulses: the first resets the system; the second allows weak tunneling between dots. The second pulse is followed by an arbitrarily long interval (microseconds to hours, in principle) with the interdot barrier closed, so that each dot is completely isolated, with fixed charge. This sequence we term latched detection, because the measurement occurs after the double dot is latched into a final state, separating in time the charge dynamics and the measurement. If needed, the measurement could be turned off during the probe pulse, though here we make the measurement time much longer than the probe time and measure weakly, so that the total back-action of the measurement on the system during the probe pulse is negligible. While here we use latched detection only for excited-state spectroscopy, we emphasize that its usefulness is much more general.

The device (Fig. 6.1(a)), defined by e-beam patterned Cr-Au depletion gates on a GaAs/ AlGaAs heterostructure grown by MBE, comprises two tunnel-coupled quantum dots of lithographic area 0.25 $\mu\mathrm{m}^2$ each and two independent charge-sensing channels, one beside each central dot. The two-dimensional electron gas lies 100 nm below the surface, with bulk density 2×10^{11} cm^{-2} and mobility $2{\times}10^5$ cm^2/Vs. Each

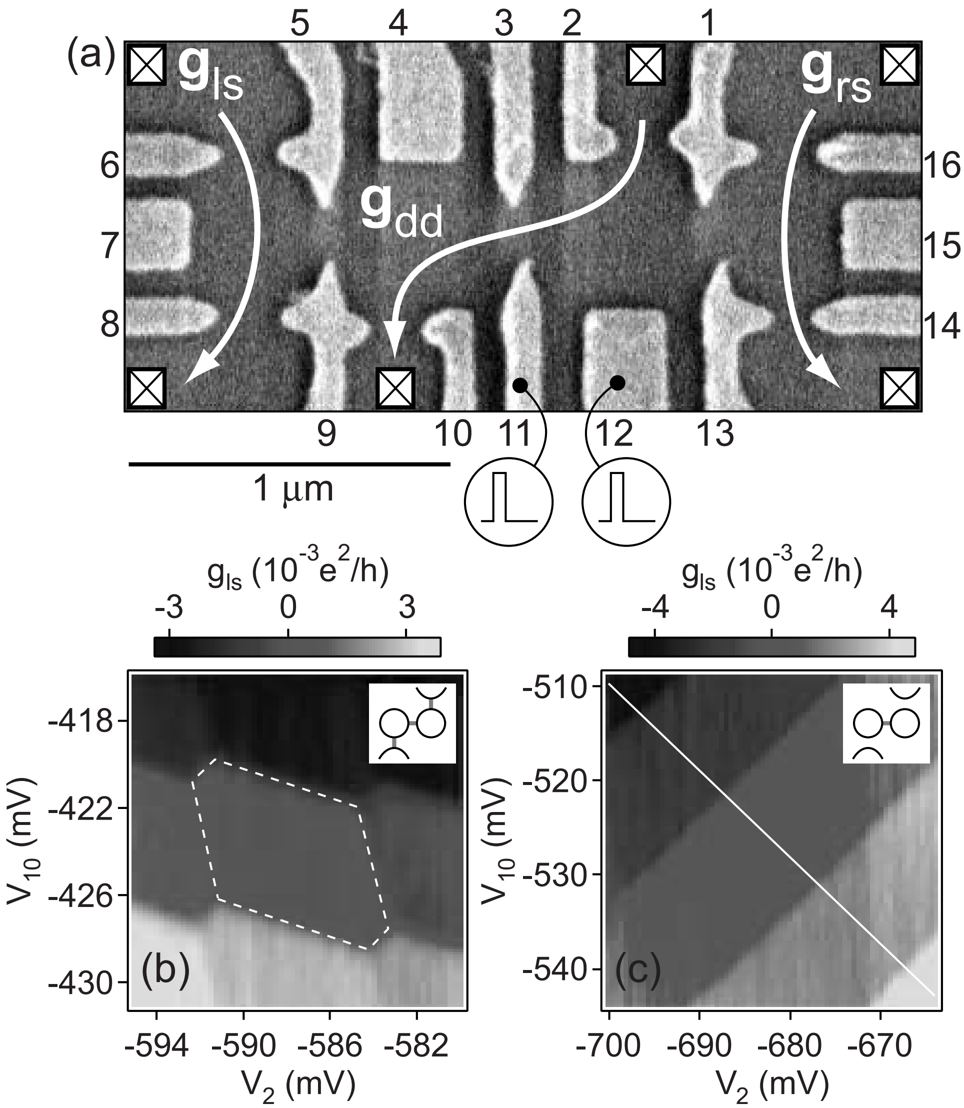

Figure 6.1: (a) Scanning electron micrograph of a device identical in design to the one measured, consisting of a double quantum dot with a charge sensor on either side. High-bandwidth coaxial lines are attached to gates 11 and 12, dc lines to the other gates. (b) Left sensor signal as a function of gate voltages V_2 and V_{10} reveals hexagonal charge stability regions (one outlined with dashed lines) when the double dot is tunnel-coupled to leads. (c) Sensor signal with the double dot isolated from the leads. Only interdot transitions remain. In all pulse/sense experiments presented, the double dot is isolated (as in c) and V_2 and V_{10} are swept along a diagonal crossing these transitions (solid white line). A plane is subtracted in (b) and (c) to compensate direct coupling of gates 2 and 10 to the sensor.

dot contains ~150 electrons and has a single-particle level spacing $\Delta \sim 100\mu$eV (estimated from effective device area) and charging energy $E_c \sim$ 600–700 μeV. Left and right sensor conductances g_{ls} and g_{rs} were measured using lock-in amplifiers with 2 nA current biases at 137 and 187 Hz; double-dot conductance g_{dd} was measured using a third lock-in amplifier with a 5 μV voltage bias at 87 Hz, although during pulse/sense measurement the double dot was fully isolated and the g_{dd} and g_{rs} circuits grounded. The charge sensors were configured as QPCs by grounding gates 6, 7, 15, and 16, and were isolated from the double dot by strongly depleting gates 5, 9, 13, and 1. Measurements were carried out in a dilution refrigerator with electron temperature ~100 mK.

6.2 Tunnel-coupled and isolated double dots

Figure 6.1(b) shows the left sensor signal as a function of gate voltages V_2 and V_{10} with the device tunnel-coupled to both leads. Here and in subsequent plots, a plane has been subtracted to level the central plateau to compensate for capacitive coupling between the gates and the sensor. In this regime, a honeycomb pattern characteristic of double-dot transport [40] is seen as a set of hexagonal plateaus in the left sensor conductance, with horizontally oriented steps of $\sim 3 \times 10^{-3}\ e^2/h$ corresponding to changes in the number of electrons in the left dot, controlled by V_{10}, and smaller vertically oriented steps marking changes in the right dot, controlled by V_2. Steps at the short upper left and lower right segments of each hexagon reflect movement of an electron from one dot to the other, with total number fixed. Here, an increase in g_{ls} marks an electron moving away from the left sensor, or an increase in the number of electrons in the right dot.

Transport through the double dot, g_{dd}, occurs only at the honeycomb vertices [84]. As tunneling to the leads is reduced by making V_2 and V_{10} more negative, the honeycomb sensing pattern persists after gdd has become immeasurably small, but the landscape changes dramatically as in Fig. 6.1(c) when the tunneling time between the double dot and the leads diverges. Here, steps follow diagonal lines of constant energy difference between the dots because only transitions from one dot to the other are allowed.

6.3 Single-pulse technique

Pulse/sense measurements were carried out in this isolated configuration, with the energy difference between the dots controlled by simultaneously varying V_2 and V_{10} along diagonals (shown, for example, by the white line in Fig. 6.1(c)), and the interdot barrier controlled by gate voltage V_3. Fast control of the same two parameters was achieved using two synchronized Agilent 33250 arbitrary waveform generators, with rise times of $\sim$ 5 ns, connected to gates 11 and 12 via semirigid coaxial lines and low-temperature bias tees. To compensate a slight cross coupling of gates 11 and 12, the pulse generators produced linear combinations of pulses, denoted V_B (affecting the barrier, mainly V_{11}) and V_E (affecting the energy difference, mainly V_{12}).

The single-pulse/probe sequence is shown schematically in the inset of Fig. 6.2. Square pulses of length $t_{reset} = 100$ ns are applied every 20 μs, with $V_B = 100$ mV opening the tunnel barrier while the pulse energy shift V_E is varied. The double dot relaxes to its overall ground state during the reset pulse if t_{reset} is much longer than the elastic and inelastic tunneling times τ_{el} and τ_{in} while the barrier is pulsed open, and also longer than the energy relaxation time within the dots. For the next 19.9 μs, the barrier is nearly closed, such that $\tau_{el} < t_{probe} < \tau_{in}$, and the energy levels are

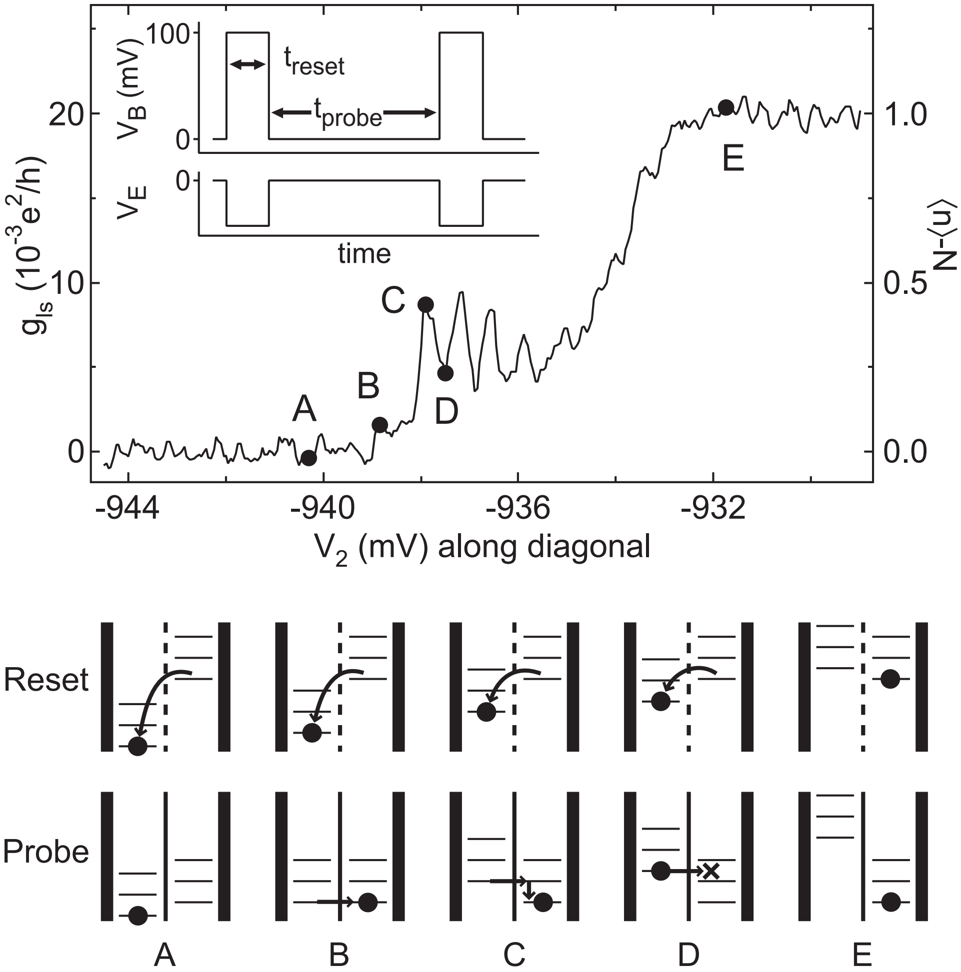

Figure 6.2: Single-pulse technique. Time-averaged conductance of the left sensor as a function of V_2 along diagonal (see Fig. 6.1(c)) with pulses applied. Inset: Pulses on gates 11 and 12 (parameterized by V_B and V_E, controlling interdot barrier and relative energy, see text), followed by a long interval of weak tunneling. A linear fit to the left plateau is subtracted. Right axis shows the average right-dot occupation $\langle n\rangle - N$. Points A–E mark features used to infer the excited state spectrum, with schematic interpretations shown below the graph.

returned to their values before the pulse. If elastic tunneling is allowed, the electron will likely tunnel and then have ample time to relax to its ground state. Without elastic tunneling, the electron will likely remain where the reset pulse put it.

Figure 6.2 shows the sensing signal during a simultaneous (diagonal, see Fig. 6.1(c)) sweep of V_2 and V_{10}, with five points (A to E) labeling key features. The data were taken with V_E negative, so that the pulse tilts the ground state toward the left dot. At point A, the energy difference in both the reset and probe states favors the excess charge occupying the left dot, and a flat sensing signal corresponding to a time-averaged right-dot occupation $\langle n \rangle = N$ is observed. At the opposite extreme (E), the energy difference in both cases favors the right dot, giving another a flat signal, $\langle n \rangle = N + 1$. At point B, the ground states of the dots are degenerate in the probe state (except for small tunnel splitting). This degeneracy appears in the data as a small peak in right-dot occupation, often barely visible above the noise, presumably because tunneling in this case is reversible; the electron does not relax once it enters the right dot, so it is free to return to the left. There is a much larger peak at C. Here either an excited state in the right dot aligns with the ground state in the left or a hole excited state in the left dot aligns with the ground state in the right. After tunneling occurs the system can relax, trapping the electron in the right dot. Finally at D, no excited states exist to match the initial configuration and allow elastic tunneling, so there is a dip in the right-dot occupation.

Figure 6.3(a) shows the sensing signal measured throughout the pulse/dc-energy-shift plane, with prominent diagonal steps marking the ground state transitions during the pulse, and fine bands extending horizontally from each step reflecting excited state transitions available during the probe time. Figure 6.3(b) presents the same data differentiated with respect to V_2 and smoothed along both axes. Here, steps in the raw signal appear as positive ridges, and excited state peaks become bipolar. The comparison with single-dot transport spectroscopy is clear: the pulse opens an energy window, and as the window expands, more excited states become accessible and emerge from the ground state feature. Features on the left (negative V_E) mark

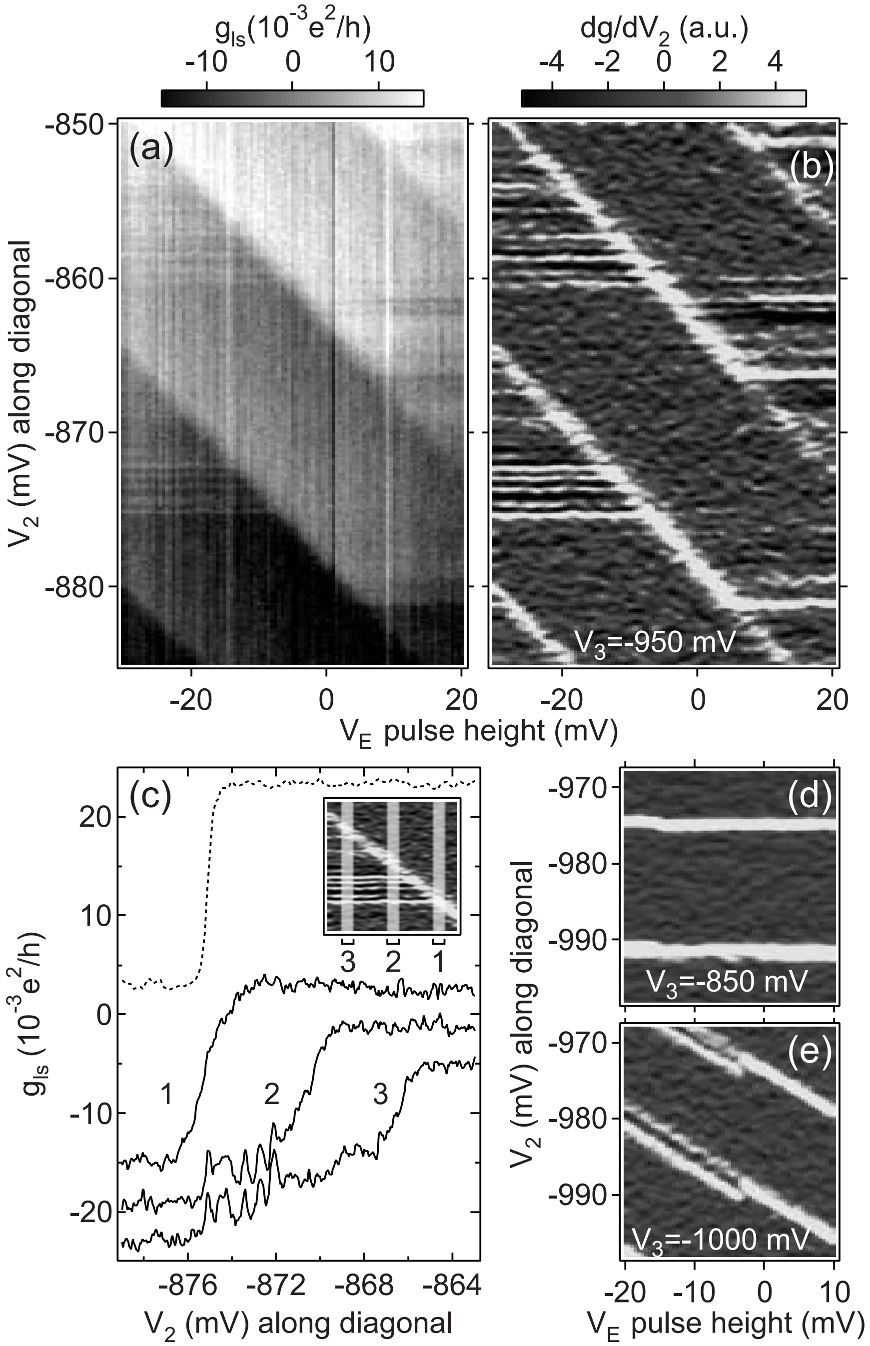

Figure 6.3: (a) Left sensor conductance, and (b) its smoothed derivative with respect to V_2, as functions of V_2 and V_E. Horizontal excited state lines emerge from a diagonal ground state feature as the energy window V_E is increased. Vertical stripes in (a) result from sensor drift. (c) Slices of conductance (as in Fig. 6.2) as a function of V_2, averaged over different V_E ranges (see inset), offset vertically for clarity. Dashed curve is measured with pulses off. (d, e) Sensor conductance derivative as in (b) measured with the tunnel barrier either more open (d) or more closed (e) such that the probe or the reset configuration, respectively, dominates. Color scales in (d) and (e) are the same as in (b).

electron excited states of the right dot or hole excited states of the left; features on the right mark electron excited states of the left dot or hole excited states of the right.

Figure 6.3(c) shows slices of sensor conductance from Fig. 6.3(a) at three different V_E pulse heights, illustrating the expansion of the energy window while the positions of the emerging excited states remain fixed. The dashed curve shows the transition measured with no pulses applied. From its smooth, narrow shape, and its consistency from transition to transition, we conclude that its width is dominated by temperature broadening [84]. We associate this with a temperature of $\sim$100 mK, assuming the electron temperature in the dot is not significantly different in the tunneling regime, where it was previously calibrated [84]. This gives a lever arm $\delta V_2/\delta E = (10.5 \pm 1)/e$ relating changes in V_2 (along a diagonal with V_{10}) to changes in the energy of levels in the left dot relative to the right. The spacing between ground-state transitions gives the sum of the two charging energies, and assuming they are equal we find $E_c = 700 \pm 70 \mu\text{eV}$. The measured excited-state gate-voltage spacing of ~ 0.75 mV gives an excited level spacing of ~ 70 μeV, comparable to the $\Delta \sim 100\mu$eV estimated from dot area. The slightly lower measured value may reflect sensitivity to both electron and hole excited states, giving overlapping spectra. As the energy window is increased, excited-state-to-excited-state transitions become available, further complicating the observed spectra. This may explain the blurring at $V_2 > 872$ mV in curve 3.

Figure 6.3(c) shows that ground-state transitions for the pulse curves (solid) are clearly broader than for the no-pulse curve (dashed). Broadening beyond temperature is presumably due to both averaging traces with different V_E and effects of overshoot and settling of the pulse. However, as the probe step is long and insensitive to pulse properties, the excited state peaks are not similarly broadened. In principle, the excited state peaks are also immune to thermal broadening, their widths limited only by intrinsic decay rates, although all peaks shown here exhibit full widths at half maximum of at least 3.5 kT (0.3 mV), possibly due to gate noise.

Figures 6.3(d) and (e) repeat Fig. 6.3(b) with different values of gate voltage V_3, illustrating the effects of opening or closing the tunnel barrier beyond the regime of excited-state spectroscopy. Changing V_3 affects the interdot barrier both during and after the pulse, but the system is most sensitive to the tunnel rate during the probe time. Increasing tunneling by making V_3 less negative by 100 mV (Fig. 6.3(d)) yields single, horizontal features, as if no pulse were applied at all. This implies that $\tau_{in} \ll t_{probe}$ so the system quickly finds its ground state during the probe time regardless of relative energy levels, making the pulse irrelevant to a time-averaged measurement. Reducing tunneling by making V_3 more negative by 50 mV (Fig. 6.3(e)) results in diagonal features, indicating that dynamics during the pulse dominate behavior. In the right half of this plot there is a single transition, implying that the system finds its ground state while the pulse is on, then the barrier is closed such that $\tau_{el}, \tau_{in} \gg t_{probe}$ and no further tunneling is permitted. On the left there are two diagonal features, implying that an excited state is populated at the start of the reset pulse. This effect is not understood at present, nor is it specific to the too-closed-barrier regime; it is occasionally seen along with the understood horizontal excited state features.

6.4 Latched detection

We now turn to the second pulse/sense method described above, latched detection, using two pulses on each gate as shown in Fig. 6.4(a). Figure 6.4(b) shows the

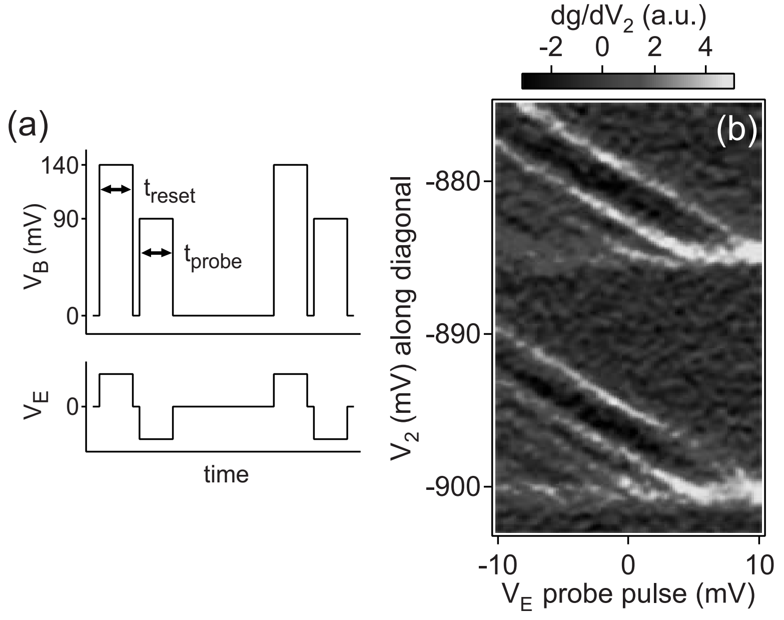

Figure 6.4: (a) Two-pulse technique, shown schematically, including a reset and a probe pulse, followed by a long measurement time when no tunneling is allowed. (b) Conductance derivative with respect to V_2, shows excited states appearing now as diagonal lines.

derivative of the sensor signal measured in this configuration as a function of V_2 and the V_E probe pulse height, using $t_{reset} = t_{probe} = 20$ ns, $V_B^{reset} = 140$ mV and $V_B^{probe} = 90$ mV. Here we vary the probe properties rather than the reset properties as in Fig. 6.3, so excited states appear diagonally and the reset ground state is horizontal. Excited states measured this way are not immune to pulse properties, and as a result, the data in Fig. 6.4 are blurred relative to Fig. 6.3. This diminished resolution is not fundamental, and can be reduced with more accurate pulse shaping.

We thank M. J. Biercuk and A. Yacoby for useful discussions and K. Crockett for experimental contributions. This work was supported in part by DARPA QuIST, Harvard NSF-NSEC, and iQuest at UCSB.

Chapter 7

Singlet-triplet spin blockade and charge sensing in a few-electron double quantum dot

A. C. Johnson, J. R. Petta, C. M. Marcus
Department of Physics, Harvard University, Cambridge, Massachusetts 02138
M. P. Hanson, A. C. Gossard
Department of Materials, University of California, Santa Barbara, California 93106

Singlet-triplet spin blockade in a few-electron lateral double quantum dot is investigated using simultaneous transport and charge-sensing measurements. Transport from the (1,1) to the (0,2) electron occupancy states is strongly suppressed relative to the opposite bias [(0,2) to (1,1)]. At large bias, spin blockade ceases as the (0,2) triplet state enters the transport window, giving a direct measure of exchange splitting of the (0,2) state as a function of magnetic field. A simple model for current and steady-state charge distribution in spin-blockade conditions is developed and found to be in excellent agreement with experiment. Three other transitions [(1,1) to (2,0), (1,3) to (2,2), and (1,3) to (0,4)] exhibit spin blockade while other nearby transitions and opposite bias configurations do not, consistent with simple even-odd shell filling.[1]

---

[1] This chapter is adapted from Ref. [113]

7.1 Introduction

Great progress has been made in engineering solid-state systems that exhibit quantum effects, providing new tools for probing fundamental problems in many-body physics as well as new device technologies. In semiconductor quantum dots, small numbers of confined electrons can be manipulated using electrostatic gates with surprising ease [49, 55, 114, 115]. For the case of two electrons in the dot (quantum dot "helium"), Pauli exclusion and exchange induce a splitting between the spin singlet and triplet states that can be controlled by gates and magnetic fields [92, 116]. In double dots, a consequence of this splitting is current rectification, in which transitions from the (1,1) to the (0,2) state (ordered pairs indicate electron occupancy in each dot) is blockaded, while the opposite bias case, involving transitions from (0,2) to (1,1) proceeds freely. Rectification is a direct consequence of spin selection rules [117].

Spin blockade of this type can be understood by considering positive and negative bias transport in a double dot containing one electron in the right dot, as indicated in Figs. 7.1(b) and (c). An electron of any spin can enter the left dot, making either a (1,1) singlet or triplet, these states being nearly degenerate for weak interdot tunneling [118]. In contrast, the right dot can accept an electron only to make a (0,2) singlet. At positive bias (Fig. 7.1(b)) current can flow: an electron enters the right dot to make a (0,2) singlet, tunnels to the (1,1) singlet, and escapes. At negative bias (Fig. 7.1(c)), an electron can enter the left dot and form a (1,1) triplet state. A transition from the (1,1) triplet to the (0,2) singlet is forbidden by conservation of spin and transport is blocked.

In this chapter we report a detailed investigation of spin blockade through a lateral

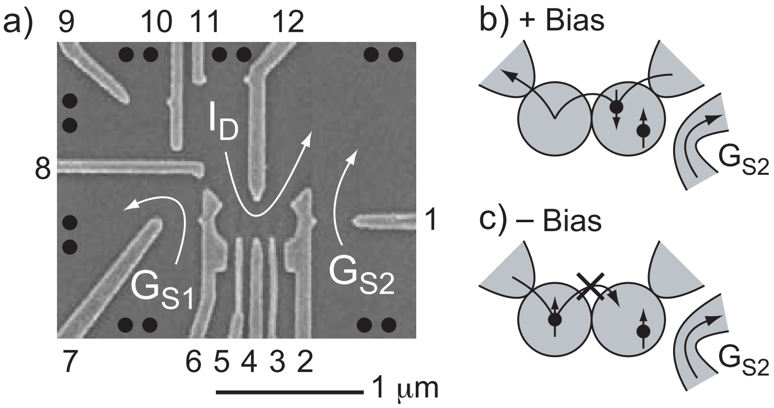

Figure 7.1: (a) Electron micrograph of a device identical in design to the one measured. Gates 2–6 and 12 define the double dot, 1 and 7 form QPC charge sensors, 8 separates the left QPC and double dot current paths, and 9–11 are unused. Black spots denote ohmic contacts. The origin of spin blockade, when the left dot has 0–1 electrons and the right dot 1–2 electrons, is illustrated in (b) and (c). Opposite spins represent a singlet, same spins a triplet. The left dot accepts any spin but the right can only form a spin singlet, blocking negative bias current once the wrong spin occupies the left dot. A charge sensor (G_{S2}) also registers the blockade, as a second electron is sometimes in the right dot at positive bias, but not at negative bias.

few-electron double-dot system, measured using both transport and charge sensing by a nearby quantum point contact (QPC) to detect the charge arrangement during blockade [71, 84]. We observe that transmission through double-dot states containing two electrons is strongly rectified, while transmission of the first electron is symmetric in bias. Negative-bias blockade is truncated when the (0,2) triplet state enters the bias window, allowing the magnetic field dependence of the singlet-triplet splitting to be measured from both transport and charge sensing. Simple rate-equation models for transport and charge distributions reproduce key features in both types of data, and allow relative tunnel rates to be extracted. Finally, other charge transitions are investigated, up to the second electron in the left dot and the fourth in the right dot. The presence or absence of spin blockade is shown to be consistent with even-odd shell filling.

Spin blockade of transport, arising from a variety of mechanisms, has been investigated previously in quantum dot systems [115, 119, 120, 121, 122, 123, 124, 54, 125]; the mechanism responsible for the present spin blockade was investigated in vertical structures in Ref. [117]. The lateral, gate-defined structure we investigate has some advantages over vertical structures by allowing independent tuning of all tunnel barriers so that sequential tunneling with arbitrary dot occupations can be explored. QPC charge sensors provide additional information, including the average charge distribution when transport is absent in the spin blockade regime.

The sample, shown in Fig. 7.1(a), is fabricated on a GaAs/AlGaAs heterostructure with two-dimensional electron gas (density 2×10^{11} cm^{-2}, mobility 2×10^{5} cm^2/Vs) 100 nm below the wafer surface, patterned with Ti/Au top gates. Gates 2–6 and 12 define a double quantum dot in which each dot can be tuned from zero to several electrons [126]. Gates 1 and 7 define QPCs whose conductance is most sensitive to the charge on the right and left dots respectively. Gate 8 isolates the current path of the double dot from the left QPC, while the double dot and right QPC share a common ground. Gates 9–11 are not energized. Current through the double dot (I_D) is measured in response to a dc voltage on the left reservoir. A small ac excitation (6 μV at 27 Hz) allows lock-in measurement of differential conductance. Conductances of QPC charge sensors ($G_{S1,2}$) are measured simultaneously with separate lock-in amplifiers (1 nA current bias at 93 and 207 Hz). Base electron temperature is $T_e \sim 135$ mK, measured from Coulomb blockade diamonds. Two devices were measured and showed qualitatively similar behavior; data from one device are presented.

7.2 Spin blockade at (1,1)-(0,2)

Figure 7.2 shows I_D at ±0.5 mV bias as a function of gate voltages V_2 and V_6, which primarily control the energy levels in the right and left dots. Figures 7.2(a) and (c) were measured near the conductance resonance of the first electron, with (m, n) indicating the charge states surrounding the resonance. At positive bias, finite current is measured within two overlapping triangles in gate voltage space, satisfying the inequalities $\mu_R \geq \epsilon_R \geq \epsilon_L \geq \mu_L$ or $\mu_R \geq \epsilon_R + E_m \geq \epsilon_L + E_m \geq \mu_L$. Here $\mu_{L,R}$ are the chemical potentials of the leads, $\epsilon_{L,R}$ are the energies to add an electron to the ground state of either dot, and the mutual charging energy E_m is the extra energy to add an electron to one dot with the other dot occupied [40]. The first set of inequalities defines the lower, or electron triangle, where, starting at (0,0), an electron hops through the dots from one lead to the other. The second inequalities define the upper, or hole triangle, where, starting at (1,1), a hole hops across the dots. Electron and hole processes involve the same three tunneling events, only their order changes. Schematics at the top of Fig. 7.2 depict the energy level alignments at the vertices of the electron triangle in Fig. 7.2(a). Within the triangles, current depends primarily on the detuning $\Delta = \epsilon_L - \epsilon_R$ of one-electron states, with a maximum current at $\Delta = 0$, demonstrating that interdot tunneling is strongest at low energy loss, consistent with previous studies of inelastic tunneling in double dots [127]. At negative bias (Fig. 7.2(c)) the triangles flip and current changes sign, but otherwise these data mimic the positive bias case (Fig. 7.2(a)).

The corresponding data with another electron added to the right dot is shown in Figs. 7.2)(b) and (d). At positive bias, the data qualitatively resemble the one-

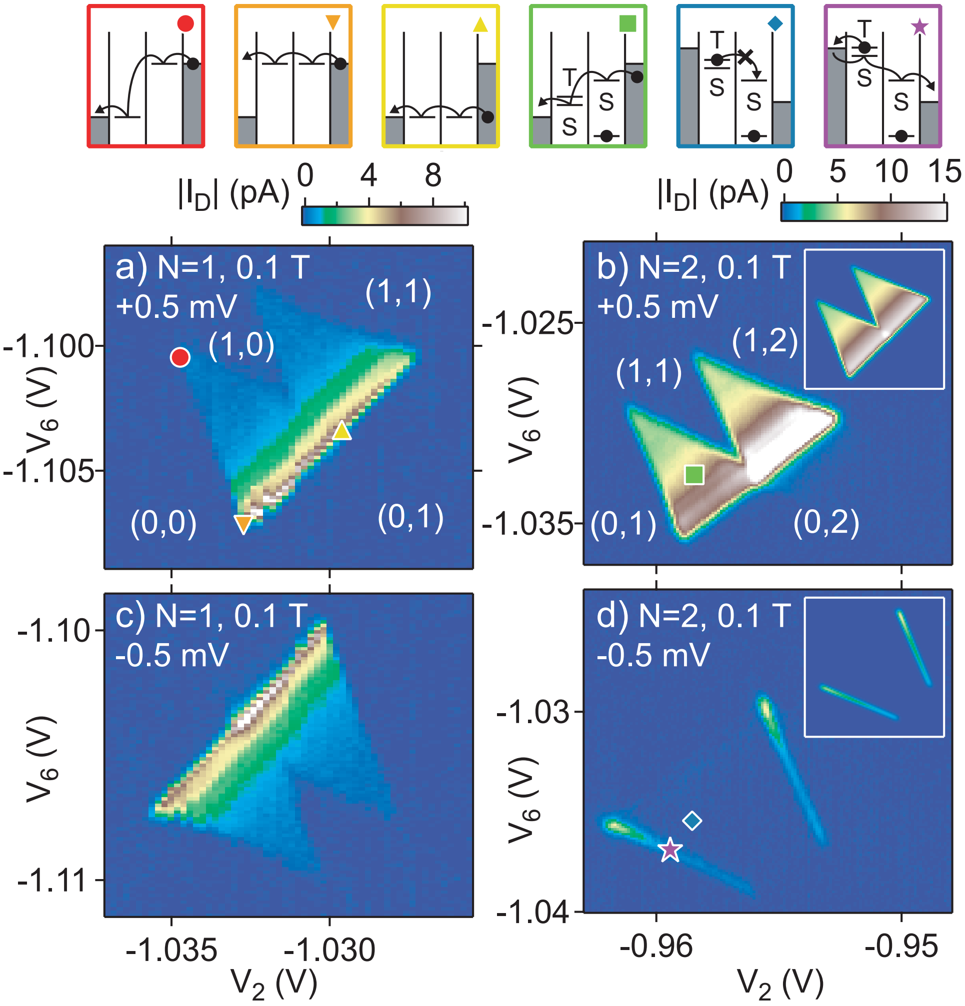

Figure 7.2: (a) Magnitude of current I_D as a function of V_2 and V_6 across the (1,0) to (0,1) transition at 0.5 mV bias. Ordered pairs (m, n) denote electrons on the left (m) and right (n) dots, with N total electrons present during interdot tunneling. The red ($\bigcirc$), orange ($\bigtriangledown$), and yellow ($\bigtriangleup$) diagrams illustrate the level alignments bounding a bias triangle. The same configuration at -0.5 mV bias, (c), shows almost perfect symmetry. (b) and (d) show the equivalent data at the (1,1) to (0,2) transition. Current flows freely at positive bias, as depicted in the green diagram ($\Box$). Negative bias current is suppressed by spin blockade (blue diagram, $\diamond$) except on the lower (purple diagram, $\star$) and upper edges. Insets to (b) and (d) show results of a rate equation model which captures most features of the data (see text).

electron case. However, at negative bias the current is nearly zero, except along the outermost edges of the electron and hole triangles. Referring to the diagrams above Fig. 7.2, at positive bias, current proceeds freely from right to left through singlet states (green square). At negative bias, an electron enters the left dot into either the

(1,1) singlet or triplet. If it enters the (1,1) singlet, it may continue through the (0,2) singlet. However, once an electron enters the (1,1) triplet, it can neither continue to the right (into the (0,2) singlet) nor go back into the left lead because it is below the Fermi level and the hole it left quickly diffuses away. Thereafter, negative-bias transport requires a spin flip or a second-order spin exchange process with one of the leads. Insofar as these processes are relatively slow, transport in this direction is blockaded.

Along the outer edge of the lower (electron) triangle, where transport is observed in the negative-bias direction (Fig. 7.2(d), purple star), an electron trapped in the (1,1) triplet state is within the thermal window of the left lead and will occasionally exchange with another electron possibly loading the (1,1) singlet, which can the move to the right, through the (0,2) singlet, and contribute to current. An analogous mechanism in the hole channel allows negative-bias current along the upper edge of the hole triangle: with transitions from (1,1) to (1,2) within the thermal window, the blockade created by an occupied (1,1) triplet can be lifted by adding an electron, making a (1,2) state, then removing it, possibly leaving a (1,1) singlet that can contribute to current.

A simple rate-equation model allows the spin-blockade picture to be quantitatively checked against transport data, and also indicates where charge resides in the double dot, which can be compared to charge sensing data. The model takes two degenerate levels in the left dot, representing the (1,1) singlet and triplet states, coupled equally to a thermally broadened left reservoir (i.e., ignoring the extra degeneracy of the triplet[2]) and a single level of the right dot, representing the (0,2) singlet (assuming

---

[2] Including the full triplet degeneracy would decrease the calculated current along

the (0,2) triplet is energetically inaccessible) coupled to the right reservoir. The singlet levels are coupled by thermally activated inelastic tunneling, with the shape of the $\Delta = 0$ peak inserted to match the positive-bias current data. Temperature, mutual charging energy, and the gate capacitances are determined from measurements. Calculated current is shown in the insets to Figs. 7.2(b) and (d). The model resembles the experimental data, with two minor exceptions: At positive bias, measured current is higher in the hole triangle than the electron triangle, implying that the dot-lead tunnel barriers are, in this case, more transparent with the other dot occupied. Also, the small but finite blockade current is absent in the model, as expected since the model contains only first-order, spin-conserving processes.

Figure 7.3 shows the charge sensor data G_{S2} versus V_2 and V_6, acquired simultaneously with each panel in Fig. 7.2. A plane is subtracted from each data set to remove direct coupling between the gates and the QPC, leaving only the effect of the average dot occupations. Away from the bias triangles we see plateaus for each stable charge state, which are used to calibrate the response. In Figs. 7.3(a) and (c), QPC conductance jumps $\Delta G_R = 0.016\ e^2/h$ due to a charge in the right dot, and $\Delta G_R = 0.008\ e^2/h$ due to the left. These values vary between data sets, but this QPC is always about twice as sensitive to the closer dot.

Within each bias triangle, the sensing signal varies with the fraction of time an electron spends in each charge state. Consider Fig. 7.3(a), the one-electron positive bias

---

the blockaded triangle edges by roughly a factor of two. While we cannot quantitatively fit to the model given the asymmetry between the electron and hole triangles, the current amplitude with no degeneracy does seem correct to better than a factor of two. One possibility is that the singlet and $m_s = 0$ triplet may be mixed by nuclei (see [128] and Ch. 8), making the effective degeneracies of blockaded and unblockaded states equal.

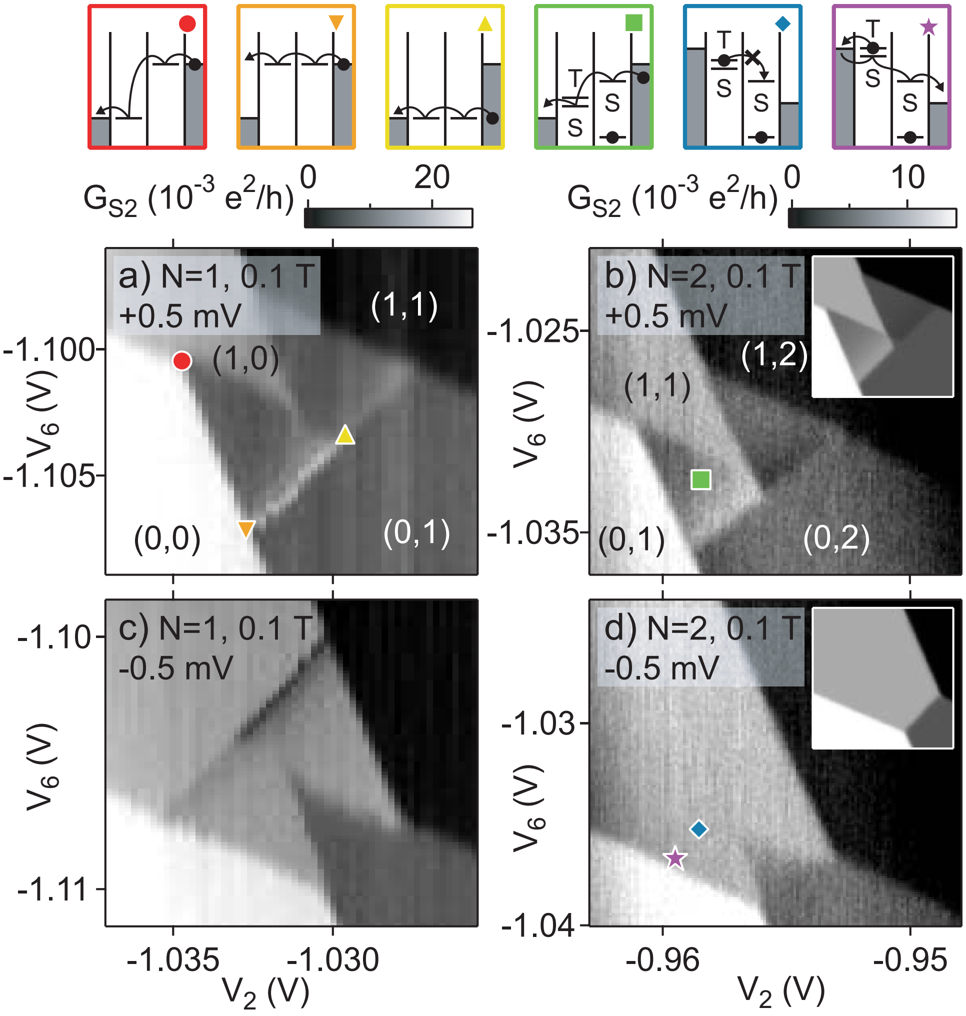

Figure 7.3: Charge sensor signal G_{S2} measured simultaneously with each panel of Fig. 7.2. A plane is subtracted from each panel to remove direct gate-QPC coupling. The first electron, (a) and (c), again shows bias symmetry while the second, (b) and (d), is missing features at negative bias. The model used in Fig. 7.2 also reproduces the charge sensor data, as shown in the insets to (b) and (d), with slight disagreement due to second-order processes (see text).

data. As with transport through the dot, charge sensing is primarily dependent on detuning, Δ. For small interdot tunneling, the system rests mainly in (0,1), thus at large detuning the sensing signal matches the (0,1) plateau. In the electron triangle, as detuning decreases and interdot tunneling increases, the system spends more time in (1,0) and (0,0). Both increase the right QPC sensor conductance. In the hole triangle, the system accesses (1,0) and (1,1), which respectively increase and decrease the right sensing signal.

Assuming the same tunnel rates to the leads in the electron and hole triangles, lead asymmetry can be quantified by comparing the rate-equation model to the sensor signal in the two triangles. At the one-electron transition, the charge sensor signal can be written as a deviation from the (0,1) plateau, $\Delta G_S = \Delta G_R(p_{10}+p_{00}) - \Delta G_L(p_{10}+p_{11})$, where p_{mn} is the occupation probability of charge state (m, n). At positive bias, current flows only leftward through each barrier, thus conservation of current gives $p^e_{01}\Gamma_D = p^e_{10}\Gamma_L = p^e_{00}\Gamma_R$ in the electron triangle and $p^h_{01}\Gamma_D = p^h_{10}\Gamma_R = p^h_{11}\Gamma_L$ in the hole triangle, where Γ_D, Γ_L, and Γ_R are the interdot, left, and right barrier tunnel rates. As each set of three probabilities sums to unity, we can calculate each individually (e.g. $p^e_{00} = [1 + (\Gamma_R/\Gamma_L) + (\Gamma_R/\Gamma_D)]^{-1}$). We define a quantity α as the ratio of ΔG_S in the hole triangle to ΔG_S at the same detuning (thus the same Γ_D) in the electron triangle, which gives $\alpha = [(S-1)p^h_{10} - p^h_{11}]/[(S-1)p^e_{10} + Sp^e_{00}]$, where S is the QPC sensitivity ratio $\Delta G_R/\Delta G_L$. Inserting the expressions for the occupation probabilities in terms of tunnel rates, we find

$$\alpha = \frac{S - 1 - \Gamma_R/\Gamma_L}{(S-1)\Gamma_R/\Gamma_L + S}. \tag{7.1}$$

This expression is independent of Γ_D (and therefore independent of detuning), implying that the lineshape of ΔG_S as a function of detuning is the same in each triangle, up to an overall positive or negative factor α. This can be seen qualitatively in Figs. 7.3(a) and (c), with equally narrow ΔG_S peaks of the same sign in each triangle, and in Fig. 7.3(b), with equally broad ΔG_S peaks of opposite sign in each triangle. Linear cuts through these data sets confirm that the lineshapes are identical to within measurement errors. Rearranging Eq. 7.1 gives the lead asymmetry

$$\Gamma_R/\Gamma_L = \frac{S - 1 - S\alpha}{1 + (S-1)\alpha}. \tag{7.2}$$

From Fig. 7.3(a), we measure $\alpha = 0.35 \pm 0.05$, giving $\Gamma_R/\Gamma_L = 0.23 \pm 0.08$. Similar analysis at negative bias (Fig. 7.3(c)) yields $\Gamma_R/\Gamma_L = 0.35 \pm 0.10$. In the positive bias two-electron case (Fig. 7.3(b)), the hole triangle shows a negative sensor change, indicating that the left barrier is more opaque than the right. It is not possible to further quantify this ratio, as we know from Fig. 7.2(b) that tunnel rates in the two triangles differ. In this case, unambiguously determining the individual tunnel rates would be possible only by using both charge sensors simultaneously.

In the spin blockade region (Fig. 7.3(d), near the blue diamond), no sensor variation is seen, confirming that the system is trapped in (1,1). By including lead asymmetry and QPC sensitivities, the rate-equation model used for the insets to Figs. 7.2(b) and (d) yields charge sensor signals as well. These are shown in the insets to Figs. 7.3(b) and (d), and again the agreement is good. The one discrepancy is between the two triangles at negative bias. The model shows a thermally broadened transition from (1,1) to (0,2) at a detuning equal to the bias. This is equivalent to strictly zero interdot tunneling, in which case the system has a ground state and occupations mimic a zero-bias stability diagram. However, between the bias triangles the only mechanism for equilibration is a second order process of each dot exchanging an electron with its lead. This is slow enough to occur on par with the second order and spin-flip processes noted above which circumvent the blockade, so the sensor shows a mixture of (1,1) and (0,2).

Figure 7.4 illustrates the features that arise at dc bias larger than Δ_{ST}, the (0,2) singlet-triplet energy splitting. Panels (a)–(d) show I_D and G_{S2} versus voltages V_2 and V_6 at ±1 mV bias and a perpendicular magnetic field $B_\perp = 0.9$ T. At negative bias, spin blockade is lifted when the (1,1) triplet is raised above the (0,2) triplet (pink +), so in Figs. 7.4(c) and (d), current turns on and steady-state populations shift where $\Delta > \Delta_{ST}$, with Δ the detuning of the (1,1) ground state with respect to the (0,2) ground state, given by the distance from the upper left side of the triangles. At positive bias, current increases (Fig. 7.4(a)) and populations shift (Fig. 7.4(b)) when the Fermi level in the right lead accesses the (0,2) triplet (black ×), which occurs at a fixed distance from the lower left side of each triangle. Thus, Δ_{ST} can be measured using either current or charge sensing and either sign of bias, with the energy scale calibrated by equating the triangle size to the dc bias [40]. Current and sensing give consistent values of Δ_{ST}, but different splittings are measured at different biases and gate voltages, presumably reflecting real changes in Δ_{ST} as these parameters are tuned. The two measurements in Fig. 7.4(a) give 480 and 660 μeV. The negative bias measurement gives $\sim 520 \pm 50$ μeV in Fig. 7.4(c). The fact that positive bias measurements differ more than negative bias measurements implies that occupation of the left dot has a strong effect on the right dot levels.

Increasing $B_{\perp}$ reduces Δ_{ST}, as seen in previous experiments [92, 116, 117, 129, 130, 131, 111, 132, 133] and theoretical work [133, 134, 135, 136], bringing the negative bias current threshold closer to the zero-detuning (upper left) edge. Figure 7.4(e) shows negative bias current at $B_{\perp} = 1.7$ T, where a dramatic decrease in Δ_{ST} is seen compared to Fig. 7.4(c). Figure 7.4(f) shows Δ_{ST} as a function of $B_{\perp}$ based on negative-bias data at different gate voltage settings. For the open squares, no voltages besides V_2 and V_6 were changed during the field sweep. The tunnel barriers closed with increasing field, obscuring the measurement above 2.5 T, before the splitting reached zero. The sweep yielding the filled circles and panels (a)–(e), started from different gate voltages and gave V_4 and V_{12} corrections quadratic in field to keep the

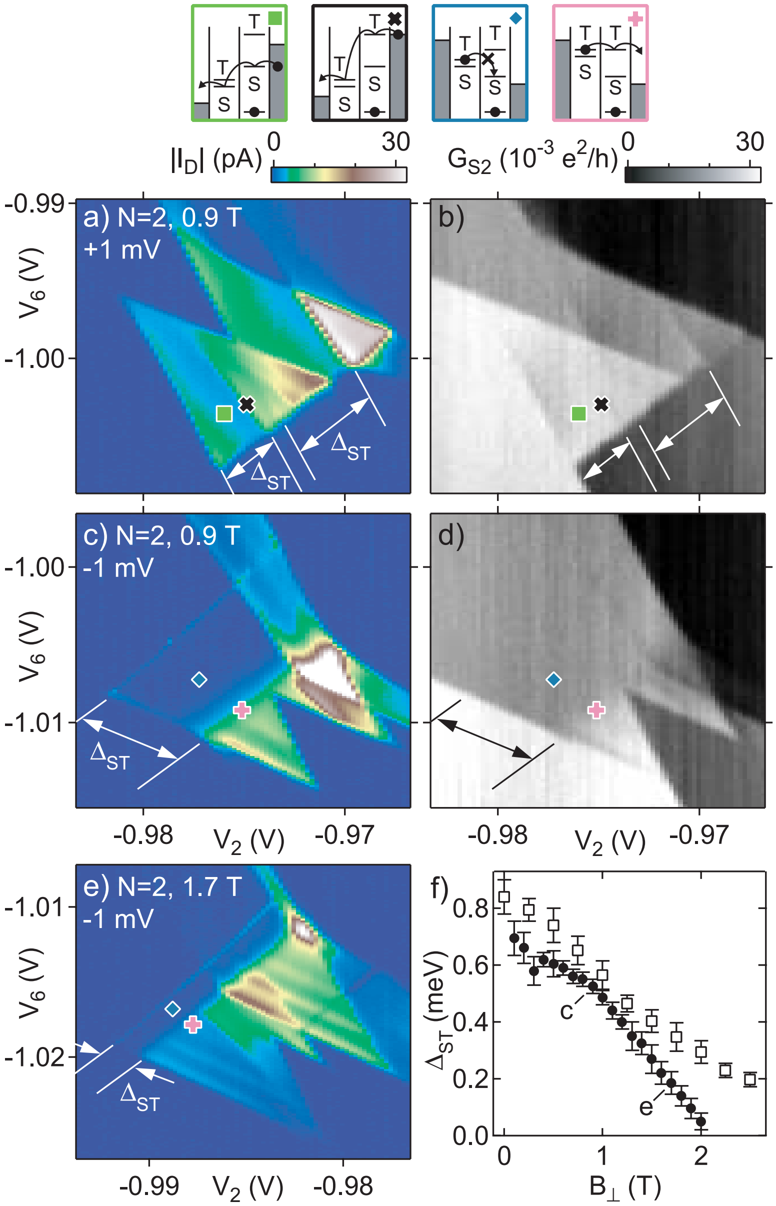

Figure 7.4: Measurements of the singlet-triplet splitting, Δ_{ST}. At +1 mV bias, I_D (a) and G_{S2} (b) as a function of V_2 and V_6 at the (1,1) to (0,2) transition show new features where triplet current is allowed (black diagram, ×) rather than just singlet current (green, □). At negative bias, I_D (c) turns on and G_{S2} (d) changes when triplet states break the spin blockade (pink + vs. blue ◇). Several Δ_{ST} values are measured from (a)–(d), which we attribute to gate voltage dependence of Δ_{ST}. As $B_\perp$ increases, (e), Δ_{ST} decreases rapidly. The dependence of Δ_{ST} on $B_\perp$ is shown in (f), with the solid and open series both taken at negative bias from different gate voltage configurations.

barriers roughly constant. Δ_{ST} dropped until at 2.1 T no splitting was observed. A split feature was hinted at in the 2.5 T positive bias data, implying that the triplet had become the ground state, but again the signal vanished as field increased. Zeeman splitting, though it would be a small effect regardless, is entirely absent at negative bias as interdot transitions connect states with equal Zeeman energy.

7.3 Spin blockade at other charge transitions

All of the results so far have concerned two charge transitions, corresponding to adding the first electron to the left dot and either the first or second to the right. Figure 7.5 extends these measurements through the second charge transition in the left dot, after which the tunnel barriers could no longer be balanced, and through the fourth transition in the right dot, after which complications were observed in the honeycomb pattern, indicative of a triple dot beginning to form. These measurements allow us to comment on the robustness of singlet-triplet spin blockade with more particles and more complicated energy levels.

The simplest situation we can imagine for our double dot is no symmetry to the potential in either dot. In this case there is no orbital level degeneracy, and we expect even-odd filling, with each odd electron inhabiting a new level and each even electron pairing with the preceding odd electron to form a spin singlet. Figure 7.5(b) illustrates where we would expect to see spin blockade within this model. When the total number of electrons during interdot tunneling is odd, current flows from one spin doublet to another. Current flows freely in either bias direction, indicated by a dark double-headed arrow. For even total electron number, one charge state (in which

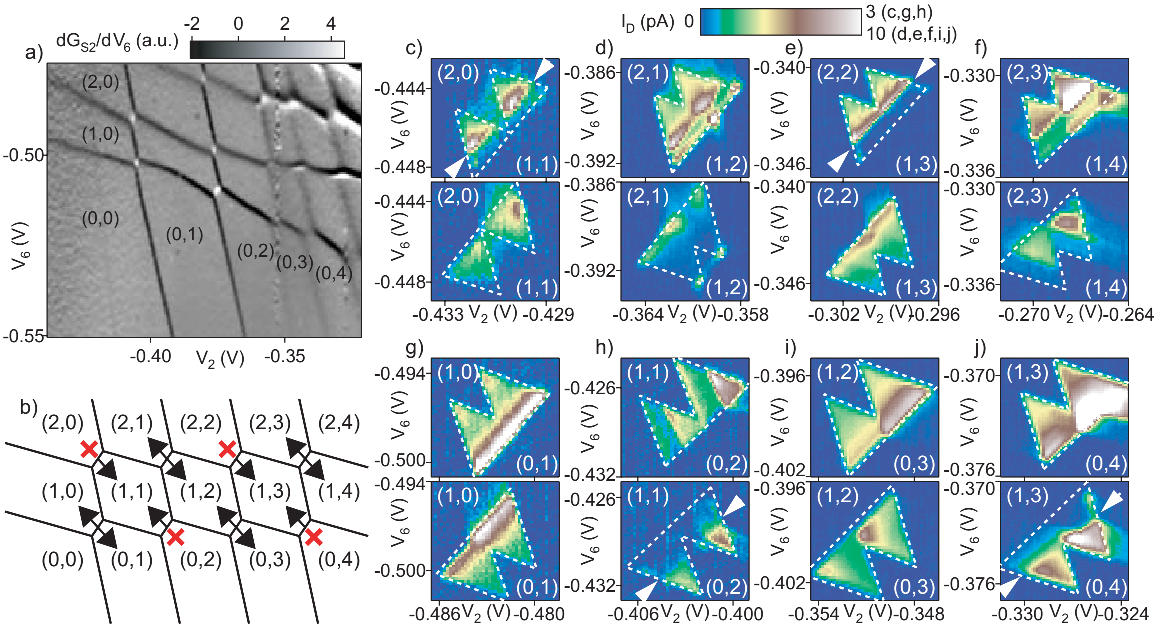

Figure 7.5: Spin blockade at other charge transitions. (a) G_{S2} over a wide range of V_2 and V_6, differentiated numerically in V_6, maps out the first several charges added to each dot. Bipolar transitions at higher occupation numbers (upper right corner) result from large dot conductance affecting the charge sensor measurement due to the shared drain reservoir. (b) Locations of current suppression due to spin blockade in an even-odd level filling model. I_D vs. V_2 and V_6 at each of these eight transitions for positive (upper half) and negative (lower half) bias are shown in panels (c)–(j). Dashed white outlines are guides to the eye indicating the full bias triangle size. One outline in each panel is drawn by hand, then rotated 180° and overlaid on the opposite bias data to ensure equal size. White arrows indicate the boundaries of observed spin blockade regions.

each dot contains an even number of electrons) has a singlet ground state, whereas the other charge state (two odd occupations) may form a triplet or a singlet. Current in one bias direction, indicated by the red X, is therefore expected to be blockaded at interdot bias less than the energy gap to the first triplet state in the doubly even charge state. Current at the opposite bias flows uninhibited from one singlet state to the other.

Figure 7.5(a) shows a large scale plot of the charge sensor signal versus V_2 and V_6, with zero bias across the dot, differentiated with respect to V_6. Sharp features in this type of plot mark changes in the occupation of each dot and allow us to determine the absolute occupation at each point. These data were taken after applying positive voltages to the gates while recooling the same device used in Figs. 7.2–7.4, which shifted all charge transitions to less negative gate voltages and gave smaller singlet-triplet splittings. Gates 3, 4, 5, and 12 are adjusted at each charge transition to balance the interdot and dot-lead tunnel barriers. Figures 7.5(c)–(j) show current through the dot versus V_2 and V_6 in a field of 100 mT for all charge transitions involving the first or second electron in the left dot and the first through fourth in the right dot—the same transitions shown in Fig. 7.5(b). The top half of each panel is measured at positive bias (250 μV in (c), 500 μV elsewhere) while the bottom half is measured at an equal negative bias. Spin blockade is seen in each configuration predicted in Fig. 7.5(b) and nowhere else. At the (1,1) to (0,2) transition (Fig. 7.5(h)), we measure negative-bias spin blockade as in Figs. 7.2–7.4, this time with (0,2) singlet-triplet splitting $\Delta_{ST} \sim 300$ μeV. This smaller splitting, compared to the 600–900 μeV seen previously, indicates either a larger and shallower or more elongated potential profile compared with the previous cooldown, such that the energy cost of triplet occupation is decreased. At the nominally symmetric (1,1) to (2,0) transition (Fig. 7.5(c)) spin blockade is observed in positive bias, and yields a (2,0) singlet-triplet splitting which is smaller still, roughly 80 μeV.

The (1,3) to (2,2) transition, Fig. 7.5(e), again shows positive bias blockade, with a splitting of $\sim$140 μeV. In this case there are two different (2,2) triplet states capable of breaking the spin blockade. One is a triplet in the left dot and singlet in the right, in which the conduction cycle looks identical to (1,1) to (2,0) but with a static singlet pair added to the right dot. The second possibility is a singlet in the left dot and triplet in the right. Here a singlet correlation between two of the right-dot electrons is transferred to the left dot, just as in (1,2) to (2,1) transport, while the triplet correlation between one electron in each dot is transferred to the two electrons in the right dot. Because of these two available processes, the measured Δ_{ST} is expected to represent the minimum of the left-dot and right-dot singlet-triplet splittings.

A singlet ground state is expected in any situation where one quantum level contains a spin pair and is not degenerate with any unfilled levels. A two-electron dot, therefore, will always have a singlet ground state because the first quantum level, with no nodes, never has orbital degeneracy [118]. For this reason, it is clear that the spin blockade we observe in Figs. 7.5(c), (e), and (h) all originate from singlet ground states and triplet excited states. In nearly symmetric potentials, however, a four-electron dot can show a triplet ground state due to Hunds rule. This has been observed in a vertical quantum dot through a detailed analysis of the spin transitions seen out to high perpendicular magnetic field [49], and in a lateral quantum dot comparable in size to one of our dots by the absence of Zeeman splitting in a large parallel field [137].

The spin blockade observed at the (1,3) to (0,4) transition, Fig. 7.5(j), with $\Delta_{ST} \sim$ 200–300 μeV, does not necessarily indicate that the singlet is the ground state of the (0,4) configuration, just that singlet or triplet has an energy lower than the other by the observed splitting. Moreover, dependence of the splitting on perpendicular magnetic field up to a few tesla, as measured in Fig. 7.4(f), would not distinguish between singlet and triplet ground states. If the ground state were a singlet, it would gain more energy due to lateral confinement than the more extended triplet state, as was the case with the two-electron dot, and therefore the singlet-triplet gap would close with field. A triplet ground state would indicate near-degeneracy of two orbital levels, so that adding a perpendicular field would favor singlet occupation of the level with lower orbital angular momentum, and again the gap would close with field.

In the present experiment, a parallel field was unavailable and, as described above, high perpendicular field has too strong an effect on tunnel barriers to allow measurements of other spin transitions, thus a direct comparison with the methods used in earlier works is not possible. However, one piece of evidence implies that our four-electron dot, in contrast to the previous measurements, has a singlet ground state. Consider the (1,4) to (2,3) transition, Fig. 7.5(f). The (2,3) configuration consists of two singlet pairs and one free spin, making an overall spin-1/2 state. The same is true of (1,4) if the four-electron dot is a singlet, which would not give any current suppression, as observed. However, if the four-electron dot were a triplet, the overall (1,4) state could have a spin of 1/2 or 3/2, leading to a suppression of current from (1,4) to (2,3), which might be termed doublet-quadruplet spin blockade. Instead, as much current is seen in Fig. 7.5(f) at positive bias as at negative bias, leading us to conclude that this four-electron dot is a spin singlet. While this is the reverse of the conclusion drawn in the two previous experiments, it is perhaps not surprising given the triple-dot behavior seen at higher right dot occupations. This behavior indicates an elongated potential in the right dot, possibly with a double minimum even while it acts as a single dot.

We acknowledge useful discussions with Jacob Taylor and Amir Yacoby. This work was supported by the ARO, the DARPA QuIST program, the NSF including the Harvard NSEC, and iQuest at UCSB.

Chapter 8

Triplet-singlet spin relaxation via nuclei in a double quantum dot

A. C. Johnson[a], J. R. Petta[a], J. M. Taylor[a], A. Yacoby[a,b], M. D. Lukin[a],
C. M. Marcus[a], M. P. Hanson[c], A. C. Gossard[c]
[a]*Department of Physics, Harvard University, Cambridge, Massachusetts*
[b]*Department of Condensed Matter Physics, Weizmann Institute, Rehovot, Israel*
[c]*Department of Materials, University of California, Santa Barbara, California*

The spin of a confined electron, when oriented in some direction, will lose memory of that orientation after some time. Physical mechanisms leading to this relaxation typically involve coupling the spin either to orbital motion or to nuclear spins [138, 139, 140, 141, 142, 143, 144]. Relaxation of confined electron spin has been previously measured only for Zeeman or exchange split spin states, where spin-orbit effects dominate [131, 55, 11]; spin flips due to nuclei have been observed in optical spectroscopy studies [12]. Using an isolated double quantum dot and direct time domain measurements, we investigate in detail spin relaxation for arbitrary splitting of spin states. We show that electron spin flips are dominated by nuclear interactions and are slowed by several orders of magnitude with a magnetic field of a few mT.[1]

---

[1] This chapter is adapted from Refs. [145, 146]

8.1 Introduction

The coupling of nuclear spins to electrons in low-dimensional semiconductors is known from optical and transport studies in quantum Hall systems to yield rich physical effects and provide new probes of the relatively isolated quantum system of nuclear spins in solids [147, 148, 149, 150]. Confined electrons interacting with relatively few nuclei are particularly sensitive to hyperfine coupling. This can lead to dramatic effects such as tunnelling currents that slowly oscillate in time and electrical control and readout of nuclear polarization [151, 12]. In this chapter we show that the interaction between single electrons confined in quantum dots with ensembles of lattice nuclei can dominate electron spin relaxation.

We use high-frequency pulsed gates to measure spin relaxation in a GaAs double quantum dot (Fig. 8.1(a)). Measurements are performed near the (1,1) to (0,2) charge transition, where (n, m) denotes the absolute number of electrons on the left and right dots. In the (0,2) configuration, the two electrons form a spin singlet to avoid the large Pauli exclusion energy cost (0.4 meV $\gg kT \approx 10$ μeV) of occupying an excited orbital state [130]. In the separated (1,1) configuration, the two electrons may occupy any spin state. That is, apart from any Zeeman energy (~ 2.5 μeV at 100 mT), the singlet, (1,1)S, and three triplets, (1,1)T$_-$, (1,1)T$_0$, and (1,1)T$_+$ ($m_s = -1, 0, 1$ respectively), are effectively degenerate, given the weak interdot coupling to which the system is tuned.

Spin relaxation is measured by preparing an unpolarized mixture of (1,1) states and monitoring the probability of transition to (0,2)S after the latter is made lower in energy by changing the electrostatic gate configuration. The different local environ-

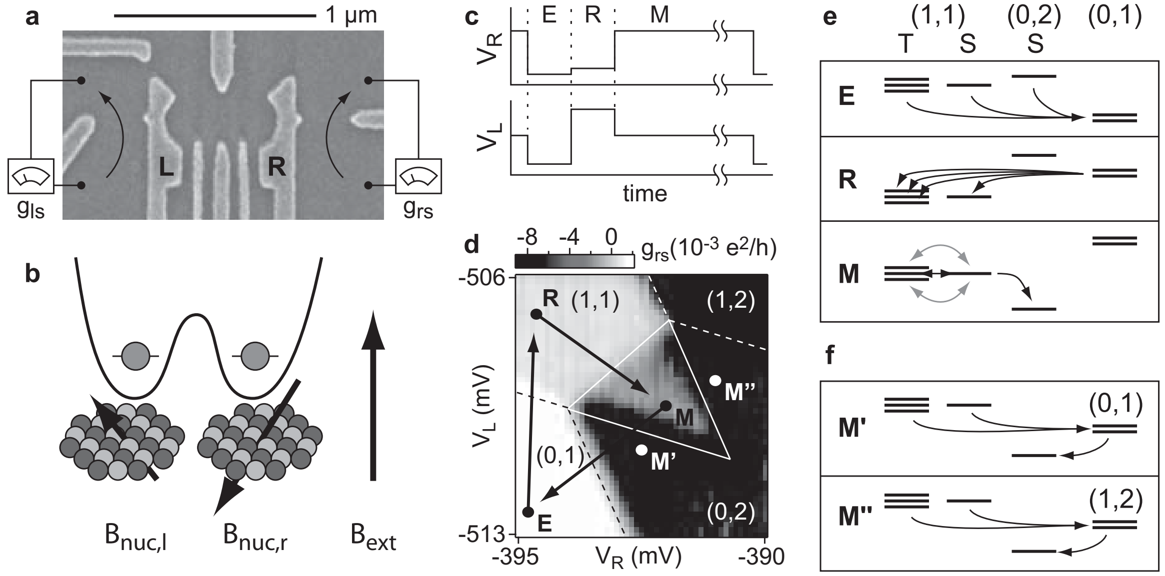

Figure 8.1: Spin-selective tunnelling in a double quantum dot. a) Micrograph of a device similar to the one measured. Metal gates deplete a two-dimensional electron gas 100 nm below the surface, with density 2×10^{11} cm^{-2}. A double dot is defined between gates L and R. Electrons tunnel between the dots and to conducting leads. Conductances g_{ls} and g_{rs} of the left and right QPCs reflect average occupation of each dot. b) In (1,1), spatially separated electrons feel different effective fields from hyperfine interaction with the local Ga and As nuclei, plus a uniform external field. c) Voltage pulses on gates L and R cycle through three configurations: empty (E), reset (R) and measure (M). d) Right sensor conductance g_{rs} as a function of dc voltages on the same two gates around the (1,1) to (0,2) transition, with pulse displacements shown by points E, R, and M. Dashed lines outline the (0,1), (1,1), (0,2), and (1,2) charge state plateaus during step M. Inside the solid-outlined 'pulse triangle,' the ground state is (0,2), but higher sensor conductance indicates partially blocked tunnelling. A plane is subtracted from the raw data to remove direct gate-QPC coupling. e) Energetics of the pulse sequence. In (0,2), only the singlet is accessible, whereas in (1,1), singlet and triplet are degenerate. (0,1) and (1,2) are spin-1/2 doublets. Step E empties the second electron, then R loads a new electron into the left dot, occupying all four (1,1) states equally. At M, (0,2)S is the ground state, but only (1,1)S and the $m_s = 0$ triplet (1,1)T$_0$ can tunnel. Mixing of (1,1)T$_+$ and (1,1)T$_-$ with the singlet is weak away from zero field, so their tunnelling is blocked. f) At M', (0,1) has lower energy than (1,1) and provides an alternate, spin-independent path to (0,2). At M'', (1,2) provides this alternate path.

ments acting on the two spins cause the two-electron spin state to evolve in time, and only if this spin state passes near (1,1)S is a transition to (0,2)S allowed. The average occupancy of the left dot, which reflects the probability of this transition, is monitored using the QPC charge sensors. Conductances g_{ls} and g_{rs} of the left and right sensors change by several percent when an electron enters the dot nearest the sensor [71, 84, 91, 126].

8.2 Pulsed-gating technique

The energy levels of each dot were controlled by voltage pulses on gates L and R, as shown in Fig. 8.1(c). The double dot was cycled through three configurations, depicted in Fig. 8.1(e), while measuring the average QPC conductances. In the 'empty' (E) step, the second electron is removed, leaving a (0,1) state. In the 'reset' (R) step, a new second electron is added, initializing the (1,1) state to an unbiased mixture of the singlet, (1,1)S, and the three triplets (1,1)T_-, (1,1)T_0, and (1,1)T_+. In the 'measurement' (M) step, (0,2) is lowered relative to (1,1) until (0,2)S becomes the ground state, while the (0,2) triplets remain inaccessible, above the (1,1) states. Because tunnelling preserves spin, only (1,1)S can relax to (0,2)S, while the (1,1) triplets are spin-blockaded from making this transition [117, 113].

The measurement step accounted for 80% of the pulse period (E and R were each 10%) so the time-averaged charge-sensor signal mainly reflects the charge state during the measurement time, t_M. Figure 8.1(d) shows g_{rs} as a function of the d.c. offsets to gate voltages V_L and V_R with pulses applied. The dashed lines indicate locations of ground-state transitions during the M step, as seen in unperturbed double dots [84].

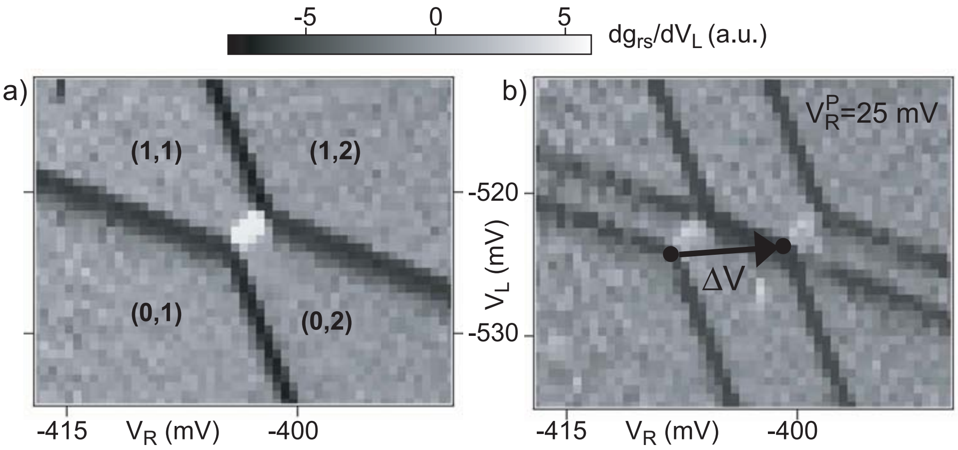

Figure 8.2: Gate pulse calibration. a) dg_{rs}/dV_L as a function of V_R and V_L around the (1,1) to (0,2) charge transition. Charge states are labeled (M, N), where M (N) is the number of electrons on the left (right) dot. b) 25 mV pulses with a 50% duty cycle and 10 μs period are applied to the coax connected to gate R. This results in two copies of the charge stability diagram shifted relative to one another by $\Delta\vec{V}$.

Gate pulses alter this signal only within the 'pulse triangle' (outlined by solid white lines). Here g_{rs} is intermediate between the (0,2) and (1,1) plateaus, indicating that although (0,2) is the ground state, the system is often stuck in the excited (1,1) state. In the regions labelled M' and M'', alternate, spin-independent relaxation pathways, shown in Fig. 8.1(f), circumvent the spin blockade.

Gates L and R are connected via bias tees to dc voltage sources and to pulse generators through coax cables with ~20 dB of inline attenuation.[2] Pulse heights are calibrated by applying pulses to a single gate and measuring the charge stability diagram. Figure 8.2(a) shows the charge sensor signal vs. d.c. gate voltages V_L and V_R with no pulses applied, differentiated with respect to V_L. Because of the differentiation, steps in the sensor signal (marking boundaries between ground state charge configurations, as seen e.g. in Fig. 8.1(d)) appear as dark or bright lines. Figure 8.2(d)

---

[2] We use Anritsu K251 bias tees. Tektronix AWG520 arbitrary waveform generators (with $\sim$ 1 ns rise times and 10-bit vertical resolution) are used for high speed manipulation of the gate voltages.

shows the same charge stability diagram acquired with square pulses applied to gate R (25 mV pulse height before the attenuators, 50% duty cycle, period τ=10 μs). This results in two copies of the charge stability diagram, the right-most (left-most) charge stability diagram reflects the ground state charge configuration during the low (high) stage of the pulse sequence. The gate-voltage offset between them, $\Delta\vec{V}$, is used to calibrate pulse amplitudes. For this pulse, $\Delta\vec{V}$ is not purely horizontal as one might expect (since it is applied solely to gate R, the horizontal axis), but is angled upward slightly, indicating that there is more cross-coupling between gates at a.c. than at d.c. Additional calibrations are performed for gate L, which primarily shifts the honeycomb in the vertical direction (not shown). A linear combination of pulses on gates R and L can then be used to shift the stability diagram in any direction in gate space.

8.3 Spin relaxation measurements

Our spin relaxation measurement technique relies on the fact that (1,1)T to (0,2)S transitions are spin blocked. Two control experiments demonstrate that the observed time dependence of the charge sensing signal is due to spin blocked transitions rather than simply slow inelastic interdot tunneling. The first is to compare the pulse sequence described above (Fig. 8.1) with a reversed pulse sequence, where the M point is in (1,1) while the R point is in (0,2). Now tunneling from R to M should always proceed on a time scale set by the interdot tunnel coupling, since the (0,2)S to (1,1)S transition is not spin blocked. Although these data are not shown, no signal is seen in the pulse triangle for this reversed sequence unless t_M is dramatically reduced,

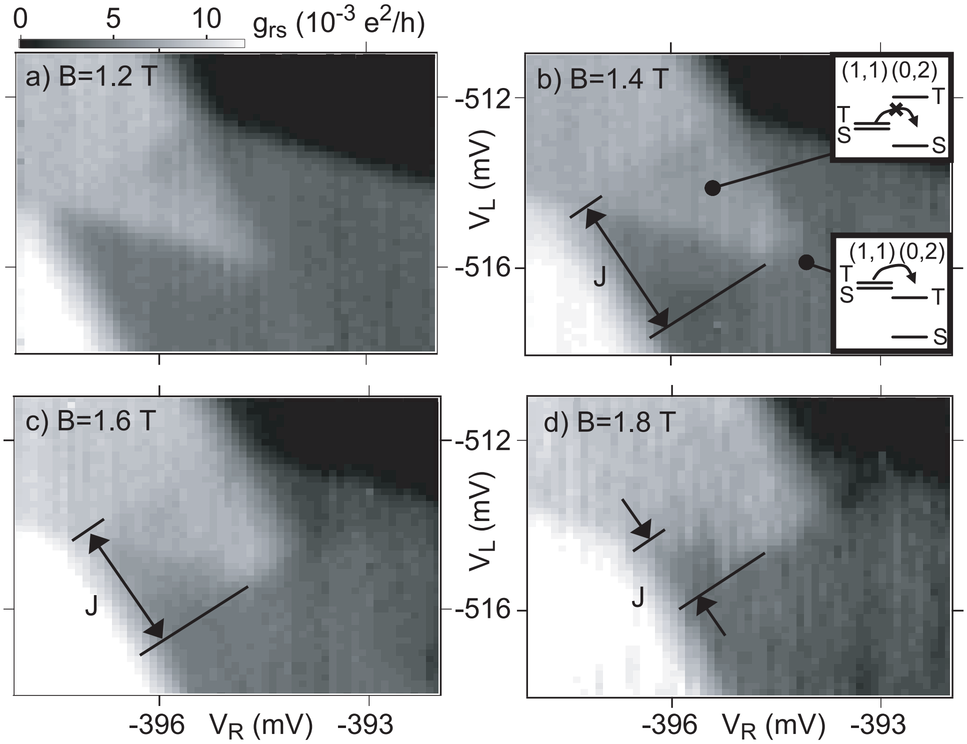

Figure 8.3: g_{rs} as a function of V_R and V_L for increasing B (which reduces J), with τ_M=10 μs. Eventually (0,2)T is lowered into the pulse triangle [inset of (b)]. At this point, (1,1)T to (0,2)T transitions are energetically possible and the transition from the (1,1) to (0,2) charge state is no longer "spin blocked". This cuts off the tip of the pulse triangle in (0,2), see (b). A best-fit plane has been subtracted from the data in (a)–(d).

confirming that long persistence time of the forward pulse sequence is not simply due to a long inelastic tunneling time.

The second control experiment measures signal in the pulse triangle as a function of a large magnetic field B. Throughout this experiment B is applied perpendicular to the sample plane, and as shown in Ch. 7, we expect that such a field will decrease the (0,2) singlet-triplet splitting from ~ 800 μeV at $B = 0$ to zero when $B \sim 2$ T. Figure 8.3(a) shows g_{rs} as a function of V_L and V_R while applying the forward pulse sequence with $B = 1.2$ T and $\tau = 10$ μs. For these data, the M-point detuning where (0,2)T has lower energy than the (1,1) states resides outside of the pulse triangle

($J > E_M$, the mutual charging energy) and the (1,1)T to (0,2) transitions are spin blocked. For $B = 1.4$ T (Fig. 8.3(b)) the (0,2)T state is low enough in energy that the (1,1)T states can directly tunnel to the (0,2)T manifold at high detunings. Now (1,1) to (0,2) tunneling can proceed, and there is no longer a (1,1) charge signal in the (0,2) region of the pulse triangle at high detuning. This cuts off the tip of the pulse triangle. The spin-blocked region continues to shrink as B is increased. From these data, we find $J \sim$340, 280, and 180 μeV for B=1.4, 1.6, and 1.8 T respectively,[3] consistent with the values derived from d.c. transport in Fig. 7.4(f).

For smaller fields, the B and t_M dependence of the charge sensor signal is shown in Fig. 8.4. With $t_M = 8$ μs, a large signal is seen in the pulse triangle, indicating that some of the (1,1) to (0,2) transitions are spin blocked. As t_M is increased this signal decreases (Fig. 8.4(b)), indicating that t_M is approaching the (1,1) singlet-triplet relaxation time. This is accompanied by a reduction in the pulse triangle size due to thermally activated processes as in Fig. 8.1(f). Similar data, but at $B = 0$, are plotted in Figs. 8.4(c) and (d). The signal in the pulse triangle is noticeably weaker for the same t_M, particularly near the (1,1)-to-(0,2) charge transition, indicating enhanced spin relaxation.

Detailed measurements of residual (1,1) occupation as a function of detuning (the energy difference between the (1,1) and (0,2) states) are shown in Fig. 8.5. Conductances g_{ls} and g_{rs} were measured along the diagonal white line in the upper panel of Fig. 8.5, for various values of B and t_M, and converted to occupation $\langle N \rangle$ by scaling to the average (1,1) and (0,2) levels outside the pulse triangle. Data are shown in

---

[3] The gate-voltage to energy conversion is determined from finite-bias triangles as described in Ch. 7.

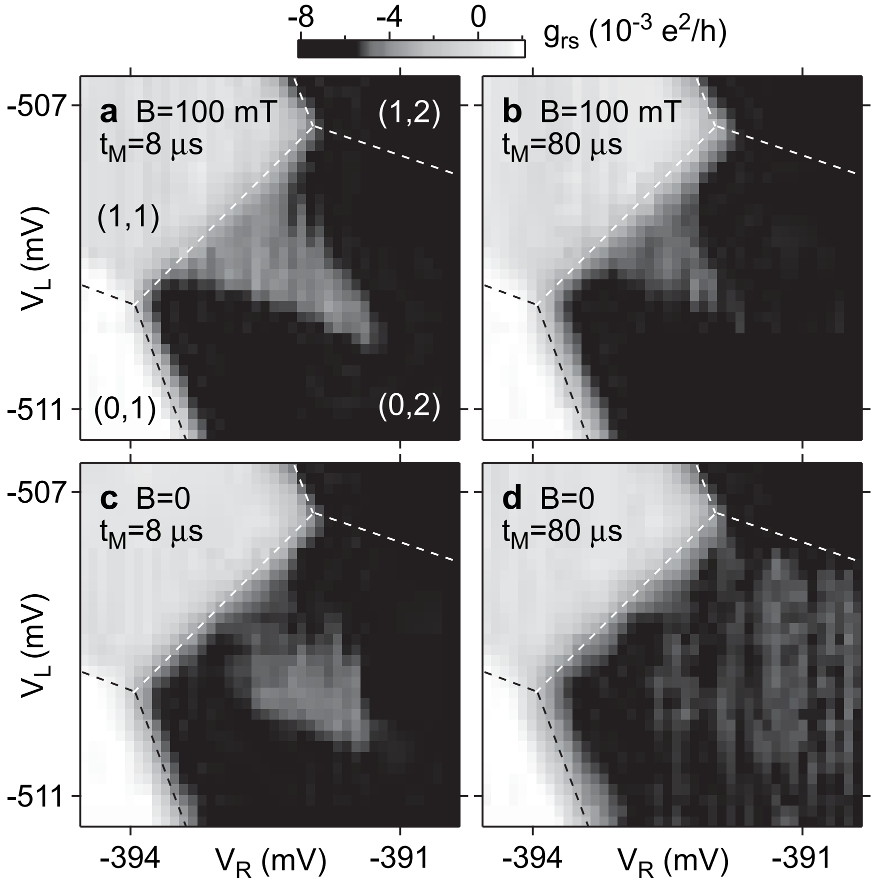

Figure 8.4: Dependence of the occupancy of the (1,1) state on measurement time, t_M, and external field, B. a) Charge sensor conductance, g_{rs}, as a function of V_L and V_R with short pulses ($t_M = 8$ μs) at $B = 100$ mT. Large average occupation of (1,1) is seen throughout the pulse triangle. Near the triangle edges, thermally activated tunnelling to the leads allows fast relaxation to (0,2), (see Fig. 8.1(f)). b) For longer pulses ($t_M = 80$ μs), thermally relaxed triangle edges expand towards the centre of the triangle. c) At $B = 0$, the (1,1) occupation is extinguished at low detuning (near the (1,1)-(0,2) charge transition) as tunnelling to (0,2) becomes possible from the (1,1)T$_+$ and (1,1)T$_-$ states. d) Combine these two effects at zero field with long pulses, and no residual (1,1) occupation is seen, indicating complete relaxation to (0,2).

detail for the points labelled A through D. As in Fig. 8.4, strong field dependence was found at low detuning (point A), where inelastic interdot tunnelling dominates. This field dependence vanishes at higher detuning where thermally activated tunnelling to the leads dominates.

As in previous work [141, 12], we model spin evolution in (1,1) by treating the ensem-

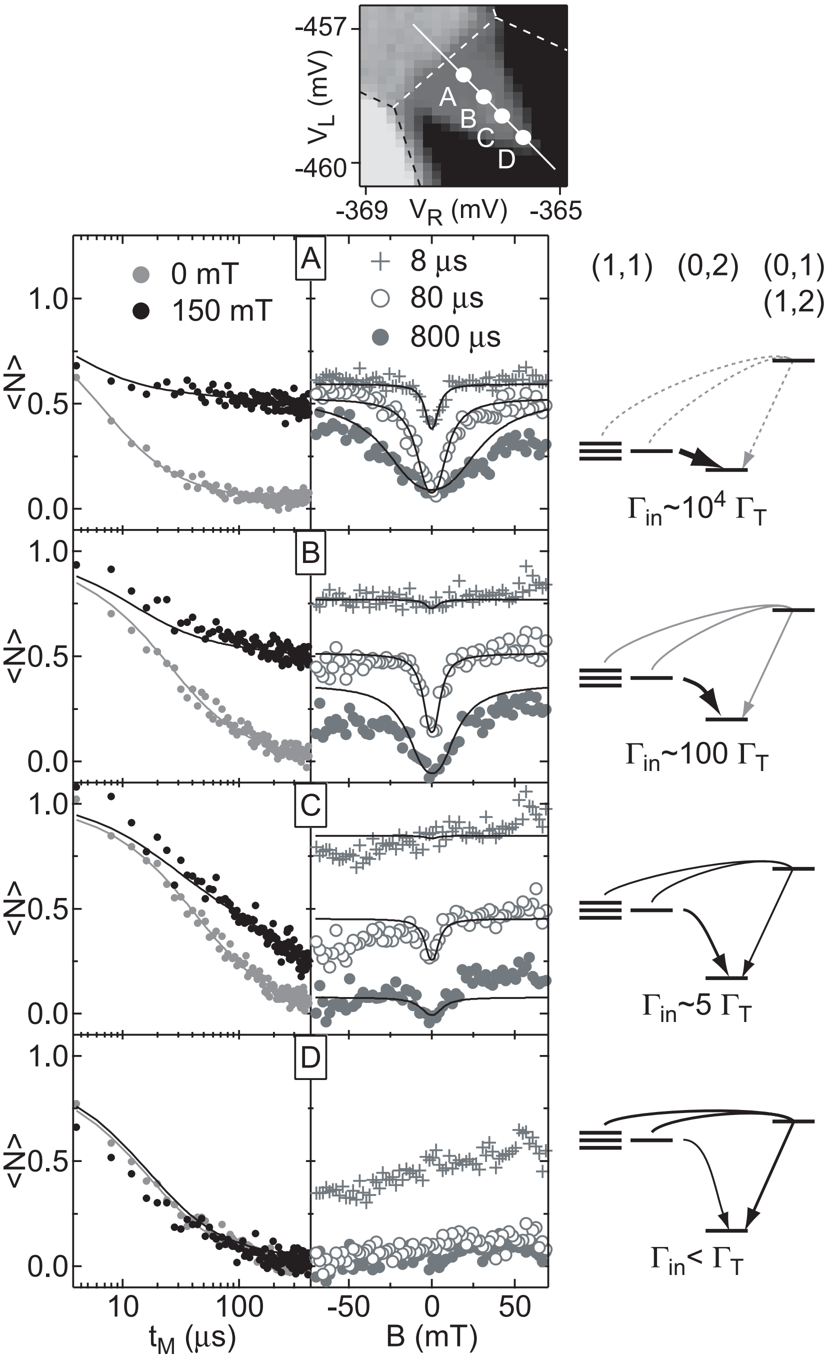

Figure 8.5: Detailed measurements of blockaded (1,1) occupation. Average occupation $\langle N \rangle$ of the (1,1) charge state, based on calibrated charge sensor conductances, at four detuning points (labelled A, B, C, D in the uppermost panel). Left panels show $\langle N \rangle$ as a function of t_M at $B = 0$ and $B = 150$ mT. Middle panels show $\langle N \rangle$ as a function of B for different t_M times. Diagrams at right show schematically the relative position of energy levels and the extracted ratios of inelastic (Γ_{in}) to thermal (Γ_T) decay rates.

ble of nuclear spins within each dot as a static effective field $\mathbf{B}_{nuc}$ with slow internal dynamics, that adds to any applied Zeeman field (see Fig. 8.1(b)). $\mathbf{B}_{nuc}$ is randomly oriented with r.m.s. strength $B_{nuc} = b_0\sqrt{I_0(I_0+1)/N_{nuc}}$, where $b_0 = 3.5$ T is the hyperfine constant in GaAs, $I_0 = 3/2$ is the nuclear spin and N_{nuc} is the effective number of nuclei with which the electron interacts [139, 140, 152, 153]. In our dots, N_{nuc} is estimated at 10^6–10^7, giving $B_{nuc} \approx$ 2–6 mT. The spins precess in a characteristic time $t_{nuc} = \hbar/g^*\mu_B B_{nuc} \approx$ 3–10 ns, which can be regarded as an inhomogeneous dephasing time T_2^*. At $B = 0$, all four (1,1) spin states mix in this time, and tunnelling will appear insensitive to spin. With $B > B_{nuc}$, however, only (1,1)T$_0$ and (1,1)S are degenerate. These will continue to mix with the same rate, but (1,1)T$_+$ and T$_-$ will be frozen out.

8.4 Analysis and discussion

To model this mixing, we assume static nuclear fields during each pulse, a spin-preserving inelastic interdot tunnelling rate Γ_{in} from (1,1)S to (0,2)S, and a spin-independent rate Γ_T due to thermally activated tunnelling via the (0,1) and (1,2) charge states (see Ap. A for details). Zeeman eigenstates for two spins in fields $B\hat{\mathbf{z}} + \mathbf{B}_{nuc,l}$ and $B\hat{\mathbf{z}} + \mathbf{B}_{nuc,r}$, denoted $|(1,1)s,s'$ ($s, s' = \pm 1/2$), decay to (0,2)S on the basis of their overlap with (1,1)S, with rates $\Gamma_{s,s'} = \Gamma_{in}|\langle(1,1)\mathrm{S}|(1,1)s,s'\rangle|^2$ as long as $\Gamma_{in} \ll g^*\mu_B B_{nuc}$. Averaging over nuclear field configuration and short-time dynamics gives decay rates for the T$_\pm$-like states:

$$\Gamma_{\pm\frac{1}{2},\pm\frac{1}{2}} = \frac{\Gamma_{in}}{4(1+(B/B_{nuc})^2)} \tag{8.1}$$

and $\Gamma_{\pm\frac{1}{2},\mp\frac{1}{2}} = \Gamma_{in}/2 - \Gamma_{\pm\frac{1}{2},\pm\frac{1}{2}}$ for the S-like and T_0-like states. At $B = 0$, total transition rates for all (1,1) states into (0,2)S are the same, $\tau_0^{-1} = \Gamma_{in}/4 + \Gamma_T$. For $B > B_{nuc}$, transition rates $\tau_B^{-1} = \Gamma_{\pm\frac{1}{2},\pm\frac{1}{2}} + \Gamma_T$ from (1,1)$T_\pm$ to (0,2)S are suppressed by field, while transitions from (1,1)S and (1,1)T_0 to (0,2)S are accelerated by up to a factor of two because they no longer mix with (1,1)$T_\pm$. During the gate-pulse transition from R to M, the relatively fast transition from (1,1)S to (0,2)S allows a fraction q of the (1,1)S state to transfer adiabatically to (0,2)S, reducing the initial occupation of (1,1)S. The resulting average occupancy N of (1,1) after a time t_M is:

$$N(t_M) = \frac{1}{t_M}\int_0^{t_M} dt(\frac{1}{2}e^{-t/\tau_B} + \frac{2-q}{4}e^{-t(2\tau_0^{-1}-\tau_B^{-1})}) \qquad (8.2)$$

Experimentally measured values for N as functions of t_M and B for various detunings are shown in Fig. 8.5, along with fits to the above theory. An additional field-independent parameter, N_∞, accounts for non-zero $N(t_M)$ at long times owing to thermal occupation of (1,1). N_∞ is zero at large detuning but increases, as expected, near zero detuning. Non-zero q values are found only at very low and very high detuning (where the R point is near zero detuning), where the slew rate of the pulse is low as it crosses to (0,2). With these parameters and τ_0 set for a given detuning by fitting the zero-field data (gray), the high-field data (black) are fitted with just the longer decay times τ_B for the (1,1)$T_\pm$ states. The field-dependence curves are then fully determined by B_{nuc}, which is most accurately determined from data in Fig. 8.6, as discussed below. Drift in sensor conductance over long field sweeps is compensated by allowing a vertical shift in the field-dependence curves. The depth and width of the dips in these curves are not adjustable.

Figure 8.6 shows the extracted decay times τ_0 and τ_B versus detuning for various fields. As the magnetic field increases, more points at high detuning fall along a line in this semi-log plot, denoting exponential energy dependence as expected for a thermally activated process. This persists over three orders of magnitude at the highest field, and with calibration from transport measurements yields a temperature of 160 ± 20 mK. At zero field, thermal decay dominates only at the highest detunings, and the low-detuning times are well fitted by a power-law function of detuning with exponent 1.2 ± 0.2 and offset 700 ns, typical of inelastic tunnelling in double quantum dots [127]. Adding these two processes gives the zero-field theory curve in Fig. 8.6, in good agreement with the zero-field data. The 10-mT curve is fitted using these zero-field parameters, but with times for the inelastic component increased by the factor $(1 + (B/B_{nuc})^2)$ from Eq. 8.1. The fit gives $B_{nuc} = 2.8 \pm 0.2$ mT, or $N_{nuc} \approx 6 \times 10^6$, within expectations. This value uniquely determines the remaining theory curves. For τ_B longer than about 1 ms the decay is faster than theory predicts (though still 10^3 times slower than at $B = 0$), indicating that another mechanism such as spin-orbit coupling may operate on millisecond timescales [131, 55, 11]. Spin-orbit coupling is expected to dominate spin relaxation at external fields of several tesla [55]. This regime is better suited to parallel fields, which couple almost exclusively to spin, than to the perpendicular orientation used here, which affects orbital wavefunctions at high fields.

Given B_{nuc} above, the model predicts an inhomogeneous dephasing time $T_2^* \approx 9$ ns for this device, which is independent of external field despite the enhanced relaxation times measured at higher fields. Up to 1 ms, the excellent agreement between experiment and theory indicates that hyperfine interaction is the only relevant source of spin relaxation in this system. Several strategies are available to circumvent this

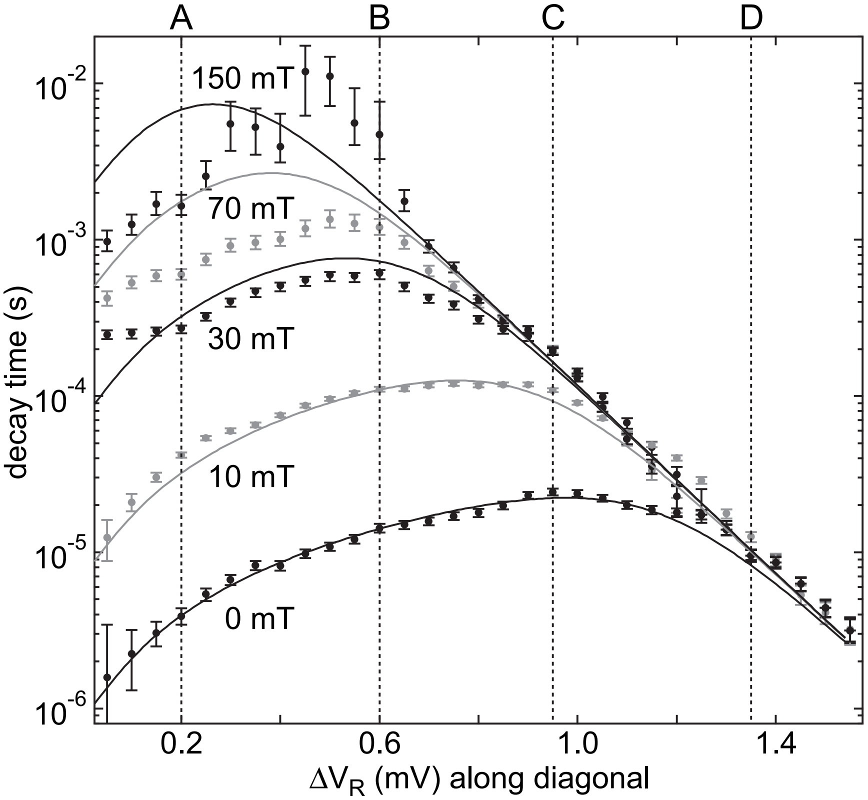

Figure 8.6: Decay of (1,1) occupancy as a function of detuning at various magnetic fields. Dotted lines mark the locations of points A through D from Fig. 8.5. Fit of zero field theory (lowest curve) to data sets all fit parameters except B_{nuc}, which is determined by fitting to the 10-mT data. Theory curves at other fields are then fully determined. Error bars at zero field result from the least-squares fitting. Error bars at non-zero field reflect changes in the resulting decay rate as the zero-field fitting parameters are varied within their uncertainties.

short dephasing time. Materials with zero nuclear spin, such as carbon nanotubes, avoid hyperfine effects entirely. Controlling B_{nuc} via nuclear polarization [12, 151] is tempting, but high polarization is required for T_2^* to increase substantially [154]. An alternative is to use spin echo techniques such as pulsed electron spin resonance to extend coherence to the nuclear spin correlation time, expected to be of the order of 100 μs in these devices [141].

We thank H. A. Engel and P. Zoller for discussions. This work was supported by the ARO, the DARPA-QuIST programme, and the NSF, including the Harvard NSEC.

Chapter 9

Singlet separation and dephasing in a few-electron double quantum dot

J. R. Petta[a], A. C. Johnson[a], J. M. Taylor[a], A. Yacoby[a,b], M. D. Lukin[a],
C. M. Marcus[a], M. P. Hanson[c], A. C. Gossard[c]
[a]*Department of Physics, Harvard University, Cambridge, Massachusetts*
[b]*Department of Condensed Matter Physics, Weizmann Institute of Science, Rehovot, Israel*
[c]*Department of Materials, University of California, Santa Barbara, California*

Quantum computation and information processing requires generation and manipulation of entangled states. While several recent experiments show that spin relaxation times (T_1) in GaAs quantum dots can approach several ms, a direct time-resolved measurement of the spin dephasing time T_2^*, has to date not been reported. Here we measure T_2^* for single electrons confined in a gate-defined double quantum dot using time-domain interferometry of correlated electron pairs. The measured $T_2^* = 10$ ns is well accounted for by a model of hyperfine interactions with the GaAs nuclei.[1]

---

[1] This chapter has not appeared in print. An expanded version including more complex Rabi and spin-echo pulse sequence measurements is in press at Science.

9.1 Introduction

Coupled GaAs quantum dots allow controlled isolation of one or more electrons [115, 25]. These devices may be well suited for quantum information processing because the tunnel couplings, exchange interactions, and electron occupation can be easily changed by tuning gate voltages and external magnetic fields [101]. In addition, the time it takes for a single spin to relax (T_1) has been shown to be very long, making electron spin a good candidate for quantum information storage [131, 55, 11, 146]. Coherent manipulation of spin states for quantum computation requires that the spin dephasing time T_2^* be much longer than the typical gate operation time. A measurement of this figure of merit has to date not been reported for spins in quantum dots. Knowledge of this timescale is crucial because a short T_2^* will likely hinder some applications of coherent spintronics [155]. Time-resolved Faraday rotation measurements in bulk GaAs systems have demonstrated spin dephasing on 100 ns timescales, but this timescale cannot be directly applied to quantum dots because the mechanisms for spin dephasing have different strengths in confined systems [156, 144, 47]. Pioneering optical spectroscopy measurements and charge sensing experiments have measured the relaxation of electron spin polarization at zero field (See [12] and Ch. 8). A direct time-resolved measurement of T_2^* for a single spin in a quantum dot is lacking.

Two potentially important sources of spin dephasing are spin-orbit and hyperfine (electron-nuclear spin) interactions. Theoretical estimates indicate that spin-orbit coupling should not cause rapid spin dephasing of electrons in GaAs dots, giving, for this mechanism, $T_2 = 2T_1 \sim 1$ ms [144]. On the other hand, dephasing due to the hyperfine interaction may be quite rapid [139, 157, 140, 141, 142]. In a simplified picture, the hyperfine interaction in a GaAs quantum dot creates an effective magnetic field, $B_{nuc} = b_0\sqrt{I_0(I_0+1)/N_{nuc}}$, where $b_0 \sim 3.5$ T is the hyperfine constant in GaAs, $I_0 = 3/2$ is the nuclear spin of all species, and N_{nuc} is the effective number of nuclei with which the electron interacts [152]. As discussed below (and in Ch. 8), $N_{nuc} \sim 6 \times 10^6$ in our devices, giving $B_{nuc} \sim 3$ mT. Since these fields are uncorrelated in different quantum dots, two spatially separated electron spins will dephase on a timescale $t_{nuc} = \sqrt{3}\hbar/(g^*\mu_B B_{nuc}) \sim 10$ ns, which can be regarded as an inhomogeneous dephasing time T_2^* [157].

We directly measure the spin dephasing time in an isolated GaAs double quantum dot, fabricated on a GaAs/AlGaAs hetrostructure grown by MBE, using pulsed gates and quantum point contact (QPC) charge sensing [71, 91, 126], as shown in Fig. 9.1. QPC conductance, g_s, measured as a function of the gate voltages V_L and V_R, is plotted in Fig. 9.1(b) and maps out the double dot charge stability diagram. Labeling charge states with the integer pair (n, m) (the second index indicating the sensed right dot), we focus on transitions involving the (0,2) and (1,1) states, where previous experiments have demonstrated spin-selective tunneling (see [146, 117] and Ch. 7).

The measurement protocol is illustrated in Fig. 9.1(c). We first initialize the system in the (0,2) singlet ground-state (denoted (0,2)S), which is separated by ~400 μeV from the first triplet state of (0,2). At time $t = 0$, the double-well potential is tilted to make the (1,1) charge state the new ground state. This induces a transition from (0,2)S into the spatially separated (1,1) singlet state, (1,1)S. For $B = 0$ and interdot tunneling, t_c, tuned to be weak,[2] such that (1,1)S is nearly degenerate with the three (1,1) triplet

---

[2] Tunnel coupling is chosen stronger here than in Ch. 8 so that charge may be adiabatically transferred between dots (described in detail below), in contrast to the purely inelastic transfer in Ch. 8.

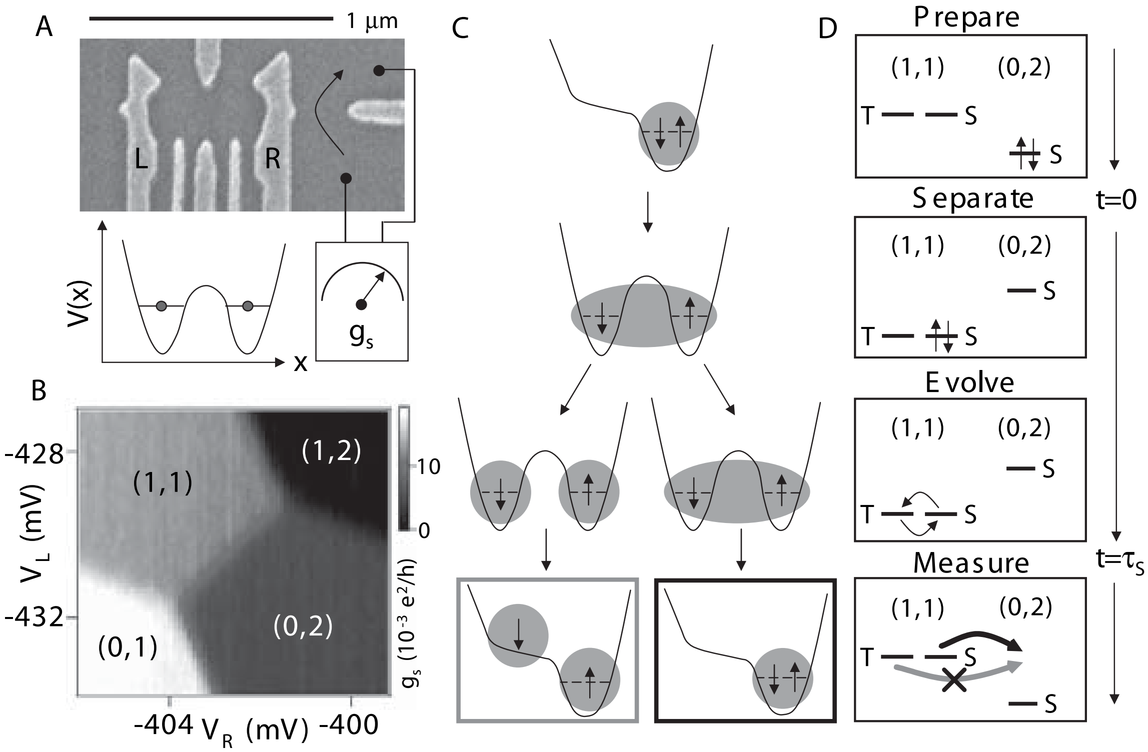

Figure 9.1: a) Scanning electron micrograph of a sample identical to the one used in this experiment. Voltages on gates L and R control the number of electrons in the left and right dots. The QPC conductance, g_s, is sensitive to the number of electrons in the double dot. b) g_s measured as a function of V_L and V_R reflects the double dot charge stability diagram. Charge states are labeled (m, n), where $m(n)$ is the number of electrons in the left(right) dot. c) Measurement protocol. The double dot is initialized in the spin singlet, (0,2)S. At $t = 0$, the spin singlet is spatially separated into (1,1)S. The separated electrons are left to evolve in the presence of hyperfine and spin-orbit interactions until $t = \tau_s$. At $t = \tau_s$ we make a projective measurement by tilting the double well potential so that (0,2)S becomes the ground state. (1,1)T to (0,2)S transitions are spin blocked, while (1,1)S to (0,2)S transitions proceed freely. The QPC detects spin-blocked transitions. d) Energy level configuration at each stage of the experiment.

states, (1,1)T$_+$, (1,1)T$_0$, and (1,1)T$_-$ (representing $m_s = +1, 0, -1$), mixing between all spin states occurs rapidly. Splitting off the (1,1)T$_+$ and (1,1)T$_-$ states with an external Zeeman field allows rapid mixing only between (1,1)S and (1,1)T$_0$. At time $t = \tau_s$, the double-well potential is tilted to again make (0,2)S the ground state. This projects the evolved (1,1) spin state onto (0,2)S. Due to spin selection rules, only (1,1)S can tunnel to (0,2)S, while (1,1)T to (0,2)S transitions are blocked. Failure to return to the (0,2) charge state, as reflected in the QPC conductance, indicates that the return transition was spin blocked, and hence dephasing occurred during the time τ_s [146]. This procedure is analogous to a time-domain interferometer, where two correlated electrons are separated, recombined, and measured.

To implement this protocol, voltage pulses were applied to gates L and R using a two-channel arbitrary waveform generator. The four-step pulse sequence is shown in Fig. 9.2(a). The system is initialized into (0,2)S by waiting at point P for 200 ns. Then (0,2)S is transferred to (1,1)S by pulsing to point S, passing through an intermediate point P' for 200 ns to reduce pulse overshoot. The gates are then held at point S for a duration τ_s followed by a spin-state projection measurement by pulsing to point M, where (0,2)S becomes the ground state, and holding for 9.4 μs before the cycle is repeated. Spin-blocked transitions are detected by measuring the time-averaged QPC conductance g_s, which reflects the configuration at point M, since $> 95\%$ of the cycle time is spent there.

9.2 The spin funnel

Interdot tunnel coupling, t_c, causes a splitting of (0,2)S and (1,1)S, lowering the energy of the hybridized (1,1)S–(0,2)S state by $t_c^2/(2|\epsilon_s|)$ to leading order in t_c/ϵ_s (i.e. far from degeneracy), where ϵ_s is the energy shift away from the (0,2)–(1,1) charge degeneracy point. Because of this splitting, the (1,1)T_+ state will cross the hybridized (1,1)S at finite Zeeman field, such that $\epsilon_s = t_c^2/(2g^*\mu_B B)$, as illustrated in Fig. 9.2(c). In the vicinity of this degeneracy, rapid mixing of (1,1)S and (1,1)T_+ states can occur, and the probability of getting stuck in (1,1) after the projective measurement onto

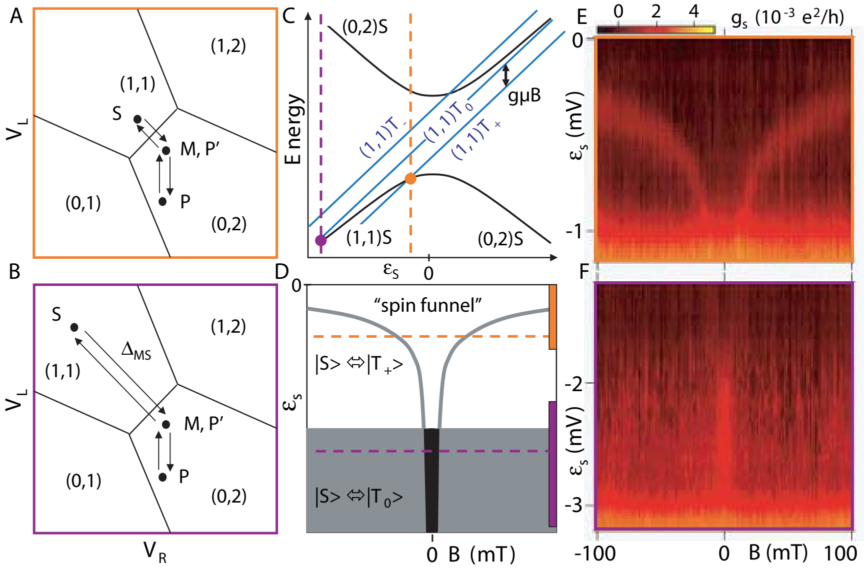

Figure 9.2: Spin dephasing in a double dot. a) Pulse cycle $P \rightarrow P' \rightarrow S \rightarrow M \rightarrow P$ for a small separation Δ_{MS} between the M and S points. b) Pulse sequence for a large Δ_{MS}. c) Finite interdot tunnel coupling results in a tunnel splitting at zero detuning. Tuning ϵ_s probes different regions of this energy level diagram. For small Δ_{MS} (resulting in a small ϵ_s), (1,1)S and (1,1)T$_+$ are in resonance at finite field. A larger Δ_{MS} (more negative ϵ_s) probes dephasing between (1,1)S and (1,1)T$_0$ at high field. At $B = 0$, (1,1)S can mix with all three (1,1)T states, enhancing the probability to remain in a spin blocked configuration. d) Schematic grey-scale plot of the probability to remain in a (1,1)T spin blocked state, $P_{(1,1)}(\tau_s \gg T_2^*)$ derived from the energy level diagram in (c). The spin funnel corresponds to mixing between (1,1)S and (1,1)T$_+$ and results in $P_{(1,1)}(\tau_s \gg T_2^*) = 1/2$. For very negative ϵ_s, (1,1)S to (1,1)T$_0$ dephasing occurs at finite field, resulting in a broad band of signal with $P_{(1,1)}(\tau_s \gg T_2^*) = 1/2$. At $B = 0$, (1,1)S can mix with all three triplet states and $P_{(1,1)}(\tau_s \gg T_2^*) = 2/3$. e) g_s measured as a function of ϵ_s and B using the pulse sequence illustrated in (a), $\Delta_{MS} = (-1, 1.05)$ mV, $\tau_s = 200$ ns. f) g_s measured as a function of ϵ_s and B using the pulse sequence illustrated in (b), $\Delta_{MS} = (-3, 3.15)$ mV, $\tau_s = 200$ ns.

(0,2)S is $P_{(1,1)}(\tau_s \gg T_2^*) = 1/2$. For more negative ϵ_s, such that $|\epsilon_s| > t_c^2/(2g^* \mu_B B_{nuc})$, different behavior is expected in different field regimes. With $B > B_{nuc}$, (1,1)S and (1,1)T$_0$ will approach degeneracy, resulting in $P_{(1,1)}(\tau_s \gg T_2^*) = 1/2$. For $B < B_{nuc}$, all four (1,1) spin states approach degeneracy. In this regime $P_{(1,1)}(\tau_s \gg T_2^*) = 2/3$. These regimes are illustrated Fig. 9.2(d) in a schematic gray-scale plot representing $P_{(1,1)}(\tau_s \gg T_2^*)$ as a function of ϵ_s and B. The resonance condition set by (1,1)S

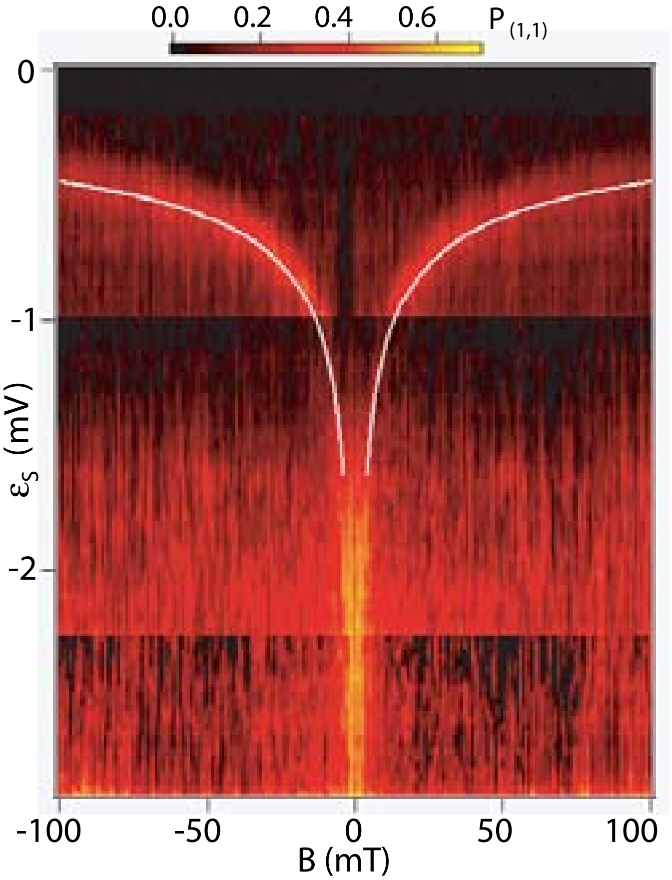

Figure 9.3: Composite plot of $P_{(1,1)}(\tau_s \gg T_2^*)$ measured as a function of ϵ_s and B with $\tau_s = 200$ ns made by combining three separate field sweeps, each with a different Δ_{MS}. For $-1.5 < \epsilon_s < 0$ mV, a well-defined spin funnel is seen. With $\epsilon_s < -1.5$ mV, the zero-field feature is flanked by a signal with roughly half the amplitude that extends out to the highest measured fields. Overlay: a power law fit to the spin funnel gives $\epsilon \propto -|B|^{-0.4}$.

and (1,1)T$_+$ results in the characteristic $1/B$ dependence of the spin funnel. Mixing between (1,1)S and (1,1)T$_0$ states results in a field-independent band of $P_{(1,1)}$ signal at large negative ϵ_s, where $|\epsilon_s| > t_c^2/(2g^*\mu_B B_{nuc})$. Within this band, $P_{(1,1)}$ is further enhanced at low fields, $B < B_{nuc}$, reflecting mixing of (1,1)S with all three (1,1)T states.

A finite singlet-triplet splitting in (0,2) limits the ϵ_s measurement range for a given pulse sequence. To span a wide range of ϵ_s we take several data sets with different separations Δ_{MS} between the S and M points. Figure 9.2(e) shows a plot of g_s as a function of B and ϵ_s with $\Delta_{MS} = (-1, 1.05)$ mV in (V_L, V_R) and $\tau_s = 200$ ns. For small $|\epsilon_s|$ we observe the spin funnel, as described above. For large $|\epsilon_s|$, (probed by setting $\Delta_{MS} = (-3, 3.15)$ mV) we find a field-independent signal, augmented at $B = 0$, as shown in Fig. 9.2(f). A composite image of $P_{(1,1)}$ created by combining three data sets with different Δ_{MS} and $\tau_s = 200$ ns is plotted in Fig. 9.3. The observed spin-blocked signal is in good qualitative agreement with the expected structure illustrated in Fig. 9.2(d). Fitting the spin funnel data to a power law $\epsilon \propto -|B|^{\alpha}$ gives a power $\alpha = -0.4$ rather than the expected $\alpha = -1$, behavior which is not understood at present but which is confirmed by more recent Rabi oscillation and spin-echo experiments.

9.3 Measurement and theory of T_2^*

The spin dephasing time is determined by measuring the spin blocked signal as a function of τ_s. We set $\Delta_{MS} = (-7, 7.35)$ mV, so that $-7 < \epsilon_s < -6$ mV. $P_{(1,1)}(\tau_s)$ is plotted in Fig. 9.4 for both $B = 100$ mT, where the (1,1)S–(1,1)T_0 dephasing process is measured, and $B = 0$ mT, where mixing between (1,1)S and all three triplet states is explored. The average of ten such measurements is shown to reduce signal noise. We find that $P_{(1,1)}$ increases on a $\sim$10 ns timescale and saturates for $\tau_s > 20$ ns at values of $\sim$0.3 for $B = 100$ mT and $\sim$0.5 for $B = 0$ mT. These results are qualitatively consistent with expectations: For $\tau_s \ll T_2^*$, dephasing is minimal, leading to $P_{(1,1)} \sim 0$, i.e., (1,1)S does not have time to evolve into a state that will get stuck in (1,1). As τ_s reaches T_2^*, $P_{(1,1)}$ should rise, since the (1,1)S state will mix

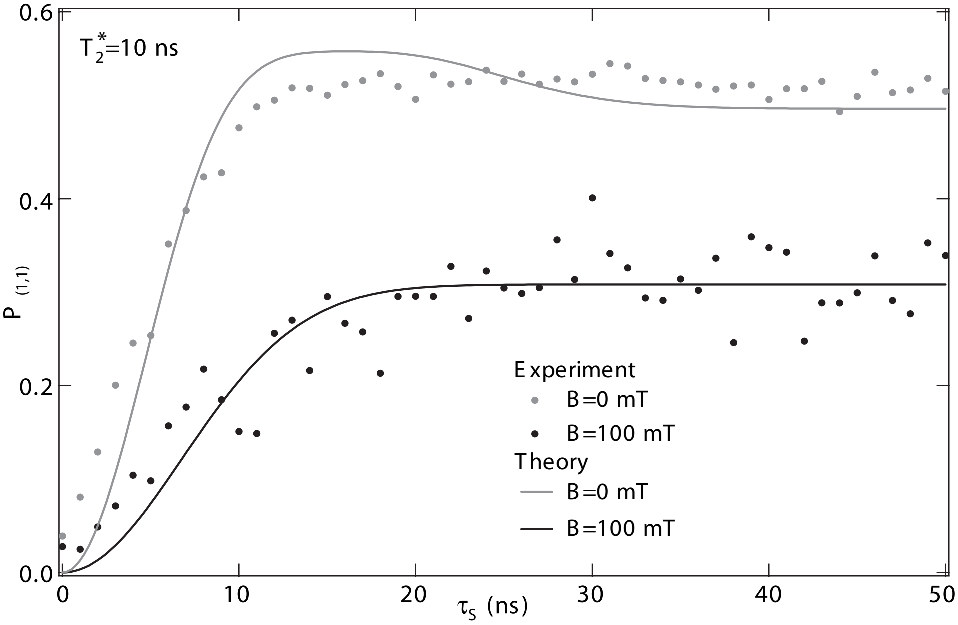

Figure 9.4: $P_{(1,1)}$ measured as a function of τ_s. At $B = 100$ mT, only (1,1)S to (1,1)T_0 dephasing is allowed and $P_{(1,1)}$ approaches ∼0.3 for long τ_s. For $B = 0$ mT, (1,1)S can mix with all three (1,1)T states and approaches ∼0.5 for long τ_s. Theory predicts long-τ_s values of 0.5, 0.67. The ratios of the experimental $P_{(1,1)}$ values are consistent with this expectation to within $< 20\%$, but the overall amplitudes are reduced (see text). The data are fit using a model that accounts for distinct nuclear environments in the left and right dots. Best fits to the data give $B_{nuc} = 2.3$ mT and $T_2^* = 9.6$ ns.

significantly with degenerate (1,1)T states.

To model the experimental $P_{(1,1)}(\tau_s)$ curves, we calculate the probability for (1,1)S to dephase in the presence of two distinct quasi-static nuclear fields acting on the spins in the left and right dots. The resulting functional forms are:

$$P_{(1,1)}(t) = \begin{cases} C_1\left(1-\frac{1}{2}(1+e^{-\frac{t^2}{t_{nuc}^2}})\right), & B \gg B_{nuc} \\ C_2\left(1-\frac{1}{3}(1+e^{-\frac{1}{2}\frac{t^2}{t_{nuc}^2}}(1-\frac{t^2}{t_{nuc}^2})+e^{-\frac{t^2}{t_{nuc}^2}}\left(1-\frac{t^2}{t_{nuc}^2}\right)^2\right), & B = 0 \end{cases} \tag{9.1}$$

Fitting parameters are C_1, C_2, and t_{nuc}. Fitting to the 100 mT data, we find $t_{nuc} = 9.6 \pm 0.5$ ns and $C_1 = 0.62 \pm 0.01$. For the B=0 data we set $t_{nuc} = 9.6$ ns and find a best fit $C_2 = 0.74 \pm 0.01$. Theory predicts an overshoot in P(1,1) for B=0, which is an overdamped remnant of the Rabi oscillations of the electron spin in the hyperfine field. The experimental data do not exhibit this overshoot. More complicated theories may be required to account for this discrepancy. Theory also predicts $C_1 = C_2 = 1$ for 100% population transfer efficiency and perfect initialization. The reduced C_1 and C_2 values found in experiment may result from a residual exchange energy j or non-adiabatic population transfer. In addition, we expect C_1 C_2. Experimentally, these values differ by $< 20\%$. This discrepancy may be due to switching noise in the 100 mT data (evident in the data in Fig. 9.3), which upon signal averaging pulls down the $P_{(1,1)}$ signal level, or finite exchange j. Nevertheless, the field dependence of $P_{(1,1)}$ suggests that only the (1,1)T_0 state is being accessed at 100 mT whereas all three triplet states are accessed at $B = 0$. Since the time dependence predicted by Eq. 9.1 is not a simple exponential form we define $T_2^* = t_{nuc}$, with a best fit value of $T_2^* = 9.6$ ns, corresponding to $B_{nuc} = 2.3$ mT. In principle, T_2^* could be enhanced by polarizing the nuclear spins or taking advantage of their long correlation time. Significant increases in T_2^* would require nearly full nuclear polarization, beyond current capabilities [140, 147]. The anticipated long nuclear correlation time compared to both gating times and electron spin relaxation and dephasing times suggests that approaches based on fast estimation of nuclear fields or echo techniques should be effective.

We acknowledge useful discussions with Hans-Andreas Engel, Emmanuel Rashba, and Peter Zoller. Funding was provided through the ARO under DAAD55-98-1-0270 and DAAD19-02-1-0070, the DARPA-QuIST program, and the NSF under DMR-0072777 and the Harvard NSEC.

Appendix A

Hyperfine-driven spin relaxation

This Appendix details the interaction between nuclei and electrons in a two-electron double quantum dot, as used to derive the theoretical curves for Ch. 8. This section is primarily the work of Jacob Taylor, and appeared as supplemental online material for Ref. [145]

A.1 Definition of B_{nuc}

We start by reviewing the effective magnetic field picture for nuclear spins in a single quantum dot [141], then extend it to the double-dot case. For a single electron in a single quantum dot with large orbital level spacing, i.e., $\hbar\omega \gg |g^* \mu_B B|$, we can write a spin Hamiltonian for the ground orbital state of the dot, $\psi(\mathbf{r})$ and neglect higher orbital states. Including the Zeeman interaction, $H_B = -g^* \mu_B \mathbf{B} \cdot \hat{\mathbf{S}}$, and the hyperfine contact interaction, $H_{HF} = A v_0 \sum_k |\psi(\mathbf{r}_k)|^2 \hat{\mathbf{I}}^k \cdot \hat{\mathbf{S}}$, we can define an effective (Overhauser) magnetic field due to nuclei,

$$\mathbf{B}_{\text{nuc}} = \frac{A v_0}{-g^* \mu_B} \sum_k |\psi(\mathbf{r}_k)|^2 \hat{\mathbf{I}}^k \ , \tag{A.1}$$

such that $H_{\text{tot}} = H_B + H_{\text{HF}} = -g^*\mu_B(\mathbf{B}+\mathbf{B}_{\text{nuc}})\cdot\hat{\mathbf{S}}$ completely determines the spin hamiltonian for a single electron quantum dot ($b_0 = \frac{A}{-g^*\mu_B} = 3.47$ Tesla for GaAs [152]). At temperatures $T \gg \frac{\hbar\gamma_n|\mathbf{B}|}{k_B}$, where γ_n is the gyromagnetic ratio for a given nuclear spin species, the equilibrium state of each nuclear spin is well described an identity density matrix, $\rho_k = \mathbf{1}/(2I_0+1)$; correspondingly, the equilibrium expectation values for $\mathbf{B}_{\text{nuc}}$ are, for large N, equivalent to a Gaussian variable with no mean and a root-mean-square width,

$$\begin{aligned} B_{\text{nuc}} = \sqrt{\langle|\mathbf{B}_{\text{nuc}}|^2\rangle} &= b_0[v_0^2\sum_{kk'}|\psi(\mathbf{r}_k)|^2|\psi(\mathbf{r}_{k'})|^2\langle\hat{\mathbf{I}}^k\cdot\hat{\mathbf{I}}^{k'}\rangle]^{1/2} \\ &= b_0\sqrt{v_0 I_0(I_0+1)\int d^3r\ |\psi(\mathbf{r})|^4}\ . \end{aligned} \tag{A.2}$$

Furthermore, as the internal dynamics of the nuclear field, determined by the nuclear Zeeman energy and Knight shift, are substantially slower than $g^*\mu_B B_{\text{nuc}}$, to a good approximation the field is *quasi-static*, i.e., does not change during the electron-nuclear spin interaction time [141].

For a lateral quantum dot [158] with a Fock-Darwin ground-state wavefunction in xy of rms width $\sigma = \sqrt{\frac{2\hbar}{m^*\omega}}$ and a quantum well confinement wavefunction in z of width l,

$$\psi(\mathbf{r}) = [\frac{16}{l^{3/2}}z\ e^{-4z/l}][\frac{\exp(-\frac{(x^2+y^2)}{4\sigma^2})}{\sqrt{2\pi\sigma^2}}] \tag{A.3}$$

and $B_{\text{nuc}} = b_0\sqrt{I_0(I_0+1)}\sqrt{\frac{3v_0}{8\pi l\sigma^2}} = 2.32\ \text{Tesla}\sqrt{\frac{v_0}{l\sigma^2}} = 18\ \text{mT}\ \sqrt{\frac{\omega[\text{meV}]}{l[\text{nm}]}}$. By comparison to the homogeneous case for a dot of volume V ($\psi(\mathbf{r}) = V^{-1/2}$), we can also define an effective number of nuclear spins, $N = [v_0\int d^3r\ |\psi(\mathbf{r})|^4]^{-1} = \frac{8\pi l\sigma^2}{3v_0}$, such that $\sqrt{\langle|\mathbf{B}_{\text{nuc}}|^2\rangle} = \frac{b_0\sqrt{I_0(I_0+1)}}{\sqrt{N}}$.

For a double quantum dot with one electron in each well, in an external field with negligible exchange coupling ($J = 0$), the spin hamiltonian is

$$H_{(1,1)} = -g^* \mu_B [\mathbf{B}^{(1)} \cdot \hat{\mathbf{S}}^{(1)} + \mathbf{B}^{(2)} \cdot \hat{\mathbf{S}}^{(2)}] \ , \tag{A.4}$$

where $\mathbf{B}^{(i)} = \mathbf{B}_{\text{ext}} + \mathbf{B}_{\text{nuc}}^{(i)}$ is the effective magnetic field in dot i. The eigenstates are spins aligned and anti-aligned with these two fields, $|s, s'\rangle$, with eigenenergies $E_{ss'} = -g^* \mu_B (B^{(1)} s + B^{(2)} s')$ and $s, s' = \pm\frac{1}{2}$. For clarity, we denote eigenstates of only the external magnetic field, e.g., with $B_{\text{nuc}} = 0$, as $\left|\tilde{s}, \tilde{s'}\right\rangle$.

A.2 Hyperfine-driven decay

We take the quasi-static approximation, where we assume that over the course of each cycle of the experiment (one pulse sequence) the nuclear field is static [159]. This requires that the correlation time of the nuclear field be greater than 100 μs, consistent with order kHz linewidths for solid-state NMR on GaAs [152]. We remark that in the existing literature describing relaxation due to nuclei in a single quantum dot [139, 140, 142, 143], the relaxation mechanism we analyze below (spin mixing due to nuclei followed by a direct inelastic decay) is absent, requiring instead a higher-order virtual process for spin relaxation.

We consider an inelastic tunneling mechanism that couples only to charge, leaving the spin state unchanged. In the absence of spin selection rules, the inelastic tunneling takes the charge state (1,1) to (0,2) with a rate Γ_{in}, which is a function of device parameters and energy difference between the two charge states (E_{SG}); such inelastic decay, due, for example, to phonons, has been studied in detail elsewhere [127]. When $\hbar\Gamma_{in} \ll |E_{ss'}|$, we may adiabatically eliminate nuclear spin degrees of freedom. As the ground state of (0,2), $|G\rangle$, is a spin singlet, the decay rate of a state $|s, s'\rangle$ in the (1,1) charge configuration is $\Gamma_{ss'} = \Gamma_{in}| \langle s, s'|S\rangle |^2$, i.e., the probability overlap of the state $|s, s'\rangle$ with the (1,1) spin singlet state, $|S\rangle$, which may then decay via charge-based inelastic decay to $|G\rangle$.

We now evaluate the overlap matrix elements, $| \langle s, s'|S\rangle |^2$. A state $|s\rangle$ for a magnetic field $\mathbf{B} = (x, y, z)$ (and of norm $n = |\mathbf{B}|$) can be expressed in the original basis ($|\tilde{s}\rangle$, spin aligned with the z-axis) as

$$|s\rangle = \frac{-(2s)i(n+z)\,|\tilde{s} = s\rangle - (ix - 2sy)\,|\tilde{s} = -s\rangle}{\sqrt{2n^2 + 2nz}} \ . \tag{A.5}$$

In the tilde-basis, $|S\rangle = (\left|\tilde{\tfrac{1}{2}}, -\tilde{\tfrac{1}{2}}\right\rangle - \left|-\tilde{\tfrac{1}{2}}, \tilde{\tfrac{1}{2}}\right\rangle)/\sqrt{2}$. The overlap elements are then

$$\left|\left\langle S| \pm \frac{1}{2}, \pm\frac{1}{2}\right\rangle\right|^2 = \frac{[(n_1+z_1)x_2 + x_1(n_2+z_2)]^2 + [(n_1+z_1)y_2 + y_1(n_2+z_2)]^2}{8(n_1^2 + n_1 z_1)(n_2^2 + n_2 z_2)} , \tag{A.6}$$

$$\left|\left\langle S| \pm \frac{1}{2}, \mp\frac{1}{2}\right\rangle\right|^2 = \frac{[(n_1+z_1)(n_2+z_2) + x_1 x_2 + y_1 y_2]^2 + [-x_1 y_2 + y_1 x_2]^2}{8(n_1^2 + n_1 z_1)(n_2^2 + n_2 z_2)} \ . \tag{A.7}$$

The states with the same $|m_s|$ value (in the instantaneous, s, basis) have the same overlap. Averaging over all quasi-static field values, we can find $\langle\Gamma_{ss'}\rangle$, the effective decay rate for an experiment with many different realizations, each with a different field value drawn from the field distribution. If the external field is aligned along one axis, i.e., z-axis, then $\langle z_i\rangle = B, \langle x_i\rangle = \langle y_i\rangle = 0, \langle(\mu_i - \delta_{\mu z}B)(\nu_j - \delta_{\nu z}B)\rangle = \delta_{ij}\delta_{\mu\nu}B_{\text{nuc}}^2/3$. By taking advantage of the factorization of expectation values for dots 1 and 2, e.g., $\langle f(\mathbf{B}_1)g(\mathbf{B}_2)\rangle = \langle f(\mathbf{B}_1)\rangle\langle g(\mathbf{B}_2)\rangle$, we find

$$\langle\Gamma_{\pm\frac{1}{2},\pm\frac{1}{2}}\rangle = \Gamma\langle F\rangle\langle G\rangle \tag{A.8}$$

$$\langle\Gamma_{\pm\frac{1}{2},\mp\frac{1}{2}}\rangle = \frac{\Gamma}{2}(\langle F\rangle^2 + \langle G\rangle^2) \tag{A.9}$$

where

$$\langle F\rangle = \left\langle\frac{(n+z)^2}{2n^2 + 2nz}\right\rangle = \left\langle\frac{n+z}{2n}\right\rangle$$

$$\langle G \rangle \;=\; \left\langle \frac{x^2+y^2}{2n^2+2nz} \right\rangle = \left\langle \frac{n^2-z^2}{2n(n+z)} \right\rangle = \left\langle \frac{n-z}{2n} \right\rangle$$

are averages over a single dot. We have assumed both dots to be of equal size, i.e., both nuclear fields have the same effective strength, but are independent, though this has little quantitative effect on the behavior of the system for differences on the order of 10% or less, and no qualitative effect for differences up to 100%. The integral, over a gaussian corresponding to the single-dot nuclear field distribution, is

$$I = \langle \frac{z}{n} \rangle = \frac{1}{[2\pi B_{\rm nuc}^2/3]^{3/2}} \int_{-\infty}^{\infty} dz \int_0^{\infty} r\ dr \int_0^{2\pi} d\theta\ \frac{z\ \exp[-\frac{r^2+(z-B)^2}{2B_{\rm nuc}^2/3}]}{\sqrt{r^2+z^2}}\ . \tag{A.10}$$

After integration over θ, r and variable change, $u = \sqrt{3/2}\frac{z}{B_{\rm nuc}}$,

$$I = e^{-3B^2/2B_{\rm nuc}^2} \int_{-\infty}^{\infty} du\ u\ e^{\sqrt{6}uB/B_{\rm nuc}} {\rm Erfc}(|u|)\ . \tag{A.11}$$

We note that $I \simeq \frac{\langle z \rangle}{\sqrt{\langle n^2 \rangle}} = \frac{|B|}{\sqrt{B_{\rm nuc}^2+B^2}}$ to better than 2% for all external field values, B. Using this approximation, we find the effective decay rates, used in the main text, from the four eigenstates of the (1,1) charge configuration to the (0,2) singlet state to have two forms, one for the $|m_s| = 1$ states ($\mathrm{T}_+, \mathrm{T}_-$), with a rate $\Gamma_{\pm\frac{1}{2},\pm\frac{1}{2}} = \frac{\Gamma_{in}}{4}\frac{B_{\rm nuc}^2}{B_{\rm nuc}^2+B^2}$, and the other for the $|m_s| = 0$ states (T_0, S), with a rate $\Gamma_{\pm\frac{1}{2},\mp\frac{1}{2}} = \frac{\Gamma_{in}}{2}[1 - \frac{B_{\rm nuc}^2}{2(B_{\rm nuc}^2+B^2)}]$.

A.3 Thermal component

In addition to the inelastic decay from the (1,1) singlet to the (0,2) singlet, coupling to the leads allows for a spin-independent transition of either $(1,1) \rightarrow (1,2) \rightarrow (0,2)$ or $(1,1) \rightarrow (0,1) \rightarrow (0,2)$ to occur, breaking blockade and reducing the expected signal. As a thermally activated process, the rate for each should dependend on the energy difference between the (1,1) state and either (1,2) or (0,1). Denoting this detuning

E_T, the corresponding decay has the expected form, $\Gamma_T = \Gamma_0 e^{-E_T/k_B T}$. We note that larger (1,1) to (0,2) detuning E_{SG} corresponds to smaller E_T detuning, as the M point moves closer to the top of the triangle of Fig. 8.4. This functional form is consistent with the observed high detuning behavior shown in Fig. 8.6. Combining this decay with the previous section results, it is convenient to define $\tau_0^{-1} = \Gamma_{in}/4 + \Gamma_T$, the zero-field decay time, and $\tau_B^{-1} = \Gamma_{\pm\frac{1}{2},\pm\frac{1}{2}} + \Gamma_T$, the decay rate of the $|m_s| = 1$ states.

Appendix B

Electronics and wiring

B.1 DC and RF wiring in a dilution fridge

Sample wiring for a dilution fridge requires special techniques and careful attention to balance the often contradictory demands of high electrical conductivity and low thermal conductivity. These often conflict explicitly, because as temperature decreases, the conduction electrons tend to become the dominant carriers of heat. The approach we have used to cool DC signals[1] is long resistive wires, heatsunk through their insulation at many different temperatures by wrapping the wires tightly around a copper spool bolted to a cooling stage of the fridge.[2] We used 3 meter wire looms from Oxford, with 18 constantan wires ($\sim$200 Ω each). The looms we bought had 6 copper wires as well which we did not use, and it was important to cut these between heatsinking stages to avoid transmitting extra heat down the fridge. Below the mixing chamber, the heatsunk resistor idea was implemented more systematically and

---

[1] In practice, DC includes frequencies up to several kHz used by lockin amplifiers.

[2] I secured the wires to the spool with dental floss only. When Oxford does the wiring they also use GE varnish, but this doesn't seem necessary in practice and makes the wiring much harder to reconfigure.

integrated with radiation shielding as described in Ap. C.

Some experiments called for high frequency (up to ∼1 GHz) electrical signals applied directly to gates on the sample. The technique I used for cooling high frequency coax cables without losing bandwidth is just one of many tried first in our group by Leo DiCarlo. Attenuators are inserted at various temperature stages to gradually thermalize the inner conductor, then at the bottom, just before the signal gets to the chip, a DC voltage is added via a bias tee. A bias tee is essentially just a capacitor in the RF line and an inductor in the DC line, such that only signals below the frequency cutoff (∼10 kHz, although this drops when the signal is applied to a high-impedance load like a gate[3]) are passsed from the DC line and only signals above the cutoff are passed from the RF line. Then, because the RF line is already AC coupled, a DC block [4] is inserted at the top of the fridge to explicitly minimize the power dumped into the attenuators. Figure B.1 shows schematically how the DC and RF signals get to the sample.

The attenuator/bias tee technique is suitable only for certain applications. You cannot put very large RF voltages on the sample without the energy dumped in the attenuators exceeding the cooling power of the fridge. You also cannot use this technique to measure a high-frequency response from the sample, because the response is attenuated on the way up just as it is going down. Within these limitations, however,

---

[3] We found that although the bias tee frequency cutoff moved way down when applied to a high-impedance load, the sample had a strange impulse response which partially decreased an applied signal after several hundred μs, which we could only attribute to sloshing of electrons in the 2DEG. For this reason, it is recommended that future samples have as little of the gate over 2DEG as possible, especially for spin experiments where long pulses are crucial.

[4] A DC block is also essentially just a capacitor. Be careful which brand is used to get a low frequency cutoff. The best one we found was from Picosecond Pulse Labs, with a cutoff below 1 kHz.

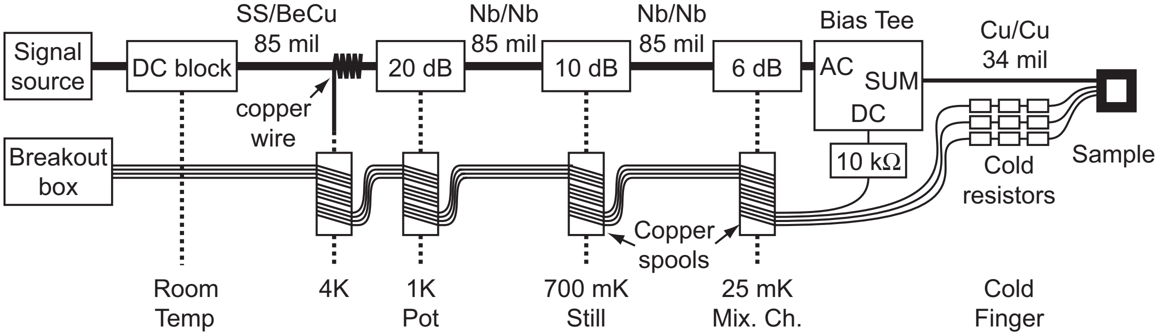

Figure B.1: DC and RF wiring in the Nahum fridge shown schematically. One RF line and 4 DC lines are shown (3 pure DC and one as the DC component of the RF line), although the actual setup had two RF lines and 32 DC lines in two looms (see text). See Ap. C for details of the cold finger design.

this technique provides reasonably cold electrons (~100 mK, twice their temperature with no coax) using robust off-the-shelf components.

Careful consideration should be given to the materials used in the coax. Coax cables follow more or less a square-root-frequency attenuation curve, so even small cable attenuation can change pulse shapes, but this must be balanced with the higher thermal conductivity which normally comes with low attenuation. Above 1K there is a long distance to the port at room temperature, and the 1K pot can handle a lot of heat, so the material of choice for the coax is beryllium-copper (BeCu), with much lower thermal conductivity than pure copper but nearly as good frequency response. Due to limited availability, however, we used coax with stainless steel (SS) outer, BeCu inner. The lines are anchored twice below 1K (at the still and mixing chamber) before passing through the bias tee and ending up at the sample. Below the bias tee we want both thermal conductivity and frequency response to be maximal, so regular Cu/Cu coax is used. There is some question what material is best for the two short segments (1K–still and still–mixing chamber). We used niobium superconducting coax for both on the theory that the superconducting state excludes heat transfer,

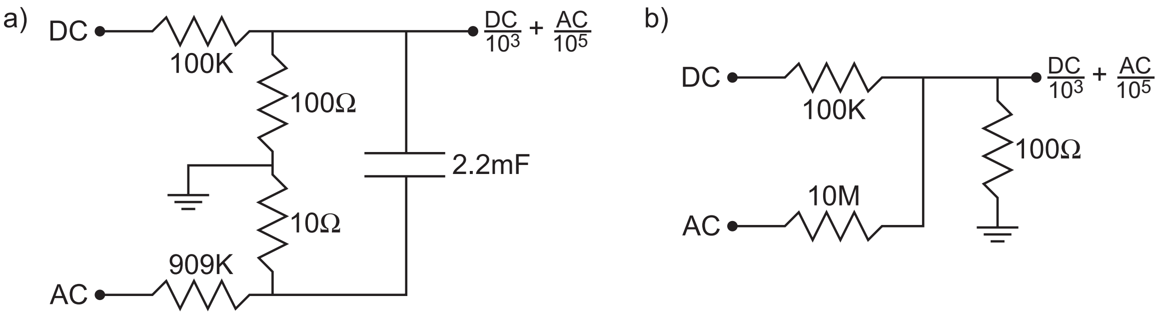

Figure B.2: a) AC+DC box schematic. This circuit divides the DC component by 10^3 and the AC component by 10^5, and adds the below-1-Hz portion of the DC input to the above-1-Hz portion of the AC input. b) Proposed purely resistive adder circuit with no frequency response.

although Leo recently calculated that SS is actually better above ^{3}He temperatures.

The choice of attenuation values is important as well. At 1K, again because the 1K pot is a powerful cooler but also because the temperature difference (300K to 1K) is greatest there (the outer conductor is thermalized at 4K as well, but only attenuation affects the inner), a large attenuation is used at this point. At the still a smaller attenuation is used, but not as small as the temperature difference (1K to 700 mK) would indicate, since the still has much more cooling power than the mixing chamber. Even less attenuation is used at the mixing chamber to balance heating the mixing chamber with heating the sample directly.

B.2 AC+DC box

To measure differential conductance in the presence of a DC bias, we need a DC voltage up to a few mV with an AC oscillation of a few μV added to it. The Agilent 33250 function generator can do this by itself, but it is cheaper and often more convenient to use a DAC channel to generate the DC voltage, and add it with a passive circuit to the oscillating voltage generated by the lockin amplifier, while dividing them both down several orders of magnitude. The circuit I used for this (schematic shown in Fig. B.2(a)) is a slight modification of the one designed by Duncan Stewart [50] but with a lower cutoff frequency so that it needn't be "tuned" to a particular lockin frequency. There has been some discussion (prompted by Amir Yacoby via Jeff Miller) that an even simpler purely resistive circuit (shown in Fig. B.2(b)) can do the same addition with no frequency response and no big capacitor to worry about getting the right kind. The only reason I can think of that one might not want to use this simpler circuit is that the capacitor may be performing useful noise filtering functions: any high-frequency noise in the DC bias is suppressed, including quick steps due to changing the bias, and any DC offset in the oscillating signal is suppressed as well.

B.3 Grounding

Grounding and noise reduction are somewhat of an art. In every experiment I've done there have been different things necessary to minimize noise, and sometimes an absolutely crucial step one time becomes absolutely forbidden the next. Nevertheless, there is one principle that usually leads pretty close to the correct grounding setup: no ground loops. Obviously most every piece of electronics wants some part grounded, and if something that should be grounded is left floating the measurement can go horribly wrong. In addition, it's not always easy to tell if a particular component is grounded. Sometimes there are solid connections between the wall ground, the equipment rack, the chassis, and the shields of front panel connectors, but in many cases these connections are broken, intentionally or not.

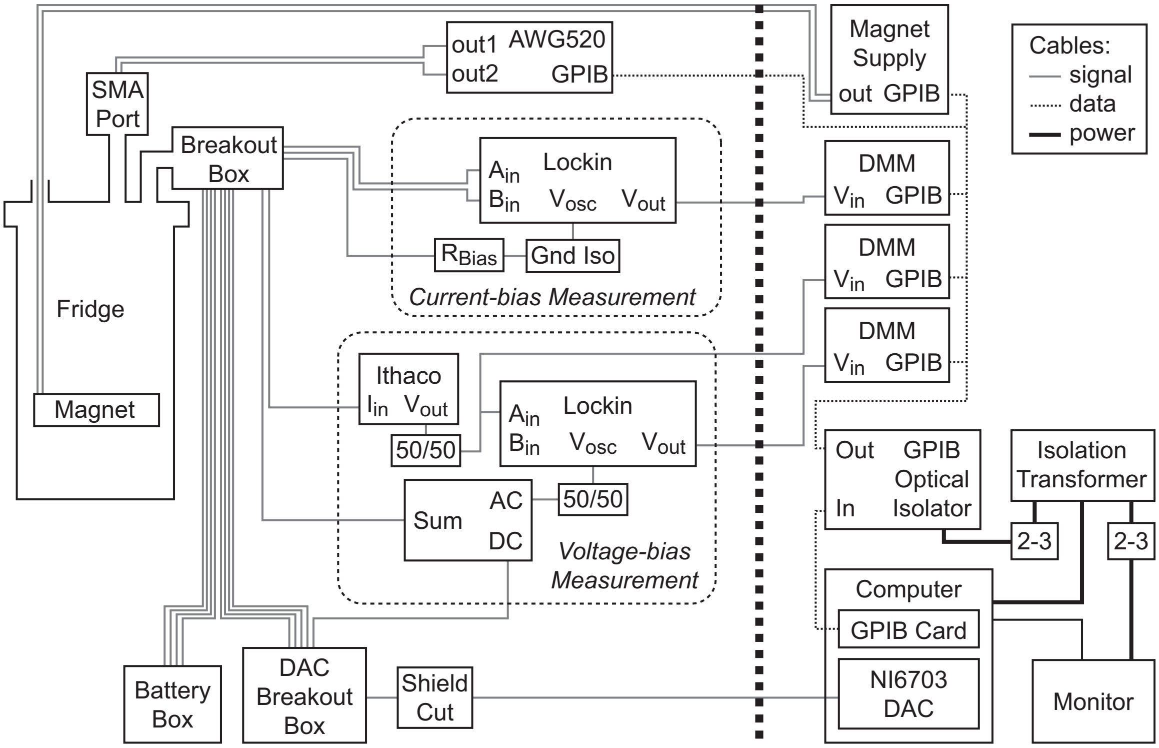

Figure B.3: Full grounding configuration for an experiment, showing all signal and data (GPIB) cables and some power cables. The thick dotted line separates quiet electronics near the fridge from potentially noisy electronics near the computer. Ideally this separation would be a shielded room wall, although in the case of the Nahum fridge it is open space by the doorway, with a cable trace running over the door. Typical current- and voltage-bias measurement setups are shown. The lockin oscillator and Ithaco output shields are partially grounded, so 50/50 (50Ω in both signal and ground lines) or Gnd Iso boxes (ground isolation - pass the inner conductor but completely break the shield) are used on these terminals. The AC+DC box is described in Sec. B.2. The computer is grounded only through the ground wires in the DAC cable, which then passes through the DAC breakout box to the fridge. The shield of this cable is cut, the GPIB signals are run through an optical isolator, and the computer, monitor, and GPIB isolator are powered through an isolation transformer, with 2-3 prong converters inserted to break ground loops within this isolated system. All other electronics are plugged directly into the wall (cabling not shown).

Figure B.3 illustrates the grounding configuration I used for a complete experiment, including the National Instruments 6703 DAC (digital to analog converter) board which resides inside the computer. The Marcus lab has nearly standardized on a DAC built by Jim McArthur in Harvard's electronics shop and designed (at least in its first incarnation) by Jim and Andrew Houck and Jeff Miller. This DAC has excellent noise and grounding properties and is external to the computer so that (at least in its later incarnations) it robustly holds its voltages regardless of what the computer is doing (i.e. crashing). This last benefit notwithstanding, it is possible to use an in-computer DAC with clean results and no ground loops. The trickiest part of this setup, and the hardest problem to diagnose, was that the computer chassis and the DAC board had slightly different ground potentials, with only a small resistance between them, and the difference was a function of how hard the computer's main processor was working. The solution was to completely float the computer, and cut the shield on the DAC cable, which was connected to the computer chassis ground rather than the ground wires in the cable. Another particularly frustrating ground loop may occur due to the magnet power supply, if the magnet leads make electrical contact with the fridge structure, leading to a sample bias which varies with magnet current. Besides careful isolation of the magnet leads inside the fridge, it is important not to let too much water or ice collect at the top of the leads, as this can conduct.

B.4 Divider/adder for NI6703 DAC

The National Instruments 6703 is a 16-bit DAC, but we discovered in testing that with appropriate filtering ($\sim$100 ms time constant) its noise is twenty times smaller than one bit This means that by chaining two channels together we can obtain an effective 20-bit DAC (although the linearity is not good enough to cover the entire range this way—you would use this feature by setting the coarse channel in the middle of the desired range, then sweeping only the fine channel while taking data). This extra resolution didn't end up being necessary for any of the measurements I did, but

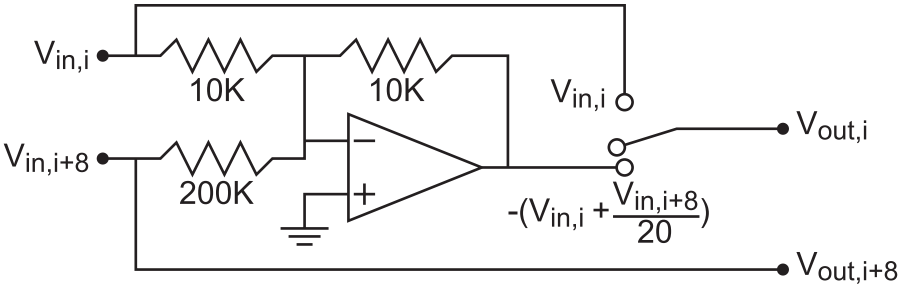

Figure B.4: Divider/adder circuit for use with NI6703 DAC card. This is one of eight identical elements (where i runs from 0–7) on the board in the breakout box for the NI6703 board. Inputs $V_{in,i}$ and $V_{in,i+8}$ come from the SCSI-type connector on the DAC cable, and the outputs $V_{out,i}$ and $V_{out,i+8}$ are BNC connectors on the front panel. The toggle switch between straight-through and linked output modes is also located on the front panel.

I built a box to allow you to, by flipping a switch, change between two independent channels and one composite channel. As the NI6703 has 16 output channels, the first 8 are the coarse channels, the latter 8 are the fine channels, and each pair (chans. 0 and 8, chans 1 and 9, etc.) has a switch to allow linked or independent operation. Jim's electronics shop has all of the software and tools to design and fill a printed circuit board, and Jim is so helpful that this, the first PCB I ever made, worked exactly right and I even felt like I did most of it myself. Figure B.4 shows the circuit diagram for one pair of channels, which was then repeated eight times on the board. The board is mounted inside the DAC breakout box shown in Fig. B.3.

Appendix C

Cold finger design

I joined the Marcus group at a time when the number of cryostats in the lab jumped from two to five: one dilution fridge and one ^{3}He fridge from Stanford were joined by a new dil fridge, a new ^{3}He fridge, and a third dil fridge inherited from the retiring Prof. Nahum. Add to that an old design which would break sample wires with every few thermal cycles, and a push in the lab toward ever more complicated devices with demand for more sample wires (which meant switching from a 28-pin to a 32-pin chip carrier and socket), and it was clear that there was a lot of cold electronics work to be done. Ron and I were tasked with creating a new cold finger design, with the understanding that we would each use one (I was revamping the Nahum dil fridge and Ron the old Stanford dil fridge) and another would replace the rickety cold finger supplied by Oxford in the new ^{3}He fridge. The mechanical design was mostly Ron's work, partly mine, and based on an idea (cold resistors, see below) of Charlie's.

The cold finger serves several purposes. First, it holds the sample in the center of the magnet. Some experiments call for the large field from the solenoid magnet to be perpendicular to the sample plane to affect orbital wavefunctions, while other experiments require a field parallel the sample plane so that field couples almost exclusively to spin. Because of this, we designed two interchangeable mounts for the socket, to be swapped without any wiring or changes to the socket itself. The parallel field mount needs fine control over the sample angle, so that the perpendicular field remaining from an 8–10 Tesla magnet is within the capability of the small (∼250 mT) homemade split coil perpendicular magnet [160] to null out. Experiments in a large perpendicular field are insensitive to small angle changes, so the perpendicular field mount can be much simpler.

The second purpose of the cold finger is to thermally link the sample to the fridge's mixing chamber while shielding it from warmer radiation, and to provide the last stage of cooling for the sample wires. At low temperatures, the wiring is the only thing capable of carrying much heat away from the sample, so cooling the sample and cooling the wires are essentially the same goal. Innumerable techniques have been tried by our group and others over the years for cooling wires without making electrical contact to them. The solution that was in place when I joined the group (and which garnered quite a few entries in the "Don't look in here Charlie" drawer by Ron and Josh trying to reproduce and improve it) was the *metal powder filter*, in which thin, resistive wires are sent through a bath of epoxy loaded with enough copper or other metal powder that it almost conducts (but not quite). The problem with this, besides the fact that it's awfully messy and difficult to work with very thin wires, is the tendency of differential thermal contraction to break these wires occasionally, so that after a few years of regular thermal cycling half of the wires didn't work (or more frustratingly, would work at room temperature but not cold).

What we tried instead, and worked surprisingly well despite its simplicity and robust-

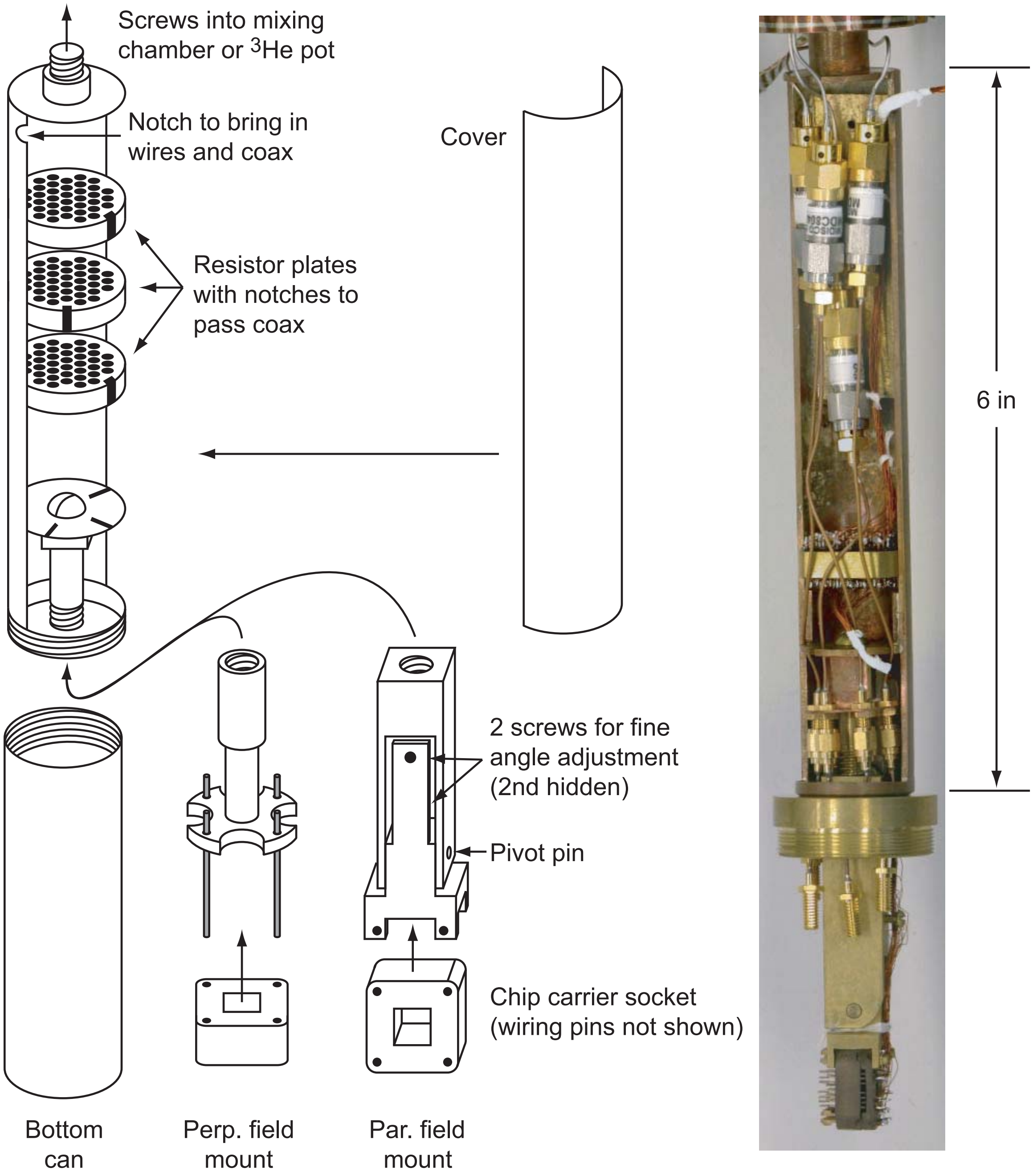

Figure C.1: Schematic and photograph of cold finger. The main structure of the cold finger is copper for optimal thermal conductivity, with a brass cover (removable half cylinder) to minimize eddy current heating. Wires pass through resistors embedded in thick brass plates while the coax (thermalized elsewhere) thread through notches in the plates (offset to block line-of-sight radiation) to get to the sample. The bottom can is brass and shields the sample from warmer radiation outside. Photograph (courtesy of J. B. Miller) shows the cold finger in the ^{3}He system, with coax installed and a thread adapter for a larger bottom can.

ness, was to simply add regular resistors in the lines, anchored tightly into a brass plate which seals the sample space below it from the radiation environment above. In as far as heat is high-frequency noise in the wire, the resistors along with their stray capacitance RC-filter this noise out. In the dilution fridges we used three of these brass plates in series, in the ^{3}He fridge just one. The resistor values we chose to be 100 Ω per plate in half of the lines (to be used for ohmics) and 5 kΩ per plate in the other half (to be used for gates). Below the plates, the radiation environment is sealed by a screw-on brass can. With this setup in the Nahum fridge, we measured electron temperature $\sim$45 mK at a base temperature of $\sim$25 mK.

Fig. C.1 shows some schematics of the design and a photograph of cold finger in use on the ^{3}He system with the cover and can removed. Since making the original cold finger, a larger bottom can has also been made to accomodate extra coax cables to the sample, and the adapter needed to thread on the larger bottom can is shown in the photograph.

Appendix D

Igor routines

For experiments, the Marcus lab runs almost exclusively Igor Pro, a superb data acquisition, analysis, and graphics platform[1], with its own built-in programming language. Perhaps the only concrete result of the first few experiments I did (Aharonov-Bohm rings and Coulomb drag, neither of which yielded anything I deemed worth putting in this thesis) is a set of higher-level Igor routines to make data acquisition easier and to automate some common analysis functions.

The idea was to make a generic data acquisition routine: there are lots of parameters to change in an experiment, but at any given time you will be sweeping one or two of them, measuring one or more quantities, and plotting the results. When I started, there was a different routine for each combination of parameters to sweep and the data to be measured was hard coded. Making simple changes required changing many routines, and doing even a slightly more complicated type of data acquisition would take completely new code. I'm not sure if I really reduced my own coding time (It took me quite a bit of time to develop this code!) but I do think these routines made

---

[1] Igor is produced by WaveMetrics (http://www.wavemetrics.com/)

it much easier to try new ways of taking data, which became invaluable as we started pulsing (and varying all of the pulse heights and times) and charge sensing (measuring up to four signals simultaneously).

The routines revolve around two generic acquisition routines, `do1d` for single-parameter sweeps, and `do2d` for two-parameter sweeps (although over the years several variations have been added for specialized applications, such as averaged or interlaced two-parameter sweeps to reduce noise). These functions take a string input for each sweep parameter which is then fed to a routine, `setval`, which contains all of the code to interface to the instruments to set physical parameters (gate voltages, field, pulse waveforms, etc.). In addition, global variables set by a graphical interface panel describe what is being measured by which DMMs (digital multimeters), and this information is fed to the routine `getdata`, which polls the dmms and calculates the data values to store.

A second advantage of using string inputs for the swept parameters and data types is that it allows the program to automatically name the new data waves[2] in such a way that the user can read off what was measured and what was swept. Analysis routines can also parse the name for this information (via the routine `getlabel`), allowing them to automate tasks like labeling axes and color scales. Finally, each wave name gets a serial number appended to distinguish it from other waves of the same type. If several data streams are measured simultaneously, they all get the same serial number, as do any derivative waves (slices, averages, differentiations, etc.) generated by analysis routines. A complete wave name might look something like `condbc5_ 212`,

---

[2] "Wave" is Igor's name for an array of data (1–4 dimensions) with a bit of extra scaling and other information tacked on.

which means conductance measured with field as the outer loop and DAC channel 5 as the inner loop, with a serial number of 212.

One final important aspect of my routines is automatic logging. At the beginning of every sweep, `do1d` and `do2d` save all of the system parameters that they have access to into a text file for later reference (although if I were doing this again today I might save this info in the `wavenote` for each data wave). In the lab book then, I would write just the serial number and notes about what appeared in the data, but not what was measured or swept or what the other system parameters were during the sweep—a significant time savings and incredibly useful weeks or months later when you want to repeat a particular measurement or know everything about it for analysis.

My routines evolved over time into five files with lots of cross references such that you needed all five to do anything. This got unnecessarily confusing and cumbersome, so as I was writing this I condensed the routines into two files (and cleaned up the code a bit while I was at it). `alexanalysis.ipf` has wave management, analysis, and image processing routines, and it can stand on its own for data analysis uses. `alexdata.ipf`, has the core data acquisition routines, and must be used along with `alexanalysis.ipf` as well as with the driver files for any instruments you intend to use.[3] Copies of these `alexanalysis.ipf` and `alexdata.ipf` should be available on the Marcus group website (marcuslab.harvard.edu) under "member information."

To illustrate the ideas above, on the following pages I've included `do1d` (but not the nearly identical `do2d`), `getdata`, `setval`, and `getlabel`. Finally, I've included two

---

[3] In particular, in order to use the `gotolocal` feature in `alexdata.ipf`, you need my version of DMM procedures, `alexDMM procedures.ipf`. This sends the DMMs to local mode (continuously displaying measurements) when not in a sweep, but keeps them in remote mode (so they go faster and don't flash a lot) during sweeps.

functions to fix an annoying aspect of exporting EPS files from Igor, from the file `alexepsfix.ipf`.

```
//do1d: generalized 1D sweep - figures out from idstr what to sweep
function do1d(idstr,start,stop,numdivs,delay)
   string idstr      // see setval for allowed idstr’s
   variable start    // starting value
   variable stop     // ending value
   variable numdivs  // number of points minus 1
   variable delay    // seconds of delay between points

   variable numpts=numdivs+1,nw=nextwave()
   string/G S_datatype1,S_datatype2,S_datatype3,S_datatype4
   string wave1,wave2,wave3,wave4
   variable d1=0,d2=0,d3=0,d4=0 // flags (0 or 1) for if data streams are in use
   variable/G V_rampbackflag   // flag(0 or 1) for whether to ramp back to
                               // initial values at the end of the sweep

   // make, name, scale, and display the data waves
   if(!stringmatch(S_datatype1,"-"))
      sprintf wave1,"%s%s_%d",S_datatype1,idstr,nw
      make/o/n=(numpts) $wave1=NaN;wave w1=$wave1
      setscale/i x start,stop,"",w1
      showwaves(wave1);movewindow/I 0,0,3,2.5
      d1=1
   else  // need something in wave1 for logwave
      sprintf wave1,"???%s_%d",idstr,nw
   endif
   if(!stringmatch(S_datatype2,"-"))
      sprintf wave2,"%s%s_%d",S_datatype2,idstr,nw
      make/o/n=(numpts) $wave2=NaN;wave w2=$wave2
      setscale/i x start,stop,"",w2
      showwaves(wave2);movewindow/I 3,0,6,2.5
      d2=1
   endif
   if(!stringmatch(S_datatype3,"-"))
      sprintf wave3,"%s%s_%d",S_datatype3,idstr,nw
      make/o/n=(numpts) $wave3=NaN;wave w3=$wave3
      setscale/i x start,stop,"",w3
      showwaves(wave3);movewindow/I 0,3,3,5.5
      d3=1
   endif
   if(!stringmatch(S_datatype4,"-"))
      sprintf wave4,"%s%s_%d",S_datatype4,idstr,nw
      make/o/n=(numpts) $wave4=NaN;wave w4=$wave4
      setscale/i x start,stop,"",w4
      showwaves(wave4);movewindow/I 3,3,6,5.5
      d4=1
   endif

   logwave(wave1)   //save conditions of sweep to a text file
```

```
   nolocal()   //prevent DMMs from returning to local mode after each reading
               //function is in "alexDMM Procedures.ipf"
   variable t1=ticks,t2,secs,i=0

   // data taking loop
   make/o/n=(numpts) gate;gate[]=start+p*(stop-start)/numdivs
   setval(idstr,gate[0]);wait(3*delay)
   variable/G V_gtrip=0 // reset the abort sequence for I-bias measurements
   do
      setval(idstr,gate[i]);wait(delay)
      if(d1)
         w1[i]=getdata(1)  //get new data into the appropriate waves
      endif
      if(d2)
         w2[i]=getdata(2)
      endif
      if(d3)
         w3[i]=getdata(3)
      endif
      if(d4)
         w4[i]=getdata(4)
      endif
      i+=1;doupdate
      // fix the scaling if time is the axis
      if(stringmatch(idstr,"time")||stringmatch(idstr,"noise"))
         t2=ticks;secs=(t2-t1)/(60.15*i)
         if(d1)
            setscale/p x,0,secs,w1
         endif
         if(d2)
            setscale/p x,0,secs,w2
         endif
         if(d3)
            setscale/p x,0,secs,w3
         endif
         if(d4)
            setscale/p x,0,secs,w4
         endif
      endif
   while((i<numpts)&&(V_gtrip==0))
   if(V_rampbackflag==1)  //check whether to ramp back to start
      setval(idstr,gate[0])
   endif
   endsweep(t1)  //cleanup shared by do1d,do2d
end

//getdata: take a point in one data stream
function getdata(stream)
   variable stream  //from datatypes panel
   SVAR datatype=$("S_datatype"+num2istr(stream))
   NVAR dmm=$("V_dmm"+num2istr(stream)), gtype=$("V_gtype"+num2istr(stream))
   variable g,i,v,Lsens,Isens,Rinline,ZeroOffset,Vapp,Rbias,DCgain, R0=25812.8
   variable/G V_hpampsum     // AC amplitude of HP33250 pair
   variable/G V_gtrip        // indicator for too low a conductance
```

```
   variable/G V_limitgflag   // check for too low conductance?
   variable/G V_glimit       // limit to check against

   if(stringmatch(datatype[0],"g")||(stringmatch(datatype[0,3],"cond")))
      if(gtype==1)  // 1=V-bias, lockin source
         Lsens=2e-3
         Vapp=6e-6
         Rinline=4.49e4
         Isens=1e-9
         ZeroOffset=0
         i=Isens*Lsens*(readdmm(dmm)-ZeroOffset)/10000
         g= R0/((Vapp/i)-Rinline)
      elseif(gtype==2)  // 2=V-bias using HP33250 as source
         Lsens=100e-3
         Rinline=20000
         Isens=1e-9
         ZeroOffset=0
         i=Isens*Lsens*(readdmm(dmm)-ZeroOffset)/10000
         g= R0/((V_hpampsum/(1e6*i))-Rinline)
      elseif(gtype==3)  // 3=V-bias, reading a resistor voltage, HP source
         Lsens=5e-4
         Rbias=1e3
         ZeroOffset=0
         v=Lsens*(readdmm(dmm)-ZeroOffset)/10000
         g= R0/(((V_hpampsum/(1000*v))-1)*Rbias-Rinline)
      elseif(gtype==4)  // 4=I-bias using lockin as source
         Lsens=50e-6
         Vapp=1e-1
         Rbias=1e8
         ZeroOffset=0
         v=Lsens*(readdmm(dmm)-ZeroOffset)/10000
         g=(R0/Rbias)*((Vapp/v)-1)
      elseif(gtype==5)  // 5=I-bias using HP33250
         Lsens=100e-6
         Rbias=10e6
         ZeroOffset=0
         v=Lsens*(readdmm(dmm)-ZeroOffset)/10000
         g=(R0/Rbias)*((V_hpampsum/342/(1e3*v))-1)
      endif
      if((V_limitgflag)&&(g<V_glimit)) //stop on low conductance?
         V_gtrip=1
      endif
      return g
   elseif(stringmatch(datatype[0],"v")) // voltage
      Lsens=10e-6
      ZeroOffset=0
      return Lsens*(readdmm(dmm)-ZeroOffset)/10000
   elseif(stringmatch(datatype[0],"i")) // current
      DCgain=1e11
      ZeroOffset=0
      v= (readdmm(dmm)-ZeroOffset)/(DCgain*1000)
      return v
   endif
end
```

```
//setval: generic routine to set physical parameters
function setval(idstr,value)
   string idstr
   variable value
   if(stringmatch(idstr[0],"c"))
      variable num=str2num(idstr[1,2])
      chanramp(num,value)
   elseif(stringmatch(idstr,"bx"))
      ramp3axis(1,value)
      wait(52)
   elseif(stringmatch(idstr,"by"))
      ramp3axis(2,value)
      wait(52)
   elseif(stringmatch(idstr,"bz"))
      ramp3axis(3,value)
      wait(52)
   elseif(stringmatch(idstr,"time")||stringmatch(idstr,"noise"))
      wait(0)
   elseif(stringmatch(idstr,"diag"))
      //diagonal "detuning" sweep of left and right walls
      variable/G diag_offset,diag_slope
      setval("right",value)
      setval("left",diag_offset+diag_slope*value)
   elseif(stringmatch(idstr,"left"))
      //change the left wall (c6) while updating left listener (c7)
      //to keep conductance in range
      variable/G c7offset,c7slope,leftcenter
      setval("c6",value)
      setval("c7",c7offset-c7slope*(value-leftcenter))
   elseif(stringmatch(idstr,"right"))
      //same with left wall
      variable/G c1offset,c1slope,rightcenter
      setval("c2",value)
      setval("c1",c1offset-c1slope*(value-rightcenter))
   else
      print "ABORTING - couldn’t resolve idstr"
      return 0
   endif
end

//getlabel: returns the label for to the given axis from a wave name string.
// also fills S_namesegment#, where # is the axis, with its idstr
// FOR NEW PARAMETERS: ADD HERE AND IN SETVAL
function/S getlabel(wavestr,axis)
   string wavestr
   variable axis //0 is data, 1 is x, 2 is y, 3 is z
   string labelstr,cropstr=wavestr,idstr
   variable nextpos,paramnum
   //make the wave "datalabels" and populate using addtext
   //for each sweep parameter or measurement type add a line here of the form:
   //     addtext(dl,"<idstr>;<label text>")
   //if a shorter name could conflict with a longer one (eg. "b" and "bx") put
   //the longer one first, otherwise I’ve used alphabetical order for clarity.
```

```
//See help on Label for escape codes
// note that "\\" gives "\" in the actual string
make/T/o/n=0 $"datalabels"=""
wave/T dl=$"datalabels"
addtext(dl,"bx;X Magnetic Field (\\umT)")
addtext(dl,"by;Y Magnetic Field (\\umT)")
addtext(dl,"bz;Z Magnetic Field (\\umT)")
addtext(dl,"bmt;Measured Field (\\umT)")
addtext(dl,"b;Magnetic Field (\\umT)")
addtext(dl,"cond;g (\\ue\\S2\\M/h)")
addtext(dl,"color;")
addtext(dl,"c;") //this one is special-see below
addtext(dl,"data;Data point")
addtext(dl,"dif_cond;\\u#2conductance derivative (a.u.)")
addtext(dl,"dif_res_cond;\\u#2conductance derivative (a.u.)")
addtext(dl,"diag;Diagonal parameter (\\umV)")
addtext(dl,"freq;Frequency (\\uHz)")
addtext(dl,"g;g (\\ue\\S2\\M/h)")
addtext(dl,"i;Current (\\uA)")
addtext(dl,"noise;Time (\\usec)")
addtext(dl,"norm;Normalized Signal")
addtext(dl,"par;Parallel Field (\\umT)")
addtext(dl,"perp;Perpendicular Field (\\umT)")
addtext(dl,"phase;Phase (\\uRadians)")
addtext(dl,"Res_cond;delta g(\\ue\\S2\\M/h)")
addtext(dl,"time;Time (\\usec)")
addtext(dl,"t1;First pulse time (\\uns)")
addtext(dl,"t2;Second pulse delay (\\uns)")
addtext(dl,"t3;Second pulse time (\\uns)")
addtext(dl,"vdc;Calculated DC voltage (\\uV)")
addtext(dl,"v;Voltage (\\uV)")

variable i=0,j
do //loop through axes
   nextpos=0
   j=0
   do //loop through ids and labels in the text wave "datalabels"
      if(j==numpnts(dl)) //quit if no match was found
         return ""
      endif
      idstr=stringfromlist(0,dl[j],";")
      //does the next id match dl[j]?
      if(stringmatch(cropstr[0,strlen(idstr)-1],idstr))
         //is there a number assoc. with this id?
         paramnum=str2num(cropstr[strlen(idstr),30])
         nextpos=strlen(idstr)+(numtype(paramnum) ? 0 :
                              strlen(num2istr(paramnum)))
         if(stringmatch(idstr,"c")) //DAC chans are special
            labelstr="Chan " + num2istr(paramnum) + " (mV)"
            if(waveexists($"DAClabel"))
               wave/T cnames=$"DAClabel";labelstr+=" - "+cnames[paramnum]
            endif
         else  //For other ids, take the label from "datalabels"
            labelstr=stringfromlist(1,dl[j],";")
```

```
            endif
         endif
         j+=1
      while(nextpos==0)
      SVAR ns=$("S_namesegment"+num2istr(i))
      if(SVAR_exists(ns))
         ns=cropstr[0,nextpos-1]
      endif
      cropstr=cropstr[nextpos,30] //move on to the next section of the name
      i+=1
   while(i<=axis)
   return labelstr
end



//alexepsfix.ipf   Alex Johnson  2004
// This  is my way of making high-quality, compact eps files from Igor
// When Igor exports an image plot as eps, it makes the interior of the image
// be a single object (good) but all pixels at the edges, no matter what you do,
// are drawn as rectangles.  This has several bad consequences:
//  1. big files
//  2. they don't always draw in the same places as the other pixels
//  3. they don't always get the same colors as the other pixels
// Igor also draws the entire color scale as rectangles, with the same
// annoying results
// To fix, first run "fixgraphedges" for each graph to be exported, then
// export the layout as a color eps, then run "removerects" and select the
// exported file.  Finally, open the "..._out.eps" file in Illustrator and
// insert the appropriate color scale file (which, if you don't have it, you can
// make by exporting one as a TIFF or similar, cropping to just the colorbar
// and resizing to 256 wide by 1 pixel high).

//fixgraphedges: rounds axes so that Igor will make small rectangles around the
// edges which will wind up under the axes so they can be thrown away
function fixgraphedges(overagex,overagey)
   variable overagex,overagey  //fraction of a pixel to make the overage
   wave w=$topimage(0)
   variable x0=dimoffset(w,0),dx=abs(dimdelta(w,0))
   variable y0=dimoffset(w,1),dy=abs(dimdelta(w,1))
   variable V_min,V_max
   getaxis/Q bottom; variable xmin=V_min,xmax=V_max
   getaxis/Q left; variable ymin=V_min,ymax=V_max

   if(xmax<xmin)  //to account for reversed axes
      overagex*=-1
   endif
   if(ymax<ymin)
      overagey*=-1
   endif
   xmax=(round((xmax-x0)/dx-(overagex+.5))+(overagex+.5))*dx+x0
   xmin=(round((xmin-x0)/dx+(overagex+.5))-(overagex+.5))*dx+x0
   ymax=(round((ymax-y0)/dy-(overagey+.5))+(overagey+.5))*dy+y0
   ymin=(round((ymin-y0)/dy+(overagey+.5))-(overagey+.5))*dy+y0
```

```
   setaxis bottom,xmin,xmax
   setaxis left,ymin,ymax
end

//removerects: takes an EPS file saved by Igor and removes the little rectangles
// made by fixgraphedges, saving the result in a new file with "_out" appended
function removerects()
   variable refnumin,refnumout
   string S_filename,filenameout,instr
   variable V_filepos,V_logEOF
   open/R/T=".eps"/M="Select EPS file to fix" refnumin
   if(refnumin==0)  //quit if no file selected
      return 0
   endif
   filenameout=stringfromlist(0,S_filename,".")+"_out.eps"
   open refnumout as filenameout
   string nrstr="NewRectImageLine"+num2char(13),cxstr="cx"+num2char(13)
   do
      //read a line from the input file (terminator CR)
      freadline/T=(num2char(13)) refnumin,instr
      //include in output only if it doesn't contain "NewRectImageLine" or "cx"
      if((strsearch(instr,nrstr,0)<5)&&(strsearch(instr,cxstr,0)<0))
         fprintf refnumout,"%s",instr  //spit it back out if it's OK
      endif
      fstatus refnumin
   while(V_filepos<V_logEOF)
   close refnumin; close refnumout
end
```

Appendix E

Measurement techniques

This appendix describes some techniques I use for efficient device measurement. I was expecting to also include here some more detailed information about fabrication of my devices (which I spent at least an integrated year on), but essentially everything I did can be found in older Marcus group theses [1, 161] and in fact the group has significantly moved on already since I stopped doing fab.[1] What remains for this appendix are two parts: the sequence of events (tests and cooling steps) I use to safely cool a device while learning as early as possible if there is a problem, and ways I've used "wall control," a slightly outdated term for adjusting gates automatically for quicker movements around parameter space.

E.1 Cooling and diagnostics

While the fridge is still warm, you can check everything about the fridge wiring (except whether there are shorts/opens that occur only cold) and quite a bit about

---

[1] See the group website (http://marcuslab.harvard.edu/) under "member information".

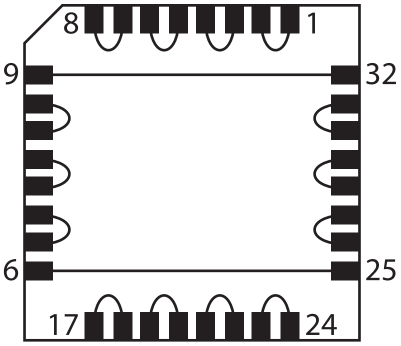

Figure E.1: Chip carrier for testing fridge wiring. Solid rectangles are bond pads, and the curves and lines represent bond wires connecting them. When inserted as usual, this connects 1–2, 3–4, etc., but when turned 90°, it connects all different pairs (1–24, 2–3, etc.).

the device. First, while the device is still safe in its antistatic case, check the fridge wiring. The easiest way to do this is to have a chip carrier bonded pad-to-pad in a pattern that links different gates depending on the insertion orientation. The one I made has bonds as shown in Fig. E.1. Insert this carrier in the normal orientation. Ground all gates on the breakout box (At this stage it is often easiest to take off all grounding caps and ground the gates only with the switches. Do NOT do this when the device is inserted, because inadvertent switch flipping could blow up a gate.

Attach a multimeter in resistance mode from line 1 to ground by attaching a BNC-to-banana connector to the multimeter, and plug this into line 1 with a BNC cable. Then float line 1. The ohmmeter should read roughly the inline resistance of line 1 plus that of line 2 (or whichever line 1 is paired with). If it shows overload, one of these lines is broken. Now float line 2, and the ohmmeter should overload. If there is any finite resistance showing, one of these lines is shorted to another line or to ground. Repeat this procedure with each pair of gates. If there are no problems, the sample lines are fine.[2] If you found a problem, repeat those gates after turning the

---

[2] There's still the possibility that lines 1 and 2, for example, are shorted together, so a truly complete check would involve doing this again with the carrier turned 90°

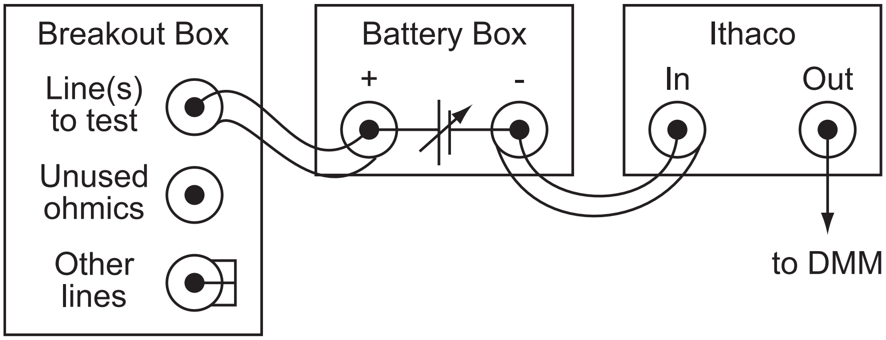

Figure E.2: Gate/ohmic test circuit. The Ithaco current meter input is connected to the negative side of the battery, and the positive side of the battery is connected to the gates or ohmics to be tested. These terminals may be reversed to test current at the opposite bias. Some ohmics may be floated during ohmic tests, while all other gates and the return-path ohmics should be grounded to prevent shocks.

carrier 90° to isolate the broken or shorted line.

E.1.1 Room-temperature sample tests

Once the fridge lines are working you can insert the sample. The sample is more sensitive to shocks when cold than warm, because there is more leakage in a warm sample, but it can still very easily be destroyed, so be sure to ground yourself well to the fridge (and ground all sample lines) while inserting the sample. All initial tests should use voltage bias so that a potential open circuit won't generate huge voltages, and you should turn the voltage slowly up from zero while watching the current, so that a potential short circuit won't generate huge currents. At room temperature, the exact resistances or I/V characteristics are unimportant, what matters is their order of magnitude, so I use a simple battery/current meter circuit as shown in Fig. E.2 for all room-temperature tests. In this circuit, current flows from the device, through the battery, to the current meter, and back again through the BNC shields and shells

---

anyway.

of the battery box and breakout box to the low-voltage side of the device.

First test the ohmics. With all gates grounded, attach the circuit of Fig. E.2 to one ohmic at a time with all other ohmics grounded. Slowly turn the battery up to several mV (1–2 hundredths on the dial), watching the current. Ohmic resistances should be in the neighborhood of 10 kΩ or less at room temperature. If these resistances are in the MΩ range, they are likely not to work at all at low temperature, but in the kΩ range, room-temperature resistance may not be correlated with low-temperature resistance, so it is not worthwhile to measure the pairwise resistances at this point. If the resistance is in the GΩ range, the bond wire likely popped off or the chip carrier is not sitting well in its socket. Note that the large, many-channel battery boxes typically have about 100 kΩ output impedances whereas some of the individual battery boxes have vanishing output impedance at low voltage, and the Ithaco on 10^{-9} A/V sensitivity has ∼4 kΩ input impedance.[3] The impedance of the measurement circuit should be determined and taken into account when measuring resistances in the kΩ range by this method.

Next, test the gates for leakage, which will also tell you whether the bond wires are connected and if any gates are shorted together. With everything grounded, including the gate to be tested (remove its grounding cap but keep the switch grounded), turn the battery to zero and attach it to the gate. You should see the measured current jump from essentially zero (when it was measuring an open BNC) to somewhere around the high pA to nA range (depending on the measurement impedance) just

---

[3] The manual says 20 kΩ, but the ones I've measured appear to all have only 4 kΩ. The difference persists at other scales:

Sensitivity (A/V)	10^{-11}	10^{-10}	10^{-9}	10^{-8}	10^{-7}	10^{-6}
Listed R (Ω)	2M	200k	20k	2k	200	20
Measured R (Ω)	390k	42k	4.3k	420	81	<10

based on the small residual voltage from the battery, which serves as a confirmation that the circuit is properly attached and it is safe to unground the gate. Do so, and you should see the current drop to near the "zero" value it had open. A current of a few pA or less remaining is normal, this is photocurrent in the device. You can see this by covering the sample with your hand or with the cold finger can, and the current will change. Now slowly turn the battery up, watching the current. I usually go to 300 mV (one turn, either positive or negative will do) and stop if the current goes above 10 nA (10 V with the Ithaco on 10^{-9}) although occasionally the leakage will be up to $\sim$100 nA in the light. Photoconductivity is an even bigger effect than photocurrent in these devices, and at room temperature in the dark a good gate should not have more than a few nA leakage current at 300 mV. Also note that if you are testing a gate connected through a bias tee, it has a large capacitance to fill through an inductor and a resistor, so it has big transient currents on a timescale of about a second, and you must proceed slowly, waiting for the transients to settle to see that the DC current is safe.

If any gate leaks much more than a few nA, it may have a short. If more than one gate leaks and they are nearby, they may be shorted together. A safe way to test this is to measure the leakage through one of them while grounding the others through large resistors (1–10 GΩ, bigger than the leakage resistance). If the leakage is gate-to-gate, it will drop substantially when doing this. The problem may be a conducting residue or contaminant on the chip, in which case you can clean it and try again (we have had cases of conducting methanol, for example), or it may be a lithographic error, in which case either you can live with those gates always having the same voltage or the device is trash. This is the end of what you can do at room temperature, so if you have gotten this far with no problems, you are ready to cool.

E.1.2 Cooling with positive bias

The practice of cooling with a positive voltage on the gates, which may have started in the Marcus group but is now used widely, recently moved beyond the realm of mythology. Andy Sachrajda's group did a systematic study (although I don't believe this has been published) of switching noise in the conductance of one particular QPC, and found a clear minimum around +250 mV with more noise on either side. Anecdotal evidence in our group suggests that each heterostructure has its own preferred cooling voltage, and we have typically used anywhere from 250–400 mV. To do this, leave all of the ohmics grounded and while their grounding caps are still on, flip all of the gates to bus. Remove one grounding cap and attach the same battery/Ithaco circuit (making sure you attach it by a long enough BNC cable that you can still get the fridge into the dewar), then remove the grounding caps from all of the other gates. Now slowly turn up the voltage to the desired value, watching the current to see that it's roughly the sum of all of the individual gate leakages (in the dark, assuming you have the IVC closed). Now you can start cooling, and the leakage current should drop sharply,[4] but keep the positive bias on until you reach 4 K.

---

[4] Ron claims he saw the sample cool just due to gas expansion upon pumping out the IVC this way.

E.1.3 Low-temperature sample tests

By the time you get to 4 K, leakage at +300 mV should be below 1 nA and negative-bias leakage should be immeasurably small up to several volts. Unless you are using an exotic heterostructure, there should be no reason to test how far you can go in negative bias as long as the positive-bias leakage is small. If you do push the gates all the way to negative-bias leakage, you may make the device noisy again. You can now take off the positive bias, test the ohmics individually, and test gate action. At this point the actual numbers are useful and are unlikely to change as you cool further (although I have heard of cases where ohmics work at 4 K but not at 50 mK) so it is worthwhile setting up a lockin measurement. The following diagnostics can be done in parallel with cooling the fridge from 4 K to base. Again, voltage bias is safer for diagnostics, and the usual configuration is to take the lockin oscillator through a big divider (usually 10^5:1) to one ohmic and out another to the Ithaco, with all other ohmics floated. You can do this from one ohmic to each other ohmic to make sure the mesa conducts and all of the ohmics basically work, then test individual ohmic pairs on your current paths. Finally, this same measurement configuration can be used to test gate action by applying negative voltages to a pair of gates which should constrict the current path being measured. Slowly turn up the (negative) voltage on one gate, and you should see a small drop in the conductance when it depletes the 2DEG underneath it. You should see a bigger drop in conductance when the second gate depletes and current is forced to go through the channel between the two gates. Depletion should occur around -200–300 mV, and can be used to test gates that are too far away from each other to pinch off completely. for QPCs, continue turning the two gates up uniformly and conductance should drop to zero at anywhere from -500 mV to -2500 mV, depending on the design and the 2DEG depth and density. When it does, you should be able to push the channel back and forth by pulling back on one gate until conduction turns back on, then pushing on the other gate to turn it back off again. This is the real signature that the QPC gates are working correctly, and you can check that nearby plungers have an effect on conductance as well. At this point, if you STILL haven't encountered any problems, you are ready to put the gates on DACs, armed with estimates of where pinch-off points are based on the above tests.

E.2 Wall control

Wall control is a slightly anachronistic name the group uses to describe correcting for the cross-coupling between gates. The technique was originally used to adjust the walls (the gates next to the QPCs of a dot) to keep a constant number of channels open in the QPCs while the plungers (the little gates far from the QPCs) were swept over a wide range to distort the shape and size of the dot. I've done several different analogous operations to keep devices at the appropriate operating points, which I will describe here in order of increasing complexity.

E.2.1 Linear charge sensor control

The experiments in Chs. 7–9 all used devices where the optimal way to control the dot electrons was to sweep a gate that also directly affected the charge sensor (gate 2 or 6 in Fig. 7.1) and therefore a sweep of any reasonable size would push the charge sensor out of its high-sensitivity region. We corrected for this by changing the other gate defining the charge sensor QPC (gate 1 or 7) in the opposite direction, for example: $c_1 = c_1^0 - slope(c_2 - c_2^0)$. This was built into the sweep parameter (see "left" in the routine `setval`, Ap. D) so that whenever c_2 was changed, c_1 would change as well. The offset c_2^0 is taken to be the value of gate 2 at the most interesting point in the sweep, and c_1^0 is determined by sweeping just c_1 at this point and finding the optimal sensor operating point, usually by picking a conductance value, say 0.3 e^2/h. Lastly, *slope* is determined by changing c_2 either direction as far as you would want to sweep it and taking new c_1 sweeps to see how far the optimal operating point moved.

E.2.2 Automatic charge sensing

From time to time the charge sensor will change its conductance, so that what was the optimal sensing point at the beginning of a long sweep may no longer be sensitive at the end. In addition, changes in other gates can have an effect on the charge sensor as well, but these effects may be nonlinear, or dependent on the values of other gates, and in any event it would be time-consuming to explicitly correct for all extra gates. As long as these gates are not being changed within a single data sweep (or even if they are, so long as they aren't the inner loop) we can automatically adjust the sensor by running a feedback routine between sweeps which changes the sensor setpoint while measuring its conductance until this conductance is optimized. This can work within the linear charge sensor control framework described above by simply setting c_2^0 to the value of c_2 when the routine is run, and setting c_1^0 to the value of c_1 when the routine terminates. With a routine like this, it is important to build in error checking so that the feedback routine doesn't run away to high positive or negative gate voltages.

E.2.3 Honeycomb centering

In double quantum dots, one often wants to pick a honeycomb vertex pair and optimize its characteristics by changing the three tunnel barriers bounding the dots. This was particularly important in the few-electron dots of Chs. 7–9, because the majority of data could only be taken at the (1,1)–(0,2) triple-point pair. With such small dots, the strengths of tunnel barriers are not determined simply by a linear combination of all gates, so wall control as originally envisioned is not possible. However, it turns out that the position of the vertices is, to a good approximation, simply a linear combination of all gate voltages, and we made use of that feature to automatically center the vertices in two-dimensional sweeps (c_2 and c_6) as the other gates (c_3, c_4, c_5 and c_{12}) are adjusted. By measuring the vertex locations at several values of each of these gates, we can assemble equations of the form

$$c_2^{center} = c_2^0 - K_{23}(c_3 - c_3^0) - K_{24}(c_4 - c_4^0) - \dots$$

and

$$c_6^{center} = c_6^0 - K_{63}(c_3 - c_3^0) - K_{64}(c_4 - c_4^0) - \dots$$

and it is a simple matter to programmatically center the sweeps at these locations for any given values of the extra gates.

E.2.4 Matrix wall control

The device from Ch. 4 and other medium-sized but complicated devices are amenable to a full “exact diagonalization” wall control (to borrow a term that makes the technique sound more fancy than it is). In this device (see Fig. 4.1) I had five physical parameters I cared about (although this was not necessary for the Fano experiment described here, only for the ill-fated Coulomb drag experiment which followed it): the upper left barrier, the lower left barrier, the dot-channel barrier, the channel conductance, and a plunger. Each parameter had one gate which was primarily responsible for controlling it, but these gates all affected all of the other parameters as well. In order to make any sense of this I had to measure all of the cross couplings, put them into a matrix, and invert the matrix so that I could tell the program what to make each parameter and it would calculate all of the gate values.

The first step is to define the physical parameters in terms of the primary control gate. For example, a QPC barrier parameter could be defined as "mV of gate 1 from a conductance of 0.5 e^2/h."[5] Then take a number of sweeps of gate 1 at various values of gate 2 and measure how far the center point (i.e. 0.5 e^2/h) moves. If, for example, every time you add 100 mV to c_2 it moves you back 21 mV in c_1 and adding 100 mV to c_3 moves you back 7 mV in c_1 and so on, you can construct an equation (similar to the procedure in the previous section) like $p_1 = c_1 + 0.21c_2 + 0.07c_3 + \ldots$ (I've suppressed offsets in c_i, and will add them back later). This procedure can be repeated for all of the barrier parameters, for the plunger you could attempt to do wall control on dot size (say, by taking the slope of Coulomb blockade peaks or conductance fluctuations in 2D plots) but in my case I was interested only in statistics as a function of dot size, not following individual features, so if gate 4 was the plunger I simply set $p_4 = c_4$.

After all of this you have a matrix equation $\mathbf{p} = \mathbf{M}(\mathbf{c} - \mathbf{c}^0)$ where $\mathbf{c}^0$ is the set

---

[5] Notice that this kind of wall control can't be linearized about a point with balanced leads, because we need to open another QPC up to one or two full modes in order to independently measure the first QPC, but for all but the smallest devices the nonlinearities should be small enough that this doesn't matter.

of gate voltages you linearized about. Now you can invert this equation,[6] yielding $\mathbf{c} = \mathbf{c}^0 + \mathbf{M}^{-1}\mathbf{p}$. Now if you make a wave to store the values of the parameters p_i you can use them as sweep parameters, plugging them into this matrix equation every time you change one and using the output to set the gate voltages. These parameters have roughly the same scaling as the original gate voltages (so a 1-mV change in p_1 will correspond to approximately a 1-mV change in c_1 with associated corrections to the other gates) but they are centered about zero unless you specifically set them otherwise.

---

[6] Igor version 5 now has a `MatrixInverse` command to get this directly, in prior versions you had to get it as a byproduct of `MatrixGaussJ`, whatever that means.

Bibliography

[1] Cronenwett, S. M. *Coherence, charging, and spin effects in quantum dots and point contacts*. PhD thesis, Stanford University, (2001).

[2] Mabuchi, H. and Doherty, A. C. Cavity quantum electrodynamics: Coherence in context. *Science* **298**, 1372–7 (2002).

[3] Keller, M., Lange, B., Hayasaka, K., Lange, W., and Walther, H. Continuous generation of single photons with controlled waveform in an ion-trap cavity system. *Nature* **431**, 1075–8 (2004).

[4] Vahala, K. J. Optical microcavities. *Nature* **424**, 839–46 (2003).

[5] Badolato, A., Hennessy, K., Atature, M., Dreiser, J., Hu, E., Petroff, P. M., and Imamoglu, A. Deterministic coupling of single quantum dots to single nanocavity modes. *Science* **308**, 1158–61 (2005).

[6] Jarillo-Herrero, P., Sapmaz, S., Dekker, C., Kouwenhoven, L. P., and van der Zant, H. S. J. Electron-hole symmetry in a semiconducting carbon nanotube quantum dot. *Nature* **429**, 389–92 (2004).

[7] Mason, N., Biercuk, M. J., and Marcus, C. M. Local gate control of a carbon nanotube double quantum dot. *Science* **303**, 655–8 (2004).

[8] Borgstrom, M. T., Zwiller, V., Muller, E., and Imamoglu, A. Optically bright quantum dots in single nanowires. *Nano Lett.* **5**, 1439–43 (2005).

[9] Davidovic, D. and Tinkham, M. Spectroscopy, interactions, and level splittings in Au nanoparticles. *Phys. Rev. Lett.* **83**, 1644–7 (1999).

[10] Petta, J. R. and Ralph, D. C. Measurements of strongly anisotropic g factors for spins in single quantum states. *Phys. Rev. Lett.* **89**, 156802 (2002).

[11] Kroutvar, M., Ducommun, Y., Heiss, D., Bichler, M., Schuh, D., Abstreiter, G., and Finley, J. J. Optically programmable electron spin memory using semiconductor quantum dots. *Nature* **432**, 81–84 (2004).

[12] Bracker, A. S., Stinaff, E. A., Gammon, D., Ware, M. E., Tischler, J. G., Shabaev, A., Efros, A. L., Park, D., Gershoni, D., Korenev, V. L., and Merkulov, I. A. Optical pumping of the electronic and nuclear spin of single charge-tunable quantum dots. *Phys. Rev. Lett.* **94**, 047402 (2005).

[13] Chiorescu, I., Bertet, P., Semba, K., Nakamura, Y., Harmans, C. J. P. M., and Mooij, J. E. Coherent dynamics of a flux qubit coupled to a harmonic oscillator. *Nature* **431**, 159–62 (2004).

[14] Wallraff, A., Schuster, D. I., Blais, A., Frunzio, L., Huang, R. S., Majer, J., Kumar, S., Girvin, S. M., and Schoelkopf, R. J. Strong coupling of a single photon to a superconducting qubit using circuit quantum electrodynamics. *Nature* **431**, 162–7 (2004).

[15] Stormer, H. L., Chang, A., Tsui, D. C., Hwang, J. C. M., Gossard, A. C., and Weigmann, W. Fractional quantization of the Hall-effect. *Phys. Rev. Lett.* **50**, 1953–6 (1983).

[16] Stormer, H. L., Tsui, D. C., and Gossard, A. C. The fractional quantum Hall effect. *Rev. Mod. Phys.* **71**, S298–305 (1999).

[17] Eisenstein, J. P. and MacDonald, A. H. Bose-einstein condensation of excitons in bilayer electron systems. *Nature* **432**, 691–4 (2004).

[18] Thornton, T. J., Pepper, M., Ahmed, H., Andrews, D., and Davies, G. J. One-dimensional conduction in the 2D electron-gas of a GaAs/AlGaAs heterojunction. *Phys. Rev. Lett.* **56**, 1198–1201 (1986).

[19] van Wees, B. J., van Houten, H., Beenakker, C. W. J., Williamson, J. G., Kouwenhoven, L. P., van der Marel, D., and Foxon, C. T. Quantized conductance of point contacts in a two-dimensional electron gas. *Phys. Rev. Lett.* **60**, 848–91 (1988).

[20] Cronenwett, S. M., Lynch, H. J., Goldhaber-Gordon, D., Kouwenhoven, L. P., Marcus, C. M., Hirose, K., Wingreen, N. S., and Umansky, V. Low-temperature fate of the 0.7 structure in a point contact: A Kondo-like correlated state in an open system. *Phys. Rev. Lett.* **88**, 226805 (2002).

[21] Auslaender, O. M., Steinberg, H., Yacoby, A., Tserkovnyak, Y., Halperin, B. I., Baldwin, K. W., Pfeiffer, L. N., and West, K. W. Spin-charge separation and localization in one dimension. *Science* **308**, 88–92 (2005).

[22] van Wees, B. J., Kouwenhoven, L. P., Harmans, C. J. P. M., Williamson, J. G., Timmering, C. E., Brockaart, M. E. I., Foxon, C. T., and Harris, J. J. Observation of zero-diomensional states in a one-dimensional electron interferometer. *Phys. Rev. Lett.* **62**, 2523–6 (1989).

[23] Meirav, U., Kastner, M. A., and Wind, S. J. Single-electron charging and periodic conductance resonances in GaAs nanostructures. *Phys. Rev. Lett.* **65**, 771–4 (1990).

[24] Kastner, M. A. The single-electron transistor. *Rev. Mod. Phys.* **64**, 849–58 (1992).

[25] Kouwenhoven, L. P., Austing, D. G., and Tarucha, S. Few-electron quantum dots. *Rep. Prog. Phys.* **64**, 701–36 (2001).

[26] Drummond, T. J., Masselink, W. T., and Morkoc, H. Modulation-doped GaAs/-(Al,Ga)As heterojunction field-effect transistors—MODFETs. *Proc. IEEE* **74**, 773–822 (1986).

[27] Kristensen, A., Bruus, H., Hansen, A. E., Jensen, J. B., Lindelof, P. E., Marckmann, C. J., Nygård, J., and Sørensen, C. B. Bias and temperature dependence of the 0.7 conductance anomaly in quantum point contacts. *Phys. Rev. B* **62**, 10950–7 (2000).

[28] Fuhrer, A., Lüscher, S., Ihn, T., Heinzel, T., Ensslin, K., Wegscheider, W., and Bichler, M. Energy spectra of quantum rings. *Nature* **413**, 822–5 (2001).

[29] Fuhrer, A., Dorn, A., Lüscher, S., Heinzel, T., Ensslin, K., Wegscheider, W., and Bichler, M. Electronic properties of nanostructures defined in Ga[Al]As heterostructures by local oxidation. *Superlattices and Microstructures* **31**, 19–42 (2002).

[30] Crook, R., Graham, A. C., Smith, C. G., Farrer, I., Beere, H. E., and Ritchie, D. A. Erasable electrostatic lithography for quantum components. *Nature* **424**, 591–4 (2003).

[31] Zheng, H. Z., Wei, H. P., Tsui, D. C., and Weimann, G. Gate-controlled transport in narrow GaAs/Al$_x$Ga$_{1-x}$As heterostructures. *Phys. Rev. B* **34**, 5635–8 (1986).

[32] Stopa, M. Quantum dot self-consistent electronic structure and the Coulomb blockade. *Phys. Rev. B* **54**, 13767–83 (1996).

[33] Stopa, M., van der Wiel, W. G., Franceschi, S. D., Tarucha, S., and Kouwenhoven, L. P. Magnetically induced chessboard pattern in the conductance of a kondo quantum dot. *Phys. Rev. Lett.* **91**, 046601 (2003).

[34] Hatano, T., Stopa, M., and Tarucha, S. Single-electron delocalization in hybrid vertical-lateral double quantum dots. *Science* **309**, 268–71 (2005).

[35] Topinka, M. A., LeRoy, B. J., Westervelt, R. M., Shaw, S. E. J., Fleischmann, R., Heller, E. J., Maranowski, K. D., and Gossard, A. C. Coherent branched flow in a two-dimensional electron gas. *Nature* **410**, 183–6 (2001).

[36] Vanicek, J. and Heller, E. J. Uniform semiclassical wave function for coherent two-dimensional electron flow. *Phys. Rev. E* **67**, 016211 (2003).

[37] Datta, S. *Electronic Transport in Semiconductor Systems.* Cambridge University Press, (1997).

[38] Imry, Y. *Introduction to Mesoscopic Physics.* Oxford University Press, (1997).

[39] Kouwenhoven, L. P., Marcus, C. M., McEuen, P. L., Tarucha, S., Westervelt, R. M., and Wingreen, N. S. Electron transport in quantum dots. In *Mesoscopic Electron Transport.* Kluwer (1997).

[40] van der Wiel, W. G., Franceschi, S. D., Elzerman, J. M., Fujisawa, T., Tarucha, S., and Kouwenhoven, L. P. Electron transport through double quantum dots. *Rev. Mod. Phys.* **75**, 1–22 (2003).

[41] Kane, B. E., Facer, G. R., Dzurak, A. S., Lumpkin, N. E., Clark, R. G., Pfeiffer, L. N., and West, K. W. Quantized conductance in quantum wires with gate-controlled width and electron density. *Appl. Phys. Lett.* **72**, 3506–8 (1998).

[42] de Picciotto, R., Pfeiffer, L. N., Baldwin, K. W., and West, K. W. Nonlinear response of a clean one-dimensional wire. *Phys. Rev. Lett.* **92**, 036805 (2004).

[43] Cronenwett, S. M., Maurer, S. M., Patel, S. R., Marcus, C. M., Duruoz, C. I., and Harris, J. S. Mesoscopic Coulomb blockade in an open-channel quantum dot. *Phys. Rev. Lett.* **81**, 5904–7 (1998).

[44] Marcus, C. M., Westervelt, R. M., Hopkins, P. F., and Gossard, A. C. Phase breaking in ballistic quantum dots—experiment and analysis based on chaotic scattering. *Phys. Rev. B* **48**, 2460–4 (1993).

[45] Bird, J. P., Ishibashi, K., Ferry, D. K., Ochiai, Y., Aoyagi, Y., and Sugano, T. Phase breaking in ballistic quantum dots—transition from 2-dimensional to zero-dimensional behavior. *Phys. Rev. B* **51**, 18037–40 (1995).

[46] Liang, C. T., Castleton, I. M., Frost, J. E. F., Barnes, C. H. W., Smith, C. G., Ford, C. J. B., Ritchie, D. A., and Pepper, M. Resonant transmission through an open quantum dot. *Phys. Rev. B* **55**, 6723–6 (1997).

[47] Zumbühl, D. M., Miller, J. B., Marcus, C. M., Campman, K., and Gossard, A. C. Spin-orbit coupling, antilocalization, and parallel magnetic fields in quantum dots. *Phys. Rev. Lett.* **89**, 276803 (2002).

[48] Folk, J. A., Potok, R. M., Marcus, C. M., and Umansky, V. A gate-controlled bidirectional spin filter using quantum coherence. *Science* **299**, 679–82 (2003).

[49] Tarucha, S., Austing, D. G., Honda, T., van der Hage, R. J., and Kouwenhoven, L. P. Shell filling and spin effects in a few electron quantum dot. *Phys. Rev. Lett.* **77**, 3613–6 (1996).

[50] Stewart, D. R. *Level spectroscopy of a quantum dot.* PhD thesis, Stanford University, (1999).

[51] Franceschi, S. D., Hanson, R., van der Wiel, W. G., Elzerman, J. M., Wijpkema, J. J., Fujisawa, T., Tarucha, S., and Kouwenhoven, L. P. Out-of-equilibrium Kondo effect in a mesoscopic device. *Phys. Rev. Lett.* **89**, 156801 (2002).

[52] Patel, S. R., Cronenwett, S. C., Stewart, D. R., Huibers, A. G., Marcus, C. M., Duruoz, C. I., Harris, J. S., Campman, K., and Gossard, A. C. Statistics of Coulomb blockade peak spacings. *Phys. Rev. Lett.* **80**, 4522–5 (1998).

[53] Sachrajda, A. S., Hawrylak, P., Ciorga, M., Gould, C., and Zawadzki, P. Spin polarized injection into a quantum dot by means of the spatial separation of spins. *Physica E* **10**, 493–8 (2001).

[54] Pioro-Ladriere, M., Ciorga, M., Lapointe, J., Zawadzki, P., Korkusinski, M., Hawrylak, P., and Sachrajda, A. S. Spin-blockade spectroscopy of a two-level artificial molecule. *Phys. Rev. Lett.* **91**, 026803 (2003).

[55] Elzerman, J. M., Hanson, R., van Beveren, L. H. W., Witkamp, B., Vandersypen, L. M. K., and Kouwenhoven, L. P. Single-shot read-out of an individual electron spin in a quantum dot. *Nature* **430**, 431–5 (2004).

[56] Biercuk, M. J. *Local gate control in carbon nanotube quantum devices.* PhD thesis, Harvard University, (2005).

[57] Chan, I. H., Fallahi, P., Westervelt, R. M., Maranowski, K. D., and Gossard, A. C. Capacitively coupled quantum dots as a single-electron switch. *Physica E* **17**, 584–8 (2003).

[58] Lu, W., Ji, Z. Q., Pfeiffer, L., West, K. W., and Rimberg, A. J. Real-time detection of electron tunnelling in a quantum dot. *Nature* **423**, 422–5 (2003).

[59] Johnson, A. C., Marcus, C. M., Hanson, M. P., and Gossard, A. C. Coulomb-modified Fano resonance in a one-lead quantum dot. *Phys. Rev. Lett.* **93**, 106803 (2004).

[60] Fano, U. Effects of configuration interaction on intensities and phase shifts. *Phys. Rev.* **124**, 1866–78 (1961).

[61] Madhavan, V., Chen, W., Jamneala, T., Crommie, M. F., and Wingreen, N. S. Tunneling into a single magnetic atom: Spectroscopic evidence of the Kondo resonance. *Science* **280**, 567–9 (1998).

[62] Gores, J., Goldhaber-Gordon, D., Heemeyer, S., Kastner, M. A., Shtrikman, H., Mahalu, D., and Meirav, U. Fano resonances in electronic transport through a single-electron transistor. *Phys. Rev. B* **62**, 2188–94 (2000).

[63] Zacharia, I. G., Goldhaber-Gordon, D., Granger, G., Kastner, M. A., Khavin, Y. B., Shtrikman, H., Mahalu, D., and Meirav, U. Temperature dependence of Fano line shapes in a weakly coupled single-electron transistor. *Phys. Rev. B* **64**, 155311 (2001).

[64] Fuhner, C., Keyser, U. F., Haug, R. J., Reuter, D., and Wieck, A. D. Phase measurements using two-channel Fano interference in a semiconductor quantum dot. Preprint at `http://arxiv.org/cond-mat/0307590` (2003).

[65] Kobayashi, K., Aikawa, H., Katsumoto, S., and Iye, Y. Tuning of the Fano effect through a quantum dot in an Ahaonov-Bohm interferometer. *Phys. Rev. Lett.* **88**, 256806 (2002).

[66] Kobayashi, K., Aikawa, H., Sano, A., Katsumoto, S., and Iye, Y. Fano resonance in a quantum wire with a side-coupled quantum dot. *Phys. Rev. B* **70**, 035319 (2004).

[67] Kim, J., Kim, J.-R., Lee, J.-O., Park, J. W., So, H. M., Kim, N., Kang, K., Yoo, K.-H., and Kim, J.-J. Fano resonance in crossed carbon nanotubes. *Phys. Rev. Lett.* **90**, 166403 (2003).

[68] Clerk, A. A., Waintal, X., and Brouwer, P. W. Fano resonances as a probe of phase coherence in quantum dots. *Phys. Rev. Lett.* **86**, 4636–9 (2001).

[69] Xiong, Y.-J. and Xiong, S.-J. Asymmetric line shape and Fano interference in the transport of electrons through a multilevel quantum dot in the Coulomb blockade regime. *Phys. Rev. B* **66**, 153315 (2002).

[70] Song, J. F., Ochiai, Y., and Bird, J. P. Fano resonances in open quantum dots and their application as spin filters. *Appl. Phys. Lett.* **82**, 4561–3 (2003).

[71] Field, M., Smith, C. G., Pepper, M., Ritchie, D. A., Frost, J. E. F., Jones, G. A. C., and Hasko, D. G. Measurement of Coulomb blockade with a noninvasive voltage probe. *Phys. Rev. Lett.* **70**, 1311–4 (1993).

[72] Amlani, I., Orlov, A. O., Snider, G. L., Lent, C. S., and Bernstein, G. H. External charge state detection of a double-dot system. *Appl. Phys. Lett.* **71**, 1730–2 (1997).

[73] Duncan, D. S., Livermore, C., Westervelt, R. M., Maranowski, K. D., and Gossard, A. C. Direct measurement of the destruction of charge quantization in a single-electron box. *Appl. Phys. Lett.* **74**, 1045–7 (1999).

[74] Chan, I. H., Westervelt, R. M., Maranowski, K. D., and Gossard, A. C. Strongly capacitively coupled quantum dots. *Appl. Phys. Lett.* **80**, 1818–20 (2002).

[75] Breit, G. and Wigner, E. Capture of slow neutrons. *Phys. Rev.* **49**, 519 (1936).

[76] Aharony, A., Entin-Wohlman, O., Halperin, B. I., and Imry, Y. Phase measurement in the mesoscopic Aharonov-Bohm interferometer. *Phys. Rev. B* **66**, 115311 (2002).

[77] Ng, T. K. and Lee, P. A. On-site Coulomb repulsion and resonant tunneling. *Phys. Rev. Lett.* **61**, 1768–71 (1988).

[78] Taniguchi, T. and Buttiker, M. Friedel phases and phases of transmission amplitudes in quantum scattering systems. *Phys. Rev. B* **60**, 13814–23 (1999).

[79] Yacoby, A., Heiblum, M., Mahalu, D., and Shtrikman, H. Coherence and phase sensitive measurements in a quantum dot. *Phys. Rev. Lett.* **74**, 4047–50 (1995).

[80] Schuster, R., Buks, E., Heiblum, M., Mahalu, D., Umansky, V., and Shtrikman, H. Phase measurement in a quantum dot via a double-slit interference experiment. *Nature* **385**, 417–20 (1997).

[81] Baltin, R. and Gefen, Y. An approximate sign sum rule for the transmission amplitude through a quantum dot. *Phys. Rev. Lett.* **83**, 5094–7 (1999).

[82] Yeyati, A. L. and Buttiker, M. Scattering phases in quantum dots: an analysis based on lattice models. *Phys. Rev. B* **62**, 7307–15 (2000).

[83] Clerk, A. A. private communication, (2003).

[84] Dicarlo, L., Lynch, H. J., Johnson, A. C., Childress, L. I., Crockett, K., Marcus, C. M., Hanson, M. P., and Gossard, A. C. Differential charge sensing and charge delocalization in a tunable double quantum dot. *Phys. Rev. Lett.* **92**, 226801 (2004).

[85] Gardelis, S., Smith, C. G., Cooper, J., Ritchie, D. A., Linfield, E. H., Jin, Y., and Pepper, M. Dephasing in an isolated double-quantum-dot system deduced from single-electron polarization measurements. *Phys. Rev. B* **67**, 073302 (2003).

[86] Engel, H.-A., Golovach, V. N., Loss, D., Vandersypen, L. M. K., Elzerman, J. M., Hanson, R., and Kouwenhoven, L. P. Measurement efficiency and n-shot readout of spin qubits. *Phys. Rev. Lett.* **93**, 106804 (2004).

[87] Buks, E., Schuster, R., Heiblum, M., Mahalu, D., and Umansky, V. Dephasing in an electron interference by a 'which-path' detector. *Nature* **391**, 871–4 (1998).

[88] Aleiner, I. L., Wingreen, N. S., and Meir, Y. Dephasing and the orthogonality catastrophy in tunneling through a quantum dot: the 'Which Path?' interferometer. *Phys. Rev. Lett.* **79**, 3740–3 (1997).

[89] Buehler, T. M., Reilly, D. J., Brenner, R., Hamilton, A. R., Dzurak, A. S., and Clark, R. G. Correlated charge detection for readout of a solid-state quantum computer. *Appl. Phys. Lett.* **82**, 577–9 (2003).

[90] Schoelkopf, R. J., Wahlgren, P., Kozhevnikov, A. A., Delsing, P., and Prober, D. E. The radio-frequency single-electron transistor (RF-SET): a fast and ultrasensitive electrometer. *Science* **280**, 1238–42 (1998).

[91] Elzerman, J. M., Hanson, R., Greidanus, J. S., van Beveren, L. H. W., Franceschi, S. D., Vandersypen, L. M. K., Tarucha, S., and Kouwenhoven, L. P. Few-electron quantum dot circuit with integrated charge read out. *Phys. Rev. B* **67**, R161308 (2003).

[92] Kouwenhoven, L. P., Oosterkamp, T. H., Danoesastro, M. W. S., Eto, M., Austing, D. G., Honda, T., and Tarucha, S. Excitation spectra of circular, few-electron quantum dots. *Science* **278**, 1788–92 (1997).

[93] Pothier, H., Lafarge, P., Urbina, C., Esteve, D., and Devoret, M. H. Single-electron pump based on charging effects. *Europhys. Lett.* **17**, 249–54 (1992).

[94] Blick, R. H., Haug, R. J., Weis, J., Pfannkuche, D., von Klitzing, K., and Eberl, K. Single-electron tunneling through a double quantum dot: the artificial molecule. *Phys. Rev. B* **53**, 7899–902 (1996).

[95] Livermore, C., Crouch, C. H., Westervelt, R. M., Campman, K. L., and Gossard, A. C. The Coulomb blockade in coupled quantum dots. *Science* **274**, 1332–5 (1996).

[96] Cohen-Tannoudji, C. *Quantum Mechanics*, volume 1, chapter 4. Wiley (1977).

[97] Ziegler, R., Bruder, C., and Schoeller, H. Transport through double quantum dots. *Phys. Rev. B* **62**, 1961–70 (2000).

[98] Johnson, A. C., Marcus, C. M., Hanson, M. P., and Gossard, A. C. Charge sensing of excited states in an isolated double quantum dot. *Phys. Rev. B* **71**, 115333 (2005).

[99] Folk, J. A., Marcus, C. M., and Harris, J. S. Decoherence in nearly isolated quantum dots. *Phys. Rev. Lett.* **87**, 206802 (2001).

[100] Aleiner, I. L., Brouwer, P. W., and Glazman, L. I. Quantum effects in Coulomb blockade. *Phys. Rep.* **358**, 309–440 (2002).

[101] Loss, D. and DiVincenzo, D. P. Quantum computation with quantum dots. *Phys. Rev. A* **57**, 120–6 (1998).

[102] Awschalom, D. D., Loss, D., and Samarth, N. *Semiconductor Spintronics and Quantum Computation.* Springer, (2002).

[103] Gurvitz, S. A. Measurements with a noninvasive detector and dephasing mechanism. *Phys. Rev. B* **56**, 15213–23 (1997).

[104] Korotkov, A. N. and Averin, D. V. Continuous weak measurement of quantum coherent oscillations. *Phys. Rev. B* **64**, 165310 (2001).

[105] Pilgram, S. and Buttiker, M. Efficiency of mesoscopic detectors. *Phys. Rev. Lett.* **89**, 200401 (2002).

[106] Hartmann, U. and Wilhelm, F. K. Decoherence of charge states in a double quantum dot due to cotunneling. *Phys. Status Solidi B* **233**, 385–90 (2002).

[107] Johnson, A. T., Kouwenhoven, L. P., de Jong, W., van der Vaart, N. C., Harmans, C. J. P. M., and Foxon, C. T. Zero-dimensional states and single-electron charging in quantum dots. *Phys. Rev. Lett.* **69**, 1592–5 (1992).

[108] Stewart, D. R., Sprinzak, D., Marcus, C. M., Duruoz, C. I., and Harris, J. S. Correlations between ground and excited state spectra of a quantum dot. *Science* **278**, 1784–8 (1997).

[109] van der Vaart, N. C., de Ruyter van Steveninck, M. P., Kouwenhoven, L. P., Johnson, A. T., Nazarov, Y. V., Harmans, C. J. P. M., and Foxons, C. T. Time-resolved tunneling of single electrons between Landau levels in a quantum dot. *Phys. Rev. Lett.* **73**, 320–3 (1995).

[110] Sivan, U., Milliken, F. P., Milrove, K., Rishton, S., Lee, Y., Hong, J. M., Boegli, V., Kern, D., and Defranza, M. Spectroscopy, electron-electron interaction, and level statistics in a disordered quantum dot. *Europhys. Lett.* **25**, 605–11 (1994).

[111] Fujisawa, T., Austing, D. G., Tokura, Y., Hirayama, Y., and Tarucha, S. Electrical pulse measurement, inelastic relaxation, and non-equilibrium transport in a quantum dot. *J. Phys. Cond. Mat.* **15**, R1395–428 (2003).

[112] Elzerman, J. M., Hanson, R., van Beveren, L. H. W., Vandersypen, L. M. K., and Kouwenhoven, L. P. Excited-state spectroscopy on a nearly closed quantum dot via charge detection. *Appl. Phys. Lett.* **84**, 4617–9 (2004).

[113] Johnson, A. C., Petta, J. R., Marcus, C. M., Hanson, M. P., and Gossard, A. C. Singlet-triplet spin blockade and charge sensing in a few-electron double quantum dot. Preprint at `http://arxiv.org/cond-mat/0410679` (2004).

[114] Chan, I. H., Fallahi, P., Vidan, A., Westervelt, R. M., Hanson, M. P., and Gossard, A. C. Few-electron double quantum dots. *Nanotechnology* **15**, 609–13 (2004).

[115] Ciorga, M., Sachrajda, A. S., Hawrylak, P., Gould, C., Zawadzki, P., Jullian, S., Feng, Y., and Wasilewski, Z. Addition spectrum of a lateral dot from Coulomb and spin-blockade spectroscopy. *Phys. Rev. B* **61**, R16315–8 (2000).

[116] Kogan, A., Granger, G., Kastner, M. A., Goldhaber-Gordon, D., and Shtrikman, H. Singlet-triplet transition in a single-electron transistor at zero magnetic field. *Phys. Rev. B* **67**, 113309 (2003).

[117] Ono, K., Austing, D. G., Tokura, Y., and Tarucha, S. Current rectification by Pauli exclusion in a weakly coupled double quantum dot system. *Science* **297**, 1313–7 (2002).

[118] Ashcroft, N. W. and Mermin, N. D. *Solid State Physics*, chapter 32. Harcourt (1976).

[119] Weinmann, D., Hausler, W., and Kramer, B. Spin blockades in linear and nonlinear transport through quantum dots. *Phys. Rev. Lett.* **74**, 984–7 (1995).

[120] Imamura, H., Aoki, H., and Maksym, P. A. Spin blockade in single and double quantum dots in magnetic fields: a correlation effect. *Phys. Rev. B* **57**, R4257–60 (1998).

[121] Tokura, Y., Austing, D. G., and Tarucha, S. Single-electron tunneling in two vertically coupled quantum dots. *J. Phys. Cond. Mat.* **11**, 6023–34 (1999).

[122] Ciorga, M., Pioro-Ladriere, M., Zawadzki, P., Hawrylak, P., and Sachrajda, A. S. Tunable negative differential resistance controlled by spin blockade in single-electron transistors. *Appl. Phys. Lett.* **80**, 2177–9 (2002).

[123] Rokhinson, L. P., Guo, L. J., Chou, S. Y., and Tsui, D. C. Spintronics with Si quantum dots. *Microelectronic Engineering* **63**, 147–53 (2002).

[124] Huttel, A. K., Qin, H., Holleitner, A. W., Blick, R. H., Neumaier, K., Weinmann, D., Eberl, K., and Kotthaus, J. P. Spin blockade in ground state resonance of a quantum dot. *Europhys. Lett.* **62**, 712–8 (2003).

[125] Rogge, M. C., Fuhner, C., Keyser, U. F., and Haug, R. J. Spin blockade in capacitively coupled quantum dots. *Appl. Phys. Lett.* **85**, 606–8 (2004).

[126] Petta, J. R., Johnson, A. C., Marcus, C. M., Hanson, M. P., and Gossard, A. C. Manipulation of a single charge in a double quantum dot. *Phys. Rev. Lett.* **93**, 186802 (2004).

[127] Fujisawa, T., Oosterkamp, T. H., van der Wiel, W. G., Broer, B. W., Aguado, R., Tarucha, S., and Kouwenhoven, L. P. Spontaneous emission spectrum in double quantum dot devices. *Science* **282**, 932–5 (1998).

[128] Koppens, F. H. L., Folk, J. A., Elzerman, J. M., Hanson, R., van Beveren, L. H. W., Fink, I. T., Tranitz, H. P., Wegscheider, W., Kouwenhoven, L. P., and Vandersypen, L. M. K. Control and detection of singlet-triplet mixing in a random nuclear field. *Science* **309**, 1346–50 (2005).

[129] Su, B., Goldman, V. J., and Cunningham, J. E. Single-electron tunneling in nanometer-scale double-barrier heterostructure devices. *Phys. Rev. B* **46**, 7644–55 (1992).

[130] Ashoori, R. C., Stormer, H. L., Weiner, J. S., Pfeiffer, L. N., Baldwin, K. W., and West, K. W. N-electron ground state energies of a quantum dot in a magnetic field. *Phys. Rev. Lett.* **71**, 613–6 (1993).

[131] Fujisawa, T., Austing, D. G., Tokura, Y., Hirayama, Y., and Tarucha, S. Allowed and forbidden transitions in artificial hydrogen and helium atoms. *Nature* **419**, 278–81 (2002).

[132] Zumbühl, D. M., Marcus, C. M., Hanson, M. P., and Gossard, A. C. Cotunneling spectroscopy in few-electron quantum dots. *Phys. Rev. Lett.* **93**, 256801 (2004).

[133] Kyriadikis, J., Pioro-Ladriere, M., Ciorga, M., Sachrajda, A. S., and Hawrylak, P. Voltage-tunable singlet-triplet transition in lateral quantum dots. *Phys. Rev. B* **66**, 035320 (2002).

[134] Wagner, M., Merkt, U., and Chaplik, A. V. Spin-singlet spin-triplet oscillations in quantum dots. *Phys. Rev. B* **45**, 1951–4 (1992).

[135] Pfannkuche, D., Gudmundsson, V., and Maksym, P. A. Comparison of a Hartree, a Hartree-Fock, and an exact treatment of quantum-dot helium. *Phys. Rev. B* **47**, 2244–50 (1993).

[136] Hawrylak, P. Single-electron capacitance spectroscopy of few-electron artificial atoms in a magnetic field—theory and experiment. *Phys. Rev. Lett.* **71**, 3347–50 (1993).

[137] van Beveren, L. H. W., Hanson, R., Vink, I. T., Koppens, F. H. L., Kouwenhoven, L. P., and Vandersypen, L. M. K. Spin filling of a quantum dot derived from excited-state spectroscopy. Preprint at `http://arxiv.org/cond-mat/0505486` (2005).

[138] Khaetskii, A. V. and Nazarov, Y. V. Spin relaxation in semiconductor quantum dots. *Phys. Rev. B* **61**, 12639–42 (2000).

[139] Erlingsson, S. I., Nazarov, Y. V., and Fal'ko, V. I. Nucleus-mediated spin-flip transitions in GaAs quantum dots. *Phys. Rev. B* **64**, 195306 (2001).

[140] Khaetskii, A. V., Loss, D., and Glazman, L. Electron spin decoherence in quantum dots due to interaction with nuclei. *Phys. Rev. Lett.* **88**, 186802 (2002).

[141] Merkulov, I. A., Efros, A. L., and Rosen, M. Electron spin relaxation by nuclei in semiconductor quantum dots. *Phys. Rev. B* **65**, 205309 (2002).

[142] de Sousa, R. and Sarma, S. D. Theory of nuclear-induced spectral diffusion: spin decoherence of phosphorus donors in Si and GaAs quantum dots. *Phys. Rev. B* **68**, 115322 (2003).

[143] Coish, W. A. and Loss, D. Hyperfine interaction in a quantum dot: non-Markovian electron spin dynamics. *Phys. Rev. B* **70**, 195340 (2004).

[144] Golovach, V. N., Khaetskii, A. V., and Loss, D. Phonon-induced decay of the electron spin in quantum dots. *Phys. Rev. Lett.* **93**, 016601 (2004).

[145] Johnson, A. C., Petta, J. R., Taylor, J. M., Yacoby, A., Lukin, M. D., Marcus, C. M., Hanson, M. P., and Gossard, A. C. Triplet-singlet spin relaxation via nuclei in a double quantum dot. *Nature* **435**, 925–8 (2005).

[146] Petta, J. R., Johnson, A. C., Yacoby, A., Marcus, C. M., Hanson, M. P., and Gossard, A. C. Pulsed-gate measurements of the singlet-triplet relaxation time in a two-electron double quantum dot. Preprint at `http://arxiv.org/cond-mat/0412048` (2004).

[147] Wald, K. R., Kouwenhoven, L. P., McEuen, P. L., van der Vaart, N. C., and Foxon, C. T. Local dynamic nuclear polarization using quantum point contacts. *Phys. Rev. Lett.* **73**, 1011–4 (1994).

[148] Salis, G. Optical manipulation of nuclear spin by a two-dimensional electron gas. *Phys. Rev. Lett.* **86**, 2677–80 (2001).

[149] Kumada, N., Muraki, K., Hashimoto, K., and Hirayama, Y. Spin degree of freedom in the ν=1 bilayer electron system investigated via nuclear spin relaxation. *Phys. Rev. Lett.* **94**, 096802 (2005).

[150] Smet, J. H., Deutchmann, R. A., Ertl, F., Wegscheider, W., Abstreiter, G., and von Klitzing, K. Gate-voltage control of spin interactions between electrons and nuclei in a semiconductor. *Nature* **415**, 281–6 (2002).

[151] Ono, K. and Tarucha, S. Nuclear-spin-induced oscillatory current in spin-blockaded quantum dots. *Phys. Rev. Lett.* **92**, 256803 (2004).

[152] Paget, D., Lampel, G., Sapoval, G., and Safarov, V. I. Low field electron-nuclear spin coupling in gallium-arsenide under optical-pumping conditions. *Phys. Rev. B* **15**, 5780–96 (1977).

[153] Dobers, M., von Klitzing, K., Schneider, J., Weimann, G., and Ploog, K. Electrical detection of nuclear magnetic-resonance in GaAs-Al$_x$Ga$_{1-x}$As heterostructures. *Phys. Rev. Lett.* **61**, 1650–3 (1988).

[154] Sarma, S. D., de Sousa, R., Hu, X., and Koiller, B. Spin quantum computation in silicon nanostructures. *Solid State Commun* **133**, 737–46 (2005).

[155] Wolf, S. A., Awschalom, D. D., Buhrman, R. A., Daughton, J. M., von Molnar, S., Roukes, M. L., Chtchelkanova, A. Y., and Treger, D. M. Spintronics: a spin-based electronics vision for the future. *Science* **294**, 1488–95 (2001).

[156] Kikkawa, J. M. and Awschalom, D. D. Resonant spin amplification in n-type GaAs. *Phys. Rev. Lett.* **80**, 4313–6 (1998).

[157] Burkard, G., Loss, D., and DiVincenzo, S. P. Coupled quantum dots as quantum gates. *Phys. Rev. B* **59**, 2070–8 (1999).

[158] Ando, T., Fowler, A. B., and Stern, F. Electronic properties of two-dimensional systems. *Rev. Mod. Phys.* **54**, 437–672 (1982).

[159] Schulten, K. and Wolynes, P. G. Semi-classical description of electron-spin motion in radicals including effect of electron hopping. *J. Chem. Phys.* **68**, 3292–7 (1978).

[160] Folk, J. A. *Spin Transport Measurements in GaAs Quantum Dots.* PhD thesis, Stanford University, (2003).

[161] Huibers, A. G. *Electron Transport and Dephasing in Semiconductor Quantum Dots.* PhD thesis, Stanford University, (1999).